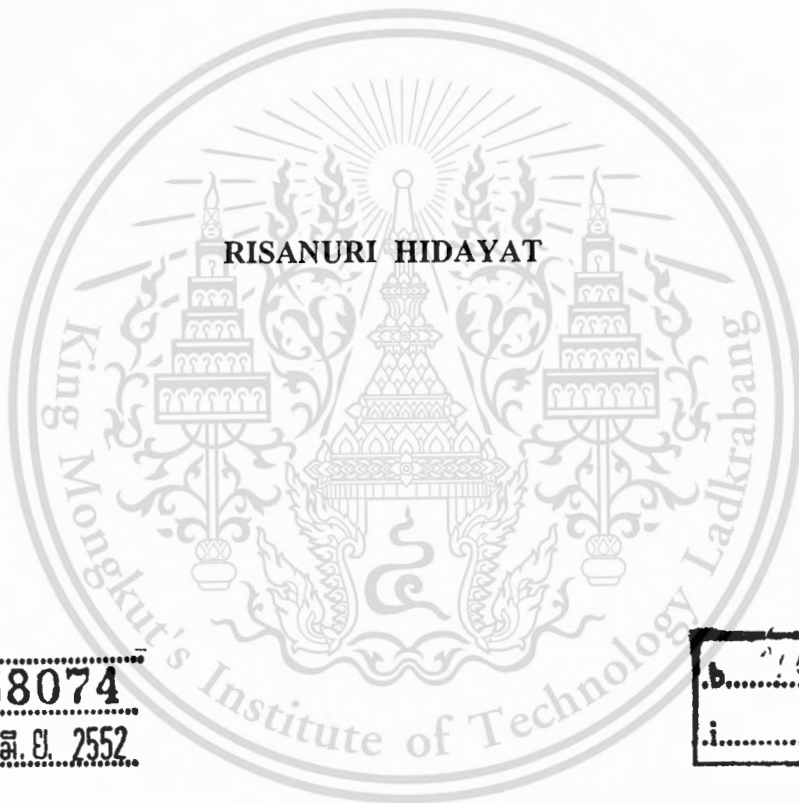
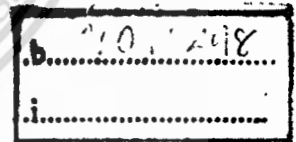


สำนักหอสมุดกลาง พระจอมเกล้าลาดกระบัง

ULTRA WIDEBAND CIRCUIT DESIGN
AND ITS PERFORMANCE ANALYSIS OF INTERFERENCE



เลขหมู่.....
เลขทะเบียน..... 58074
วัน,เดือน,ปี 17 ส.ย. 2552.



A THESIS SUBMITTED IN PARTIAL FULFILLMENT
OF THE REQUIREMENTS FOR DEGREE OF
DOCTOR OF ENGINEERING IN ELECTRICAL ENGINEERING
FACULTY OF ENGINEERING
KING MONGKUT'S INSTITUTE OF TECHNOLOGY LADKRABANG

2009

KMITL-2009-EN-D-018-001

This material is reserved for educational use only, not allowed for commercial use.

Forbidden to modify the content, and cite the document when use.



COPYRIGHT 2009

FACULTY OF ENGINEERING

KING MONGKUT'S INSTITUTE OF TECHNOLOGY LADKRABANG

This material is reserved for educational use only, not allowed for commercial use.

Forbidden to modify the content, and cite the document when use.

Thesis Title	Ultra Wideband Circuit Design and Its Performance Analysis of Interference
Student	Mr. Risanuri Hidayat.
Student ID.	48060023
Degree	Doctor of Engineering
Program	Electrical Engineering
Year	2009
Thesis Advisor	Assoc. Prof. Dr. Kobchai Dejhan,
Thesis Co-Advisors	Assist. Prof. Dr. Phichet Moungnoul, Prof. Dr. Yoshikazu Miyanaga.

Abstract

This thesis presents about ultra wideband circuit design and its performance analysis of interference. A new method of ultra wideband (UWB) monocycle pulse generation and a gigahertz wideband analog multiplier are also proposed. The multiplier is based on MOS cascade operation circuit, and uses voltage to current mode operation. The inputs are in voltage mode and become in current mode after the multiplication. The V-I multiplier has gigahertz frequency response and can be applied to multiply the generated UWB pulse. The circuit is based on 0.18 μm CMOS technology simulated using HSPICE level 49 and operates in ± 1 V. Both the multiplier and the UWB pulse generation circuits have advantage in simplicity, and so are potentially lower costs. The simplicity, low cost and good performance of the circuit makes itself attractive for various UWB systems.

Some various modulations of impulse radio (IR) UWB, a new channel model based on the Saleh-Vanenzuela model for UWB communication and its bit error rates (BER) are presented. BER are analyzed using Binary Pulse Amplitude Modulation and measured over various bit rates. The result shows that monocycle pulse over LOS and NLOS channel gives the best bit rates.

หัวข้อวิทยานิพนธ์	การออกแบบวงจร Ultra wideband และความสามารถในการจัดการสัญญาณรบกวน
นักศึกษา	Risanuri Hidayat
รหัสนักศึกษา	48060023
ปริญญา	วิศวกรรมศาสตรดุษฎีบัณฑิต
สาขาวิชา	วิศวกรรมไฟฟ้า
พ.ศ.	2552
อาจารย์ที่ปรึกษา	รศ.ดร. กอบชัย เดชหาญ
อาจารย์ที่ปรึกษาร่วม	ผศ.ดร. พิเชฐ ม่วงนวล ศ.ดร. Yoshikazu Miyanaga

บทคัดย่อ

วิทยานิพนธ์นี้เสนอการออกแบบวงจร Ultra wideband และความสามารถในการจัดการสัญญาณรบกวน โดยวิธีการใหม่นี้เสนอการสร้างสัญญาณกำเนิดแบบโมโนไซเคิลพัลซและวงจรถูกอนาลอกในช่วงกิกะเฮิรต์ซ์ โดยวงจรถูกใช้วงจรมอสต้อแบบอนุกรมและทำงานในโหมดแรงดันไฟฟ้าถึงโหมดกระแส โดยอินพุตจะทำงานในโหมดแรงดันไฟฟ้าและจะทำงานในโหมดกระแสหลังจากผ่านวงจรถูก คุณลักษณะด้าน V-I ของวงจรถูก มีผลตอบสนองทางความถี่ในช่วงกิกะเฮิรต์ซ์และสามารถนำไปประยุกต์ใช้ในวงจรถูกของการสร้างสัญญาณ UWB วงจรนี้ใช้ $0.18 \mu\text{m}$ เทคโนโลยี CMOS และจำลองการทำงานด้วยโปรแกรม HSPICE level 49 และทำงานที่แรงดัน ± 1 โวลต์ โดยที่ทั้งวงจรถูกและวงจรถูกกำเนิดสัญญาณ UWB เป็นวงจรถูกที่สร้างง่ายและมีราคาต่ำ การมอดูเลทแบบต่าง ๆ ของ IR ของ UWB เสนอช่องสัญญาณใหม่ ขึ้นอยู่กับ แบบจำลองของ Saleh-Vanenzuela ของการสื่อสาร UWB และอัตราความผิดพลาดของบิต (BER) โดยที่ การวิเคราะห์อัตราความผิดพลาดของบิตใช้วิธี Binary Pulse Amplitude ซึ่งผลการทดลองแสดงเป็น monocycle pulse ต่อ ช่องสัญญาณ LOS และ NLOS เป็นอัตราบิตที่ดีที่สุด

ACKNOWLEDGMENT

The author would like to thank my advisor, Assoc. Prof. Dr. Kobchai Dejhan, for his guidance, encouragement, and support during my stay at King Mongkut's Institute of Technology Ladkrabang. His advice on technical matters and his guidance on my life were valuable. These same thanks attributes to my co-advisor, Assist. Prof. Dr. Phichet Moungnoul, for the guidance, appreciations, support. The same thanks also to my co-advisor, Prof. Dr. Yoshikazu Miyana, for the guidance, attentions, and support.

The author would like to thank King Mongkut's Institute of Technology Ladkrabang (KMITL) for not putting any constraints on this project whatsoever and for giving me the opportunity to be creative, explore new technology and pursue those directions I deemed appropriate. The author also would like to thank Gadjah Mada University for giving me support and opportunity to the study.

The author also would like to thank AUN/SEED-Net project that is mainly supported by the Japan International Cooperation Agency (JICA) for providing the financial resources under Collaborative Research between Research Center for Communication and Information Technology (ReCCIT), King Mongkut's Institute of Technology Ladkrabang (KMITL) and the Division of Media and Network technologies, Graduate School of Information Science and Technology, Hokkaido University, Japan.

Thanks my family for supporting the duration of the study.

Contents

Abstract	I
Acknowledgment	III
Contents.....	IV
Figure Contents	VI
Table Contents.....	IX
Chapter 1 INTRODUCTION	1
1.1. Overview	1
1.2. UWB Regulations.....	3
1.3. Research Scope and Dissertation Organization.....	4
Chapter 2 UWB PULSE GENERATION	6
2.1. Some Previous Researches	6
2.2. Gaussian Pulse for UWB.....	7
2.3. Principles and the proposed diagram.....	8
2.4. Circuit.....	9
2.4.1. MOS Capacitance.....	9
2.4.2 Gaussian pulse generation circuit.....	11
2.4.3. Differentiator Circuit.....	14
2.5. Simulation Result	16
2.6. Discussion	23
Chapter 3 THE UWB MODULATION	24
3.1.1. Bi-Phase Modulation.....	25
3.1.2. On-Off Keying.....	25
3.1.3. Pulse Amplitude Modulation.....	26
3.1.4. Pulse Position Modulation.....	26
3.1.5. Pulse Shape Modulation	27
3.2. Pulse Trains	28
3.3. UWB Spread Spectrum	29
3.3.1. Time Hopping.....	30
3.3.2. Direct Sequence.....	35

Chapter 4 UWB CHANNEL MODEL.....	37
4.1. Path Loss Model.....	37
4.2. Multipath Model.....	40
4.2.1. RMS Delay Spread.....	42
4.2.2. Multipath Model Comparison	42
4.2.2.1. 802.11 Model.....	42
4.2.2.2. Saleh-Valenzuela Model (S-V)	44
4.2.2.3. Δ -K Model.....	46
4.2.3. Proposed Intel Channel Model	49
Chapter 5 UWB RECEIVER	56
5.1. Noise and Interference.....	56
5.2. Multiplier for UWB.....	58
5.2.1. Multiplier Circuit Principle	58
5.2.1.1. Cascade MOS Operation.....	58
5.2.1.2. Four Quadrant V-I Multiplier	60
5.2.2. The Proposed Multiplier Circuits	61
5.2.3. Performance analysis.....	62
5.2.4. The Application for UWB Pulse	64
5.2.5. Discussion	70
5.3. IR-UWB Interference over Modified S-V Channel Model.....	70
5.4. BER Analysis Results	72
Chapter 6 CONCLUSIONS AND FUTURE RESEARCH	79
6.1. Conclusions	79
6.2. Future Research	80
REFERENCES.....	81
LIST OF PUBLICATIONS.....	85

Figure Contents

Figure 1. 1 MB-OFDM Band Structure and Channelization	2
Figure 1. 2 DS-UWB and the FCC requirement	3
Figure 1. 3 FCC spectral mask for indoor and outdoor UWB	4
Figure 1. 4 UWB Communication System.....	5
Figure 2. 1 Sinusoidal monocycle generator	6
Figure 2. 2 Gaussian pulse waveform	7
Figure 2. 3 Principles of monocycles Gaussian UWB pulse generation.....	8
Figure 2. 4 Proposed diagram of monocycles UWB signal generation	9
Figure 2. 5 MOS capacitances.....	10
Figure 2. 6 Gaussian pulse generation circuit and its detail.....	11
Figure 2. 7 CMOS inverter loading capacitance	12
Figure 2. 8 Fanout capacitance.....	13
Figure 2. 9 Self capacitance	13
Figure 2. 10 Propagation delay t_{PHL}	13
Figure 2. 11 CR differentiator	15
Figure 2. 12 Capacitance of MOS when D is connected to S	15
Figure 2. 13 MOS as CR differentiator	15
Figure 2. 14 Modified differentiator circuit	16
Figure 2. 15 The proposed circuit.....	17
Figure 2. 16 Time diagram in the Gaussian pulse generation circuit.....	17
Figure 2. 17 The generated Gaussian pulse.....	17
Figure 2. 18 The generated Gaussian monocycle pulse	20
Figure 2. 19 PSD of the derivative monocycle pulse in Figure 2.18(a).	20
Figure 2. 20 Power consumption of the circuit	20
Figure 2. 21 The improvement of the proposed circuit.....	22
Figure 2. 22 The time diagram of Figure 2.21.	22
Figure 2. 23 The normalized PSD of the derivative pulse Figure 2.22.	22

Figure 3. 1. BPM pulse shapes for ‘1’ and ‘0’ bits.....	24
Figure 3. 2. OOK pulses used for ‘1’ and ‘0’ bits	25
Figure 3. 3. PPM pulse shapes for ‘1’ and ‘0’ bits	27
Figure 3. 4. Examples of the pulse waveforms used for PSM modulation	28
Figure 3. 5. Spectrum of pulse train without (a) and with (b) randomizing techniques	30
Figure 3. 6. Time Hopping Pulse Position Modulation Principle.	34
Figure 3.7. Direct Sequence UWB pulse with Binary Phase Modulation.....	35
Figure 4. 1. Average power profile of Rayleigh model, taken from [23].....	41
Figure 4. 2. An illustration of channel impulse response [23].	43
Figure 4. 3. An illustration of exponential decay of mean cluster power and ray power within clusters (copied from [23]).....	43
Figure 4. 4. One channel realization generated from Δ -K model.....	46
Figure 4. 5. One LOS channel realization generated using the parameter in Table 4.8.	50
Figure 4. 6. One NLOS channel realization generated using the parameter in Table 4.9.	51
Figure 5. 1 UWB communication with channel and AWGN.....	57
Figure 5. 2 MOS operation.....	59
Figure 5. 3 Cascade MOS Operation.....	59
Figure 5. 4 Two-quadrant Multiplier.....	60
Figure 5. 5 Four-quadrants Multiplier	60
Figure 5. 6 The Proposed Multiplier Circuit	61
Figure 5. 7 DC Characteristics	63
Figure 5. 8 Frequency Response	63
Figure 5. 9 Transient simulation for 2 sine waves.....	63
Figure 5. 10 The UWB pulse generation circuit and its pulse	65
Figure 5. 11 The improvement of the proposed circuit and its pulse	66
Figure 5. 12 Two monocycle pulses multiplication	67
Figure 5. 13 The monocycle and its second derivative pulses multiplication.....	68
Figure 5. 14 Two UWB triplet pulses multiplication	69

Figure 5. 15 The UWB triplet and its second derivative pulses multiplication 69
Figure 5. 16 The generated channel model 72
Figure 5. 17 BER of the UWB pulses through the LOS and NLOS channel models . 74
Figure 5. 18 BER performance over AWGN channels 75



Table Contents

Table 1. 1 FCC radiation limits for indoor and outdoor UWB	3
Table 2. 1 Summary of the Gaussian pulse generation circuit.....	18
Table 2. 2 Delay time differences.....	18
Table 2. 3 Summary of the differentiator circuit and the circuit performances	21
Table 3. 1 Advantages and disadvantages of various modulation methods.....	28
Table 4. 1 RMS delay spread numbers suggested for the indoor channel	41
Table 4. 2 Simulated and measured results for Rayleigh model	44
Table 4. 3 Simulated and measured results for Saleh-Valenuela[23].	46
Table 4. 4 Simulated and measured results for Δ -K model evaluation using Intel's results.....	47
Table 4. 5 Simulated and measured results for LOS UWB channels.....	47
Table 4. 6 Simulated and measured results for NLOS UWB channels.....	47
Table 4. 7 Simulated and measured results for Intel model evaluation using Intel's results.....	51
Table 4. 8 Simulated and measured results for LOS UWB channels using Intel's model.....	52
Table 4. 9 Simulated and measured results for NLOS UWB channels using Intel's model.....	52
Table 4. 10 Example multipath channel characteristics and corresponding model parameters.	53
Table 4. 11 Summary of proposed channel model.....	54
Table 5. 1 Multiplier circuit specifications.....	64
Table 5. 2 Input signal of Figure 5.9	64
Table 5. 3 Channel model parameters.	71
Table 5. 4 Bit rates results.	73
Table 5. 5 BER performance in AWGN channels.	73

Chapter 1

INTRODUCTION

1.1. Overview

UWB firstly were developed as a military radar systems because they could “see through” trees and beneath ground surfaces. However, recently UWB technology has been focused on consumer electronics and communications. Ideal targets for UWB systems are low power, low cost, high data rates, precise positioning capability and extremely low interference [1].

The FCC (Federation Communication Commissions) granted the frequency range from 3.1 GHz to 10.6 GHz with very little emission power to UWB technology and therefore consolidated the legality of UWB technology. By the ideal targets of UWB systems, UWB is a promising technology for future high-speed wireless communications and has a great potential to penetrate the PC peripherals and consumer electronics market [2].

Research in UWB technology and UWB related devices is growth rapidly in recent year as estimation the potential market of UWB. Many industrial heavyweights, such as Intel, Texas Instrument (TI), Motorola, and Samsung participate to involve in this field. As a result an industrial standard is expected to be made. IEEE 802.15.3a, as a new high-speed wireless standard is still in the process, and will achieve up to 480 Mbps throughput.

UWB standard is provided by the IEEE project 802-15.3a task group with examples of two different UWB radio systems. First is based on MB-OFDM (Multi-Band Orthogonal Frequency Division Multiplexing) and another is based on Direct Sequence Code Division Multiple Access (DS-CDMA). The OFDM is led by Texas Instruments and Intel, and followed by Samsung Electronics, Panasonic, Hewlett Packard and many other companies. The DS-CDMA is supported by Motorola, ParthusCeva, etc. It is closest to an impulse radio. The two proposals, MB-OFDM, and DS-CDMA, are currently still competing in the IEEE802.15.3a working group, and the final results are expected to come out in the near future.

The MB-OFDM divides spectrum into 14 bands as shown in Figure 1.1. Multiband is dividing the available spectrum into several bands, each having a

minimum of 500 MHz of bandwidth, to comply with the FCC requirements. It introduces orthogonality in the frequency domain. In this case, the impulse radio has long pulses in each band, and the OFDM principle is used in each band.

The 14 bands span the range of 3168 to 10 560 MHz, divide the spectrum into 528-MHz bands, and then employs OFDM in each band to transmit data rates as high as 480 Mb/s. Each band consists of 128 subchannels of 4.125 MHz. MB-OFDM employs only QPSK modulation in each subchannel to allow low resolution in the baseband analog-to-digital (A/D) and digital-to-analog (D/A) converters (4–5 bits) [3].

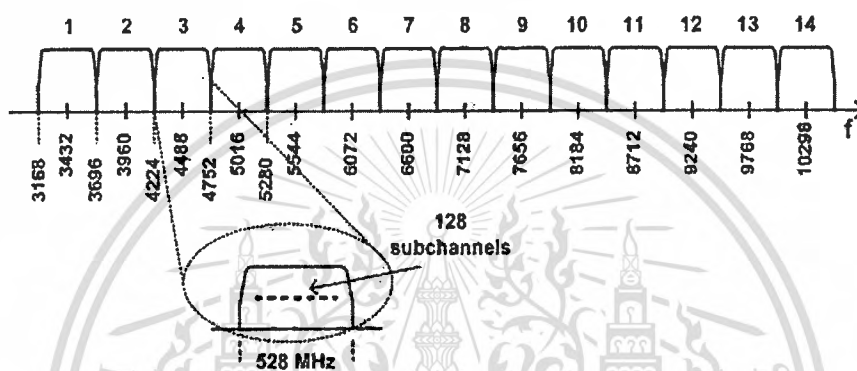


Figure 1.1 MB-OFDM Band Structure and Channelization

DS-SS uses the whole available spectrum as known as single-band. It transmits data with very short pulses (impulse radio). Impulse radio is carrier-less, so it only has base-band processing and no intermediate frequency (IF) processing is needed. This makes impulse radio devices much cheaper than other communication devices. In the impulse radio devices, no Local Oscillator is necessary; no up- or down- converters are needed. Therefore, the impulse radio devices are simple and of low cost, high speed, low power consumption, and small size. Figure 1.2 shows an impulse radio and its FCC requirements [4].

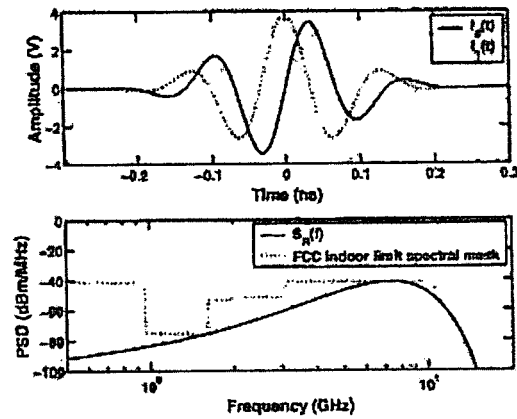


Figure 1. 2 DS-UWB and the FCC requirement

1.2. UWB Regulations.

In 1998, FCC recognized the importance of UWB technology and began the process of regulatory review. In February 2002, FCC made the formal rule that permits ultra wideband to operate under certain indoor and outdoor power spectral masks. The radiation limits by FCC are presented in Table 1.1 for indoor and outdoor data communication applications [5].

Table 1. 1 FCC radiation limits for indoor and outdoor UWB

Frequency in MHz	Indoor	Outdoor
	EIRP in dBm	EIRP in dBm
960 - 1610	- 75.3	-75.3
1610 - 1990	- 53.3	- 63.3
1990 - 3100	- 51.3	- 61.3
3100 - 10600	- 41.3	- 41.3
Above 10600	- 51.3	- 61.3

Figure 1.2 shows the current proposal for the spectral mask limits as well as the FCC masks as described in Table 1.1. It represents the masks for data communication applications for indoor and outdoor use. In all cases the maximum average power spectral density follows the limit of FCC Part 15 regulations (Federal Communications Commission, 2004).

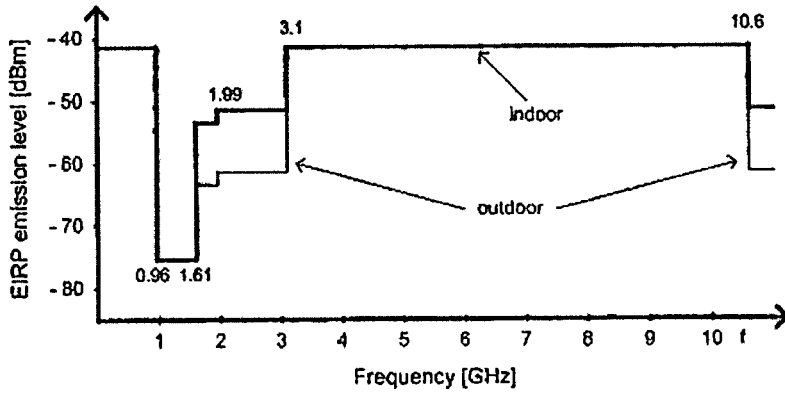


Figure 1.3 FCC spectral mask for indoor and outdoor UWB

1.3. Research Scope and Dissertation Organization

The UWB communication system can be delineated in Figure 1.3. On the transmitting side, the incoming data stream is modulated. But before this, it can be first encoded. All encoding methods for narrowband, such as convolution codes, block codes, turbo codes, etc., are all applicable to UWB systems. The UWB modulation types include time hopping pulse position modulation, time hopping pulse amplitude modulation, direct sequence pulse position modulation, multiple-band OFDM, etc.

On the receiving side, the UWB signal is first captured by a receiving antenna. Second, the signal is filtered with a matched filter, which is usually the same as the transmitting pulse shaping filter. Matched filter is also as Low Noise Amplifier (LNA). Then the signal is demodulated. The demodulation process is the inverse process of the modulation. After that the signal can be decoded. The decoding methods, such as Viterbi decoder, turbo decoder, and sequential decoder, which are used in narrowband communications, can also be applied in UWB systems. If the interleaving, scrambling, and puncturing are used in the transmitter, de-interleaving, de-scrambling, and de-puncturing should be conducted accordingly in the receiver.

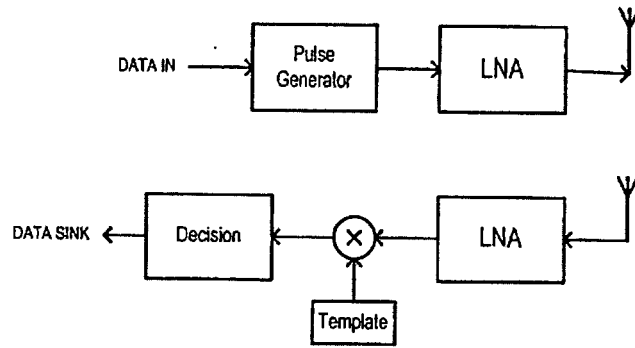


Figure 1. 4 UWB Communication System

As described previously that UWB communication system is divided into two camps, this research focuses on the DS-UWB. The scope of this research covers the UWB pulse generation, UWB modulation types, channel models, performances and interferences, etc. The dissertation is organized as follows. Chapter 2 discusses UWB pulse generation circuit design and it's fulfilled of FCC rules. Chapter 3 is about modulation types of the UWB communication system. Chapter 4 talks about UWB channel models. Chapter 5 studies the interference of the UWB communications. Chapter 6 summarizes the findings and concludes the dissertation.

Chapter 2

UWB PULSE GENERATION

2.1. Some Previous Researches

Ultra-Wideband (UWB) radio is defined as a wireless technology to transmit data over a wide spectrum of frequency bands with low power [6]. Since its signal has short pulse duration, high data rate can be achieved. It is considered as one of the next generation wireless communication systems. Federal Communications Commission (FCC) has released unlicensed 3.1-10.6 GHz frequency band for Ultra-Wideband (UWB) related applications [6].

Several monocycle pulse shapes were introduced [7]. Some researches have published pulse generators for UWB in circuit level [8,9,10,11]. Some papers have proposed transmitting scheme which gives a priority to avoid both complexity and high power analog components for UWB [12,13,14]. However, its power consumption is still relatively high. In this chapter, a new method to generate Gaussian monocycle by applying input transition. This proposed circuit has advantages that apply simple circuit and consumes low power. It applies MOS gates process that always needs delay [15]. The input transition is AND for a few nanoseconds. A Gaussian pulse is thus generated. A differentiator circuit is used to perform a monocycle pulse. The generation is simulated based on 0.18 μm CMOS technology. Figure 2.1 shows an example of the previous UWB monocycle generator [11].

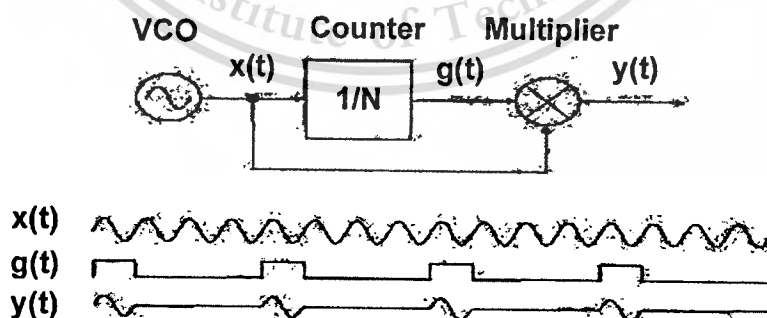


Figure 2. 1 Sinusoidal monocycle generator

2.2. Gaussian Pulse for UWB

Ultra Wideband (UWB) technology is defined by the Federal Communications Commission (FCC) as any wireless transmission scheme that occupies a fractional bandwidth $W/f_c \geq 20\%$ where W is the transmission bandwidth and f_c is the band center frequency, or more than 500 MHz of absolute bandwidth. The FCC recently approved the deployment of UWB on an unlicensed basis in the 3.1–10.6 GHz band subject to a *modified* version of Part 15.209 rules.

Some references have represented several kind formulas of Gaussian pulse [7,9,11]. The Gaussian pulse and its first derivative, which is usually called as monocycle has formula, respectively as follows;

$$x(t) = A_1 \cdot e^{-2\left(\frac{\pi t}{T_c}\right)^2} \quad (2.1)$$

$$x^{(1)}(t) = \frac{dx(t)}{dt} = A_2 t \cdot e^{-2\left(\frac{\pi t}{T_c}\right)^2} \quad (2.2)$$

$$f_c = \frac{1}{T_c} \quad (2.3)$$

where T_c is the width of the pulse, A_1 and A_2 are amplitudes, and f_c is the frequency center of the monocycle pulse. Figure 2.2 shows the Gaussian pulse waveform and monocycle of the pulse.

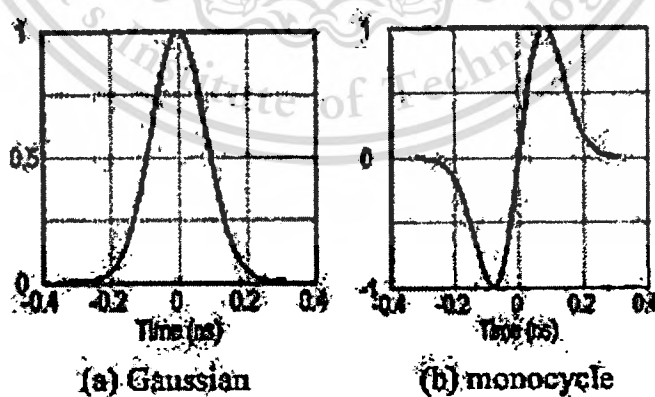


Figure 2. 2 Gaussian pulse waveform

2.3. Principles and the proposed diagram

The UWB generation applies at the *input* transition time. Figure 2.3 shows about the principles of the UWB monocycle pulse generation. Figure 2.3(a) is the step input. Figure 2.3(b) is the actual input and its inverting signal with delay. The delaying and inversion processes of the input are done in Figure 2.3(b), and the results are D and \bar{D} .

As shown in Figure 2.3(b), there is a little space that both D and \bar{D} are high. When D and \bar{D} are AND-ed, it will produce a Gaussian pulse, as shown in Figure 2.3(c). Finally, the Gaussian pulse then is differentiated to produce a Gaussian monocycle pulse, as shown in Figure 2.3(d).

Figure 4 proposes a diagram to generate the UWB Gaussian monocycle pulse. It is really simple diagram. It is comprised of CMOS inverters (NOT), NAND and a differentiator circuit. The CMOS inverters invert the input signal and produce a little space time that both D and \bar{D} are high. The signals D and \bar{D} are then AND-ed by a NAND circuit to generate a Gaussian pulse. A differentiator circuit differentiates the Gaussian pulse to generate a UWB monocycle pulse.

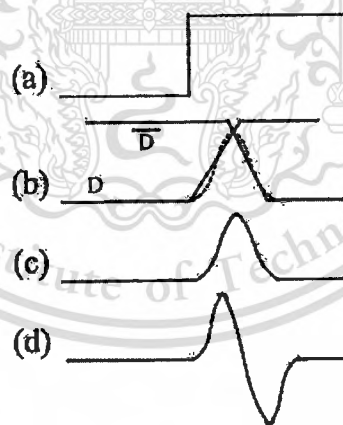


Figure 2. 3 Principles of monocycles Gaussian UWB pulse generation

- (a) Step input
- (b) Actual Input and its Inverting Signal
- (c) Gaussian pulse
- (d) Monocycle pulse

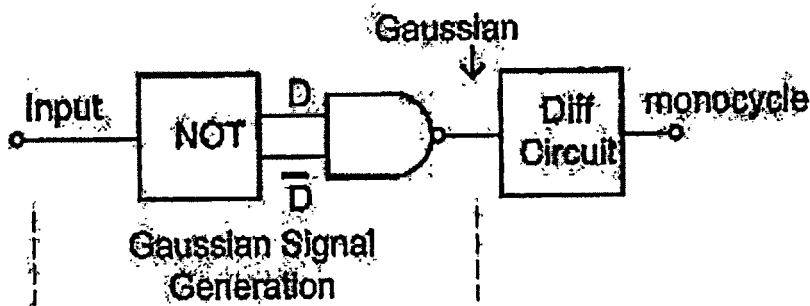


Figure 2. 4 Proposed diagram of monocycles UWB signal generation

2.4. Circuit

2.4.1. MOS Capacitance

This chapter explores the capacitances of MOS transistor. Figure 2.5 shows about capacitances between nodes of MOS transistor. C_{GD} , C_{GS} , C_{GB} , C_{DB} , and C_{SB} are respectively the capacitances between nodes gate (G) - drain (D), G - source (S), G - bulk (B), D-B and S-B.

There are two basic types of nonlinear or voltage-dependent capacitances in the structure: thin-oxide capacitances that are connected to gate, and junction capacitances, connected to bulk. In addition, there are two overlap capacitances, which are linear and voltage-independent, between gate-drain, and between gate-source.

The thin-oxide capacitances present between gate-source and between gate-drain., named C_{gs} and C_{gd} respectively. The capacitances usually have the same value, and can be expressed as [16,17],

$$C_{gs} = C_{gd} = C_g = \frac{1}{2} C_{ox} WL \quad (2.4)$$

$$C_{ox} = \frac{\epsilon_{ox} W}{t_{ox}} \quad (2.5)$$

where C_{ox} is the thin-oxide capacitance per unit area. W and L are channel width and channel length. ϵ_{ox} is the permittivity of the oxide and t_{ox} is the oxide thickness.

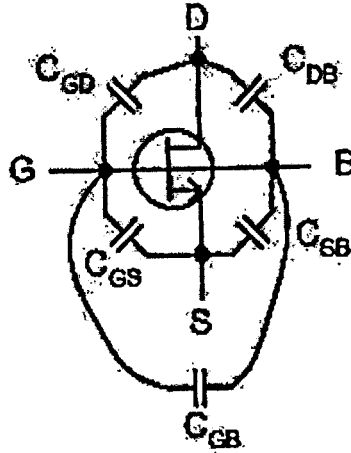


Figure 2. 5 MOS capacitances

The overlap capacitance, C_{OL} , is the capacitance of both side of gate that is comprised of the overlap capacitances between gate-drain (C_{OLGD}) and between gate-source (C_{OLGS}). These can be expressed as [17]

$$\begin{aligned} C_{OLGD} &= C_{GDO} \cdot W \\ C_{OLGS} &= C_{GSO} \cdot W \end{aligned} \quad (2.6)$$

C_{GDO} is the gate-drain overlap capacitances per unit gate width, and C_{GSO} is the gate-source overlap capacitances per unit gate width. The values are modeled in the SPICE simulation.

The junction capacitances happen in the capacitances of drain-bulk and source-bulk, named respectively C_{JDB} and C_{JSB} . The capacitances can be expressed as [16],

$$C_{JDB} = \frac{CJ \cdot A_D}{\left(1 - \frac{V_J}{PB}\right)^{MJ}} + \frac{CJSWG \cdot P_D}{\left(1 - \frac{V_J}{PB}\right)^{MJSWG}} \quad (2.7)$$

$$C_{JSB} = \frac{CJ \cdot A_S}{\left(1 - \frac{V_J}{PB}\right)^{MJ}} + \frac{CJSWG \cdot P_S}{\left(1 - \frac{V_J}{PB}\right)^{MJSWG}} \quad (2.8)$$

where CJ and $CJSWG$ are the source/drain bottom junction capacitance and the zero-bias gate-edge sidewall bulk junction capacitance, respectively. MJ and $MJSWG$ respectively are the grading coefficient of the bottom-wall junction capacitance and

grading coefficient of the gate-edge sidewall junction capacitance. PB is the built-in potential of the bottom-wall junction capacitance. A_D , A_S , P_D and P_S are the drain area, source area, drain perimeter and source perimeter, respectively. Finally, V_J is the junction voltage, voltage drop across the junction of the transistor.

2.4.2 Gaussian pulse generation circuit

Figure 2.6 shows the circuit to generate Gaussian pulse that is the detail of Figure 4. The NOT circuits invert *input* to become D and \bar{D} . It needs delay to invert *input*, so there is a little space time that both D and \bar{D} are high. The NAND output will be low if only if D and \bar{D} , are high, as illustrated in Figure 2.3. On the output (Gaussian node), a Gaussian pulse will be performed by the NAND circuit, as shown in Figure 2.6 (a).

Figure 2.6 (b) and Figure 2.6 (c) are the detail circuit of the NOT and the NAND, respectively. Some parameters of the MOS transistor in the circuit must be considered to get a precise delay, such that the Gaussian pulse can be generated from the circuit.

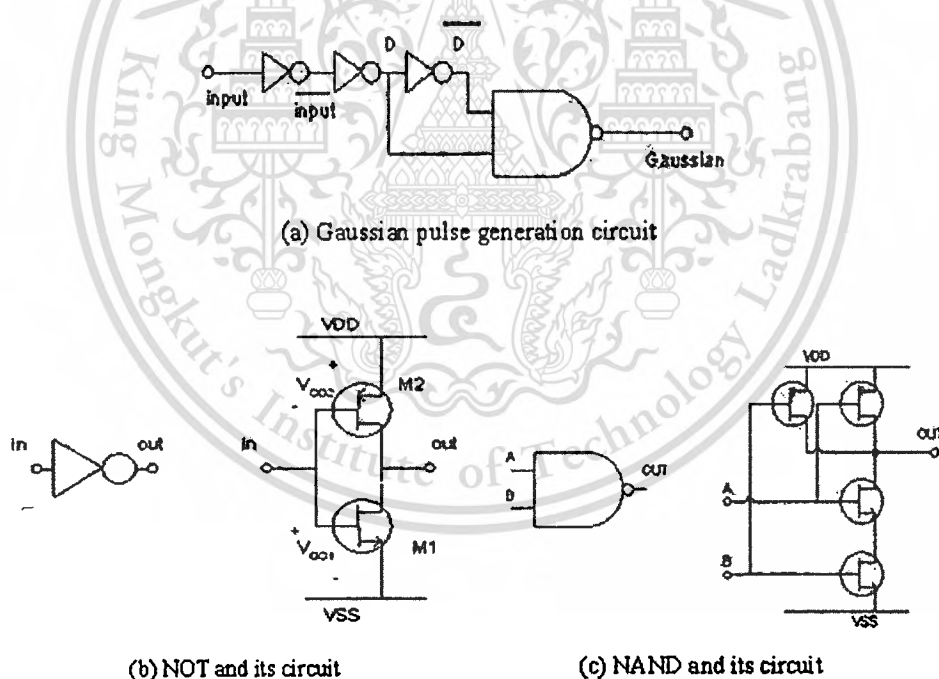


Figure 2. 6 Gaussian pulse generation circuit and its detail

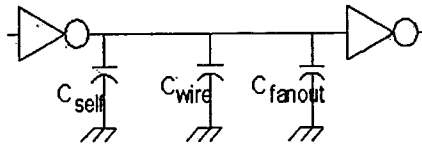


Figure 2. 7 CMOS inverter loading capacitance

Time delay of the inverter has been proposed [15]. The delay is the effect of the inverter capacitance, especially in high frequency, which is illustrated previously in Figure 2.5.

Figure 2.7 shows about the capacitance of the CMOS inverter. The capacitance is comprised of three components: the self-loading, the wire and the fanout capacitances [16]. For delay calculation, these individual quantities are summed altogether.

$$C_L = C_{self} + C_{wire} + C_{fanout} \quad (2.9)$$

where C_L is the total load capacitance.

C_{self} is the self capacitance and can be defined as the output capacitance of the first inverter, while C_{fanout} is fanout capacitance, that is the input capacitance of the second inverter in Figure 2.7. Between inverter, there is wire capacitance, C_{wire} . Since it is assumed that the wire is short, the wire capacitance is neglected.

Figure 2.8 illustrates about C_{fanout} that is derived from Figure 2.5. C_{fanout} is the capacitance connected to the input of the inverter. Since both PMOS and NMOS have thin-oxide and also overlap capacitances, C_{fanout} can be expressed as [16],

$$C_{fanout} = C_{gn} + C_{OLGDn} + C_{OLGSn} + C_{gp} + C_{OLGDP} + C_{OLGSp} \quad (2.10)$$

where C_{gn} and C_{gp} are the capacitances of the thin-oxide for MOS, as expressed in (2.4-2.5). C_{OLGD} and C_{OLGS} are the overlap capacitances between gate-drain and between gate-source respectively, and has been expressed in (2.6). The subscript either n or p identify for NMOS and PMOS respectively. If C_{GDO} and C_{GSO} values are the same, then $C_{OLGD} = C_{OLGS} = C_{OL}$. Therefore the equation (2.10) can be simplified as

$$C_{fanout} = (C_{ox} L)(W_n + W_p) + 2C_{OLn}W_n + 2C_{OLp}W_p \quad (2.11)$$

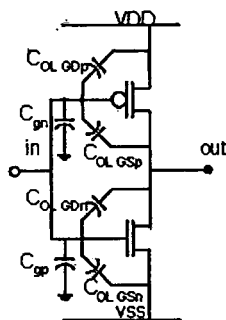


Figure 2. 8 Fanout capacitance

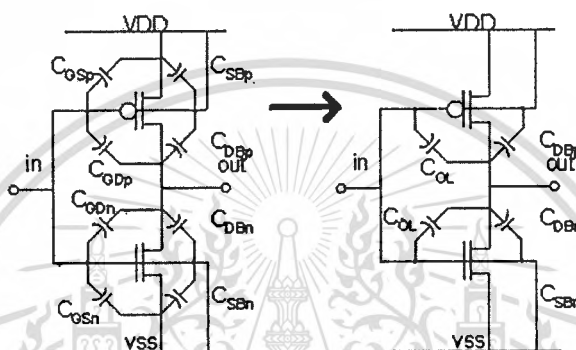


Figure 2. 9 Self capacitance

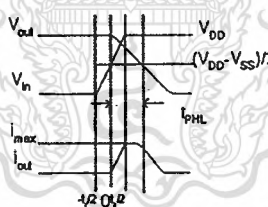


Figure 2. 10 Propagation delay t_{PHL}

The self-capacitance, C_{self} , is the capacitances connected to the output. Figure 2.9 illustrates the important terms to include in the self-capacitance, also derived from Figure 2.5.

Suppose that delay time (t_{PHL} or t_{PLH}) involves a transition to the 50% point, it can be assumed that the transistors are in saturation or cutoff. In either region, the thin-oxide gate-drain capacitance, C_{gd} is negligible [16]. The total self-capacitance can be expressed as the junction capacitances plus the overlap capacitances as follows,

$$C_{self} = 2C_{OLGDn} + 2C_{OLGDp} + C_{DBn} + C_{DBp} \quad (2.12)$$

where C_{OLGDn} and C_{OLGDp} are the overlap capacitances from gate-to-drain. These have a double value of the capacitance because of commonly referred as Miller effect modeling [16]. C_{DBn} and C_{DBp} are the one junction capacitance between drain-bulk per device. The capacitances are formulated in (2.7) and (2.8).

As t_{PHL} or t_{PLH} involves a transition to the 50% point, the delay for an inverter can be calculated as in equation (2.13), and illustrated in Figure 2.10.

$$t_{PHL} = R_{effNMOS} \frac{L}{W} C_L \quad (2.13)$$

$$t_{PLH} = R_{effPMOS} \frac{L}{W} C_L$$

where t_{PHL} and t_{PLH} are delay time from high to low and from low to high respectively, while R_{eff} is the effective resistance of the transistor. L , W and C_L have the same definition as previous mentioned.

2.4.3. Differentiator Circuit

The differentiator circuit differentiates the Gaussian pulse to get the differential of Gaussian pulse or monocycle, as declared in (2.2). Here, CR (Capacitor-Resistor) circuit is chosen. Figure 2.11 shows the CR differentiator. The output voltage in Figure 2.11 can be expressed as,

$$V_{out}(s) = \left(\frac{sRC}{1 + sRC} \right) V_{in}(s) \quad (2.14)$$

If $sRC \ll 1$, then

$$V_{out}(s) = sRCV_{in}(s)$$

$$v_{out}(t) = RC \frac{d.v_{in}(t)}{dt} \quad (2.15)$$

This research applies a MOS transistor as a capacitor. The reason is that the capacitance produced by the MOS is small, even in fF scale, fulfilling the requirement for the differentiator circuit. When drain (D) of the MOS is connected to source (S), $V_{DS}=0$, the transistor works in non-saturation region. Each capacitance as declared in 4.1, in non-saturation has expression as [16,17],

$$C_{GD} = C_{gd} + C_{Ol} \quad (2.16)$$

$$C_{GS} = C_{gs} + C_{Ol} \quad (2.17)$$

$$C_{GB} = 0 \quad (2.18)$$

$$C_{DB} = C_{JDB} \quad (2.19)$$

$$C_{SB} = C_{JSB} \quad (2.20)$$

Figure 2.12 shows the capacitance of MOS in such condition. Figure 2.13 shows about the MOS connection in the differentiator circuit. Capacitor C_1 is illustrated in Figure 2.12. V_C is the controlling voltage that leads the value of the junction voltage (V_J) that takes effect to the capacitance. Input in Figure 2.13 is Gaussian node that comes from the Gaussian pulse generation circuit (Figure 2.6(a)), and the output is a node called V_{out1} .

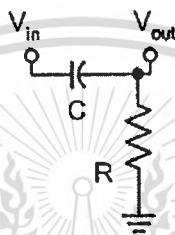


Figure 2.11 CR differentiator

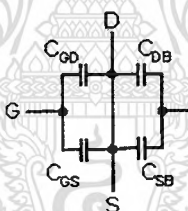


Figure 2.12 Capacitance of MOS when D is connected to S

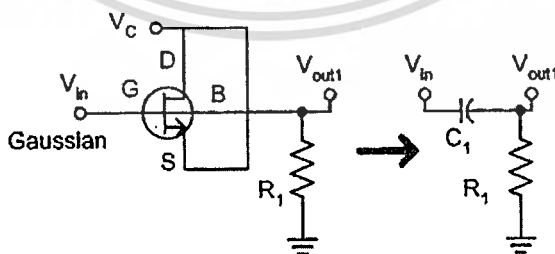


Figure 2.13 MOS as CR differentiator

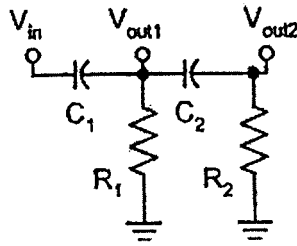


Figure 2. 14 Modified differentiator circuit

A modified differentiator circuit is used in the research to get the monocycle thicker. Figure 2.14 shows the modified circuit developed from Figure 2.13. CR filter is added but it has no effect to get more differential because C_2 is large. Derived from (2.14), the circuit has output expression as follow,

$$V_{out2}(s) = \left(\frac{sR_2C_2}{1 + sR_2C_2} \right) V_{out1}(s)$$

When desired that $V_{out2}(s) = V_{out1}(s)$, sR_2C_2 must be \gg , then

$$V_{out2}(s) \approx V_{out1}(s) \quad (2.21)$$

2.5. Simulation Result

Figure 2.15 shows about the proposed circuit. The circuit has advantages in simplicity that using few components. All circuits are simulated using HSPICE level 49 of $0.18\mu\text{m}$ CMOS parameter from mosis [18].

The Gaussian pulse generation circuit is shown in Figure 2.6 and drawn again in Figure 2.15. The input is a step signal or pulse that the width is in such a way that the Gaussian pulse can be performed. The output is a node called Gaussian (see Figure 2.6(a)).

L/W in CMOS inverters (NOT) and NAND used in this research are respectively $0.36/0.36\mu\text{m}$ and $0.18/0.27\mu\text{m}$.

Figure 2.16 shows the time diagram in Gaussian pulse generation circuit. When input coming to the circuit in Figure 2.6 is nearly ideal, after buffering in the first NOT, then CMOS inverters will convert input to become D and \bar{D} . D delay time

สำนักหอสมุดกลาง พระจอมเกล้าลาดกระบัง

(t_{PLH}) is approximately 140 ps delay (200 ps to 340 ns). And \bar{D} delay time (t_{PHL}) is approximately 40 ps delay (340.00 ps to 380 ps).

Figure 2.17 shows the Gaussian pulse generated from the circuit. The Gaussian pulse has 130.00 ps width (310 ps to 440 ps), amplitude 1.884mV, and 154 ps delay

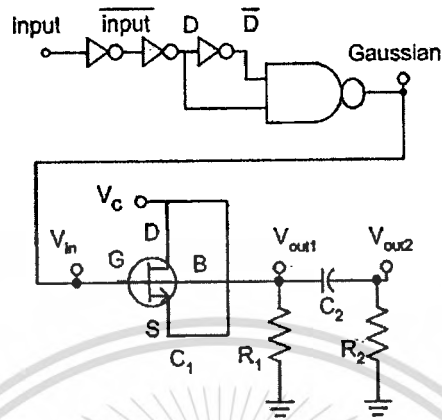


Figure 2.15 The proposed circuit.

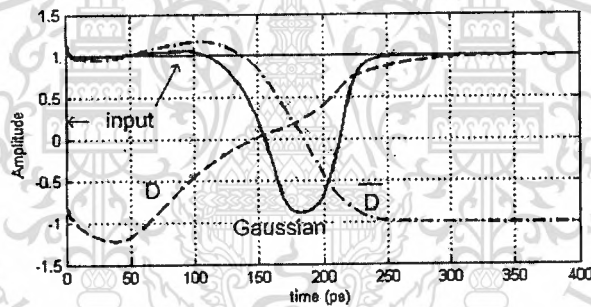


Figure 2.16 Time diagram in the Gaussian pulse generation circuit

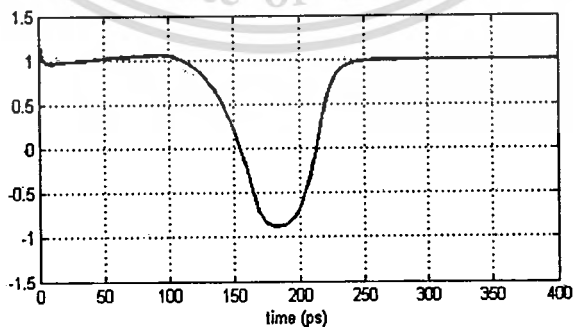


Figure 2.17 The generated Gaussian pulse

(200 ps to 354 ps) from input. The result also observes that input width minimum to be able to generate the Gaussian pulse is approximately 0.09 ns. Table 2.1 shows result summary of the circuit.

Table 2. 1 Summary of the Gaussian pulse generation circuit

L/W CMOS inverter	0.36/0.36 μm
L/W NAND	0.18/0.27 μm
Gaussian width	130 ps
Gaussian amplitude	884 mV
Gaussian delay	154 ps
input (pulse) width min.	0.09ns

There is a different value of delay between hand-calculation and circuit simulation. The hand-calculation using (2.13) and its root is applied to node D and \bar{D} . However, the difference is in tolerance that it may because some variable has been neglected. Delay time simulation is observed by graphic of input and D or \bar{D} in Figure 2.16. Table 2.2 shows about delay time in simulation and calculation. Note that $t_{\text{PLH}}(D)$ is delay time from low to high on the node D plus t_{PHL} of the first NOT (see Figure 2.6(a)), and $t_{\text{PHL}}(\bar{D})$ consider the fanout capacitance of NAND gate.

Table 2. 2 Delay time differences

	simulation	calculation
$t_{\text{PLH}}(D)$	140 ps	107 ps
$t_{\text{PHL}}(\bar{D})$	40 ps	25 ps

The capacitance of MOS transistor in Fig, 13 derived from (2.16) to (2.20) gives value of $C_1 \approx 0.10$ fF. However, the ac analysis of simulation shows that C_1 is equivalent to 0.07 fF. The values of $C_2 = 1\text{nF}$ and $R_2 = 1\text{M}$ is used in the modified differentiator circuit in Figure 2.14, such that (2.21) is fulfilled. The MOS capacitor has 0.18/0.18 μm of L/W. The MOS has the same parameter model as previous, with HSPICE level 49.

Figure 2.18 shows the time diagram of Gaussian monocycle pulse at the V_{out1} node. The figure shows that the graphic is the differential function of the input, as proposed in(2.15). Figure 2.18(a) is the monocycle with C_2 and R_2 , circuit in Figure

2.14. The monocycle has 200 ps width (300 ps to 500 ps), and peak to peak value 874 mV and 906 mV. Figure 2.18(b) is the monocycle without C_2 and R_2 , circuit in Figure 2.13. The figures show that C_2 and R_2 make the monocycle pulse more balance and thicker.

Figure 2.19 shows the normalized Power Spectral Density (PSD) of the derivative of the monocycle pulse from the circuit. If a monocycle pulse is transmitted, due to the derivative characteristics of the antenna, the output of the transmitter antenna can be modeled by the first derivative of the pulse [19]. When the time diagram is shown in Figure 2.18, called $y(t)$, the derivative can be achieved by the basics of differential calculus

$$x^{(1)}(t) = \lim_{dt \rightarrow 0} \frac{x(t + dt) - x(t)}{dt} \quad (2.22)$$

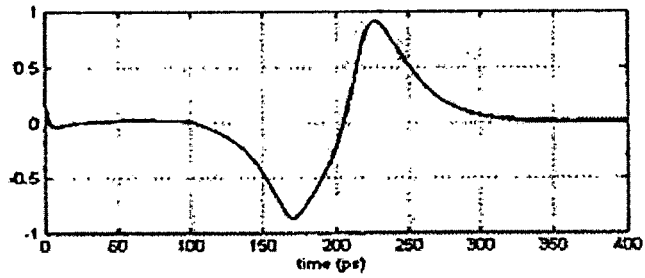
PSD of the deterministic power signal, $w(t)$, is

$$P(f) = \lim_{T \rightarrow \infty} \left(\frac{|X(f)|^2}{T} \right) \quad (2.23)$$

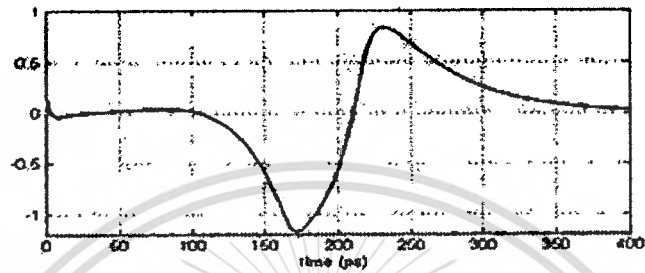
where T is the pulse spacing interval. $X(f)$ is the Fourier transform of the pulse, i.e. $x(t)$. $P(f)$ has units of watts per hertz. When $X(f)$ is attained, the peak emission frequency, i.e. f_M , can be found as the frequency at which the maximum value of $|X(f)|$. The normalized PSD can be defined as

$$|P(f)| = \frac{|X(f)|^2}{|X(f_M)|^2} \quad (2.24)$$

The normalized PSD in Figure 2.19 applies (2.24) in which $X(f)$ is the Fourier Transform of the differential of the pulse in Figure 2.18. The differentiation uses the equation in (2.22). The normalized PSD is used due to comply the FCC spectral mask of the pulse that is transmitted by antenna [6,19]. Figure 2.19 shows that PSD complies the spectral mask, unless it is over the tail of the frequency (10.6 GHz).



(a) with C2 and R2



(b) without C2 and R2

Figure 2.18 The generated Gaussian monocycle pulse

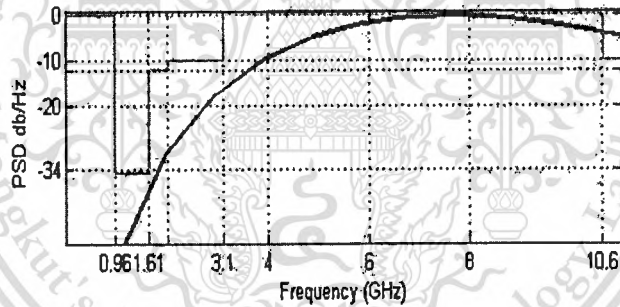


Figure 2.19 PSD of the derivative monocycle pulse in Figure 2.18(a).

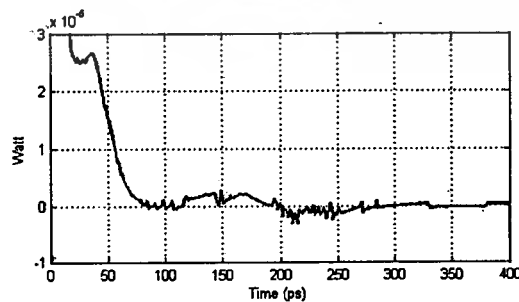


Figure 2.20 Power consumption of the circuit

Power maximum happens in the step input transition region, 0 to 1, (Figure 2.16), which is 5.35mW maximum (at time=0). In the other region the power is low, which is around 25 μ W or less. Figure 2.20 shows the low of power consumption of the proposed circuit.

The result shows that the proposed circuit succeeds to generate a Gaussian monocycle pulse with simple circuit, few components. The whole circuit consisted of only 11 MOS's and 2 CR components.

Figure 2.21 shows the improvement of the Gaussian monocycle pulse generation. The second monocycle pulse is generated after being delayed by two NOT's. Then both monocycles are connected to generate UWB pulse 4th derivative of the Gaussian pulse shape. The equation of the 4th derivative of the Gaussian pulse can be written as follows:

$$x^{(4)}(t) = \frac{dx^4(t)}{dt^4} = [A_3u^3 - A_4u] \cdot e^{-2u^2} \quad (2.25)$$

Table 2. 3 Summary of the differentiator circuit and the circuit performances

L/W MOS capacitor	0.18/0.18 μ m
C ₁ (MOS)	0.07 fF
C ₂	1 nF
R ₁ = R ₂	1 M Ω
Monocycle width (T _c)	200 ps
Peak to peak	- 0.87V to 0.91V
Power supply	\pm 1 V
Power consumption	25 μ W or less
Power maximum	5.35 mW

where $u = \pi t/T_c$ in (2.3). The values A₃ and A₄ are the amplitudes. The time diagram of node Gaussian02 in Figure 2.21 is the same as in Figure 2.17 with some delays. Figure 2.22 shows the time diagram of Gaussian monocycle pulse at the V_{out} node. The figure shows that the graphic has four peaks of signal which conducts as the fourth differential function of Gaussian pulse in (2.25).

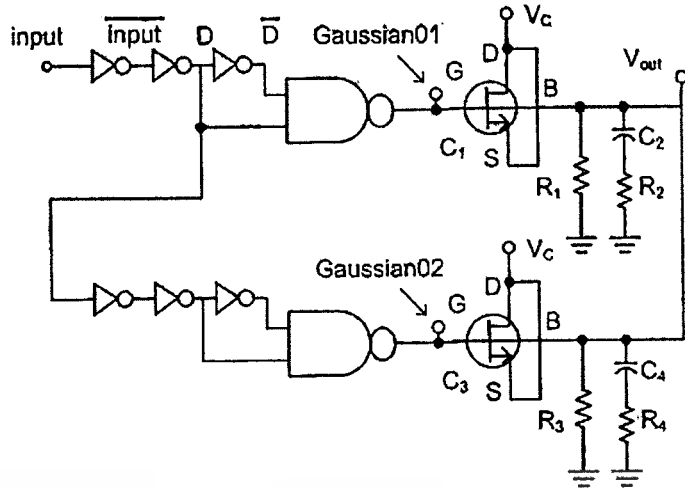


Figure 2. 21 The improvement of the proposed circuit.

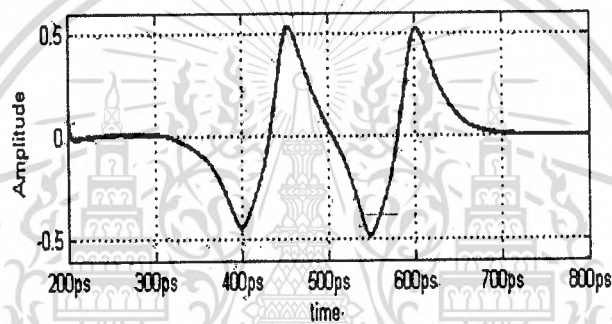


Figure 2. 22 The time diagram of Figure 2.21.

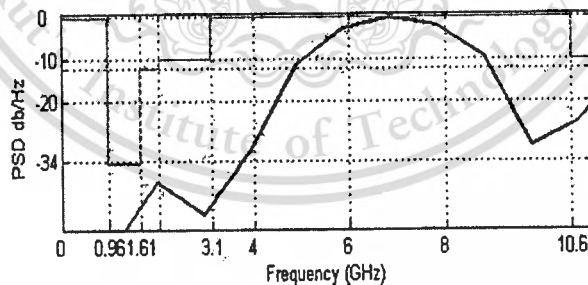


Figure 2. 23 The normalized PSD of the derivative pulse Figure 2.22.

Figure 2.23 shows the normalized Power Spectral Density (PSD) of the derivative of the UWB pulse from the circuit in Figure 2.21, using (2.22). As shown in Figure 2.23 the normalized PSD complies the FCC spectral mask.

2.6. Discussion

This design has advantage in simplicity and low cost power that are main focus in the UWB point of view. It applies 3 (three) NOTs, 1 (one) NAND, 2 (two) resistors, 1 (one) capacitor, and 1 (one) MOS as capacitor. Totally it implements 11 MOS. The supply is ± 1 volt, and 25 μ W for power consumption, as shown in Table 2.3.

As comparison, Azakkour [11] based on Choi [20] has proposed a gated pulse generator for UWB. Since it used VCO and on-off switch, it was more complicated than our design. The power is also larger, i.e. 243 mW. Kim [10] has also proposed a UWB pulse generator using digital CMOS circuit, which the average power consumption of the whole circuit was 15.4 mW and 675 mW at the pulse repetition frequency of 500 and 1 MHz, respectively. A wavelets generation circuit for UWB proposed by Gerrits [8], combined the output signals of four bipolar differential pairs to generate the second derivative of the Gaussian function as output signal. The circuit implemented 8 (eight) MOS's but it is excluding 4 (four) current sources applied in the circuit.

The normalized PSD of the UWB monocycle pulse generated by the circuit complies the FCC spectral mask unless a little band at the tail of frequency. The improvement circuit doubles the amount of the components. However it generates a pulse that complies the FCC requirements completely.

Chapter 3

THE UWB MODULATION

There are a variety of UWB modulation types used to build UWB systems. Some of them modulate information bits directly into very short pulses. UWB that is based on impulse radio concepts refers to the generation of a series of very short duration pulses, of the order of hundreds of picoseconds. Each pulse has a very wide spectrum, which must adhere to the spectral mask requirements. Continuous pulse transmission introduces a complication in that, without further signal processing at the transmitter, strong spectral lines will be introduced into the spectrum of the transmitted signal.

Since there is no IF (Intermediate Frequency) processing in such systems, they are often called baseband processing, or impulse radio system. Some well-known modulation types, such as time hopping pulse position modulation, time hopping pulse amplitude modulation, and direct sequence pulse amplitude modulation, are in the category of impulse radio. Several techniques are available for minimizing these spectral lines, the most common of which will be described later in this chapter.

3.1. Data Modulation

A number of modulation schemes may be used with UWB systems. The potential modulation schemes include both orthogonal and antipodal schemes.

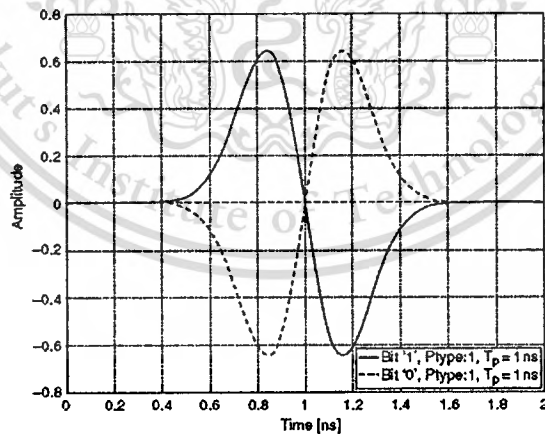


Figure 3. 1. BPM pulse shapes for '1' and '0' bits

3.1.1. Bi-Phase Modulation

The classic binary phase modulation (BPM) can be presented using e.g. two antipodal Gaussian pulses as shown in Figure 3.1.[5] The transmitted binary baseband pulse amplitude modulated information signal (i) is presented as

$$x(t) = d_j \cdot w_{ir}(t) \quad (3.1)$$

where $w_{ir}(t)$ represents the UBW pulse waveform, j represents the transmitted bit that $j=1$ then $d_j = 1$ and $j= '0'$ then $d_j=-1$.

$$d_j = \begin{cases} -1, & j = 1 \\ 1, & j = 1 \end{cases} \quad (3.2)$$

3.1.2. On–Off Keying

The next modulation scheme is binary on–off keying (OOK). By using (3.1), the following definition in (3.3) is used for this modulation to perform the waveform of the OOK modulation. The major difference between OOK and PAM is that nothing is transmitted in OOK when bit '0' is chosen.

$$d_j = \begin{cases} 0, & j = 0 \\ 1, & j = 1 \end{cases} \quad (3.3)$$

The major difficulty of OOK is the presence of multipath, in which echoes of the original or other pulses make it difficult to determine the absence of a pulse. Moreover, it cannot be extended to an M-ary modulation method, as PPM, PAM, and OPM. The on–off keying (OOK) is shown in Figure 3.2.[5]

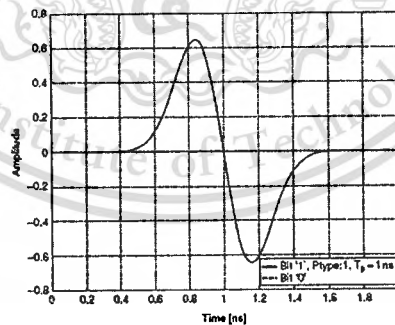


Figure 3. 2. OOK pulses used for '1' and '0' bits

3.1.3. Pulse Amplitude Modulation

Pulse amplitude modulation (PAM) for UWB can be also represented as shown in (3.1), where the pulse shape parameter $d_j = 1$ for $j=1$, and then $0 < d_j < 1$ for $j= '0'$.

The fact that, in general, an amplitude-modulated signal which has a smaller amplitude is more susceptible to noise interference than its larger amplitude counterpart. Furthermore, more power is required to transmit the higher amplitude pulse. Because of these reasons, amplitude modulation is not the preferred way for most shortrange communication.

In sinusoidal systems, amplitude-modulated systems are usually characterized by a relatively low bandwidth requirement and power inefficiency in comparison with angle modulation schemes. In most UWB applications the power efficiency is of high importance.

3.1.4. Pulse Position Modulation

With pulse position modulation (PPM), the chosen bit to be transmitted influences the position of the UWB pulse. It means that while bit '0' is represented by a pulse originating at the time instant 0, bit '1' is shifted in time by the amount of δ from 0. Analytically, the signal can be represented as

$$x(t) = w_{ir}(t - \delta \cdot d_j) \quad (3.4)$$

where d_j assumes the following values, depending on the bit chosen to be transmitted,

$$d_j = \begin{cases} 0, & j = 0 \\ 1, & j = 1 \end{cases} \quad (3.5)$$

The other variables have been defined previously. The value of δ could be chosen according to the autocorrelation characteristics of the pulse. The autocorrelation function can be analytically defined as [1]

$$R(\tau) = \int_{-\infty}^{+\infty} w_{ir}(t) \cdot w_{ir}(t + \tau) dt \quad (3.6)$$

For instance, to implement a standard PPM with orthogonal signals, the optimum value for δ (which we call δ_{opt}) will be the one which satisfies

$$\rho(\delta_{opt}) = \int_{-\infty}^{+\infty} w_{ir}(t) \cdot w_{ir}(t + \delta_{opt}) dt = 0 \quad (3.7)$$

Figure 3.3 shows a particular case of PPM transmission where data bit '1' is sent delayed by a fractional time interval $\delta < 1$, and data bit '0' is sent at the nominal time. The optimal modulation changes by using different pulse waveforms. The theoretical performance in an additive white Gaussian noise channel can be achieved with nonoverlapping, orthogonal pulses, specifically, the modulation index $\delta \geq T_p$.

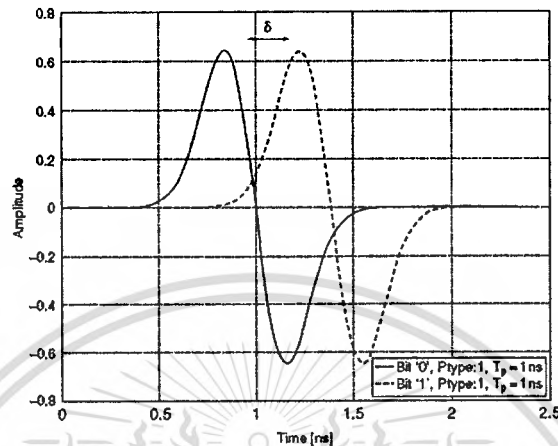


Figure 3. 3. PPM pulse shapes for '1' and '0' bits

3.1.5. Pulse Shape Modulation

Pulse shape modulation (PSM) uses different, orthogonal waveforms to represent bit '0' and '1'. The transmitted pulse can be represented as

$$x(t) = (t - d_j)w_{tr}^{(0)}(t) + d_j \cdot w_{tr}^{(1)}(t) \quad (3.8)$$

where d_j is defined as (2.11) and $w_{tr}^{(0)}$ and $w_{tr}^{(1)}$ represent two different waveforms. Figure 3.4 shows an example pair of PSM pulses. This case uses the first and the second derivatives of the Gaussian pulse. These two waveforms are orthogonal according to the definition given by the cross correlation of the two waveforms.

$$R(\tau) \Big|_{\tau=0} = \int_{-\infty}^{+\infty} w_{tr}^{(0)}(t) \cdot w_{tr}^{(1)}(t + \tau) dt = 0 \quad (3.9)$$

The orthogonality of the PSM signals depends on the pulse waveforms chosen to describe bit 0 and 1. For example, in the case of the first and second derivatives of the Gaussian pulse, it can be shown that the signals are orthogonal [5].

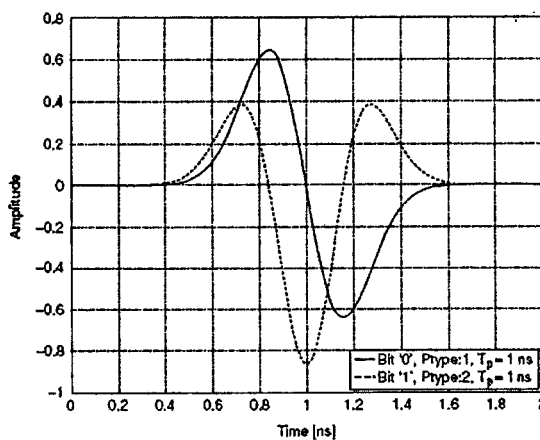


Figure 3. 4. Examples of the pulse waveforms used for PSM modulation

Table 3. 1 Advantages and disadvantages of various modulation methods.

Modulation	Advantages	Disadvantages
PPM	Simplicity	Needs fine time resolution
BPM	Simplicity	efficiency Binary only
PSM	Orthogonal for multiple access	Complexity
PAM	Simplicity	Noise immunity
OOK	Simplicity	Binary only, noise immunity

3.2. Pulse Trains

Continuous pulse generation leads to strong spectral lines in the transmitted signal at multiples of the pulse repetition frequency. Data modulation typically occurs in a number of conceptual stages. First is the generation of a pulse train. Then, a randomizing technique is applied to break up the spectrum of the pulse train. Finally, the data modulation is applied to carry the information.

Pulse trains are sequences of pulses, which will be able to transmit much larger volumes of information than a single set of pulses. In general, a simple and unmodulated pulse train $x(t)$ with a regular pulse output can be written as

$$s(t) = \sum_{n=-\infty}^{+\infty} p(t - nT) \quad (3.10)$$

where T is the period or the pulse-spacing interval and $p(t)$ is the basis pulse. The effects of changing the pulse duration and repetition rate of each pulse have been examined and the results are as follows:

- Increasing the pulse rate in the time domain increases the magnitude in the frequency domain (i.e., the pulse rate influences the magnitude of the spectrum).
- The lower the pulse duration in the time domain the wider the spectral width (i.e., the pulse duration determines spectral width).
- A random pulse-to-pulse interval produces a much lower peak magnitude spectrum than a regular pulse-to-pulse interval since the frequency components are unevenly spread over the spectrum and the addition of magnitude is less effective. Therefore, the pulse-to-pulse interval controls the separation of spectral components.

When a regular pulse train is used, energy spikes may cause interference with other RF systems at short range and limit the amount of useful energy transmitted. One method to overcome these spectral peaks is to “dither” the transmitted signal by adding a *pseudo-random noise* (PN) codes to add an offset to the signal. Since these codes are known and easily reproducible at the receiver, the problem for the receiver becomes mostly acquisition of the signal, but tracking is made much easily.

3.3. UWB Spread Spectrum

There are mainly two main approaches to randomizing the pulse train, Time Hopping (TH) and Direct Sequence (DS) techniques. The spectrum of a pulse train with and without randomizing techniques is depicted in Figure 3.5 [5]. Figure 3.5(a) shows the spectrum of a simple pulse train. As it can be seen, the spectrum contains strong spectral lines at multiples of the pulse repetition frequency.

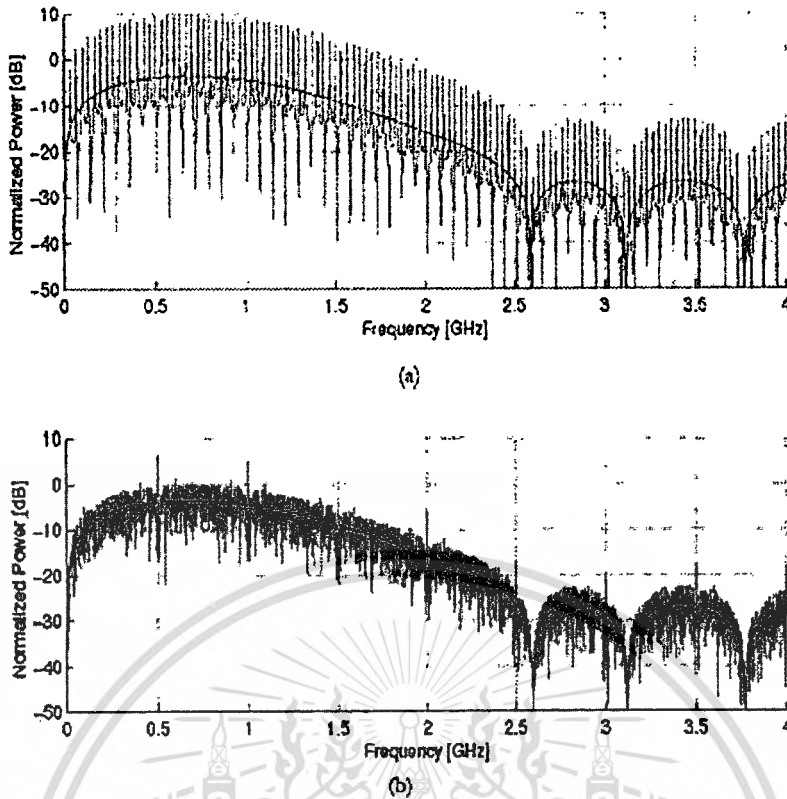


Figure 3. 5. Spectrum of pulse train without (a) and with (b) randomizing techniques

Randomizing the position in time of the generated pulses using data modulation and other randomizing techniques will affect the spectrum in such a way that the energy spikes are spread all over the spectrum, which is therefore smoothed. Figure 3.5(b) shows the spectrum of a pulse train that includes time hopping based randomization.

3.3.1. Time Hopping

In a time hopping system, an impulse signal is transmitted in short bursts pseudo-randomly, and the receiver knows beforehand when to expect the burst. Currently, many researches typically are based on PPM using Time Hopping as the basis for an UWB communication system. Pulse Position Modulation can be modeled as [21]

$$S^{(k)}(t) = \sum_j w(t - jT_f - c_j^{(k)}T_c - \delta d_{[j/N_s]}^{(k)}) \quad (3.11)$$

where $S^{(k)}$ is the k^{th} transmitted signal in multi-user system. $w(t)$ represents the transmitted waveform. T_f is the pulse repetition time or frame time. j is the j^{th} waveform that sits at the beginning of each time frame. Pseudonoise Time Hopping is to eliminate collisions in multiple accessing. $c_j^{(k)}$ is the j^{th} code of the k^{th} user's PN sequence. T_c is a time-shift unit incurred by the PN sequence. δ is referred to modulation index in pulse position modulation (PPM), which is a time-shift unit incurred by the binary symbol $d_{[j/N_s]}^{(k)} \in \{0,1\}$. $d_j^{(k)}$ is the primary data sequence of the transmitter. Data are transmitted every N_s monocycles per symbol and the symbol δ is the time shift that applies to the monocycle. So, the j^{th} monocycle nominally starts at time $(+jT_f + c_j^{(k)}T_c + \delta d_{[j/N_s]}^{(k)})$.

There are three components structure of time shift, i.e. Uniform Pulse Thin Spacing, Pseudorandom Time Hopping, and Data Modulation. Uniform Pulse Thin Spacing as a pulse train of the form $\sum_{j=-\infty}^{+\infty} w(t - jT_f)$ in (3.11) consists of monocycle pulses spaced T_f seconds apart in time. The frame time or pulse repetition time T_f typically may be a hundred to a thousand times the monocycle width, with its largest value constrained in part by the stability of the available clocks. The result is a signal with a very low duty cycle. Multiple-access signals composed of uniformly spaced pulses are vulnerable to occasional *catastrophic collisions* in which a large number of pulses from two signals are received at the same time instants, much as might occur in spread ALOHA systems.

Pseudorandom Time Hopping is used for eliminating damaged collisions in multiple accessing. Each link (indexed by k in (3.11)) is assigned a distinct pulse shift pattern $\{c_j^{(k)}\}$ which is referred as a *time hopping code*. These hopping codes $\{c_j^{(k)}\}$ are periodic pseudorandom codes with period N_p , i.e., $c_{j+iN_p}^{(k)} = c_j^{(k)}$ for all integers j and i . Each code element is an integer in the range

$$0 \leq c_j^{(k)} < N_h \quad (3.12)$$

The time hopping code therefore provides an additional time shift to each pulse in the pulse train, with the j^{th} monocycle undergoing an added shift of $c_j^{(k)} T_c$ seconds.

Hence the added time shifts caused by the code are discrete times between 0 and $N_h T_c$ seconds. It is further assumed that

$$N_h \cdot T_c \leq T_f \quad (3.13)$$

Hence the ratio $N_h T_c / T_f$ indicates the fraction of the frame time T_f over which time-hopping is allowed. Since a short time interval is required to read the output of a monocycle correlator and to reset the correlator, we assume that $N_h T_c / T_f$ is strictly less than one. If $N_h T_c$ is too small, then catastrophic collisions remain a significant possibility. Conversely, with a large enough value of $N_h T_c$ and well designed codes, then the multiple-access interference in many situations can be modeled as a Gaussian random process.

Because the hopping code is periodic with period N_p , the waveform $\sum_j w(t - jT_f - c_j^{(k)} T_c)$ is periodic with period

$$T_p = N_p \cdot T_f \quad (3.14)$$

One effect of the hopping code is to reduce the power spectral density from the line spectral density ($1/T_f$ apart) of the uniformly spaced pulse train down to a spectral density with finer line spacing $1/T_p$ apart.

Data Modulation: The data sequence $d_j^{(k)}$ of transmitter k is a binary (0 or 1) symbol stream that conveys information in some form. Since this is an *oversampled* modulation system with N_s monocycles transmitted per symbol, the modulating data symbol changes only every N_s hops, and assuming that a new data symbol begins with pulse index $j = 0$, the index of the data symbol modulating pulse j is $\lfloor j / N_s \rfloor$. (Here the notation $\lfloor z \rfloor$ denotes the integer part of z .) In this modulation method, when the data symbol is 0, no additional time shift is modulated on the monocycle, but a time shift of δ is added to a monocycle when the symbol is 1. Other forms of data modulation can be employed to benefit the performance of the synchronization loops, interference rejection, implementation complexity, etc. The data modulation further smoothes the power spectral density of the pseudorandom time-hopping modulation.

In this modulation format, a single symbol has duration $T_s = N_s T_f$. For a fixed

frame (pulse repetition) time T_f the binary symbol rate R_s determines the number N_s of monocycles that are modulated by a given binary symbol, via the equation

$$R_s = \frac{1}{T_s} = \frac{1}{N_s \cdot T_f} \text{ sec}^{-1} \quad (3.15)$$

In the receiver, when N_u links are active in this multiple-access system, then the received signal $r(t)$ can be modeled as

$$r(t) = \sum_{k=1}^{N_u} A_k s^{(k)}(t - \tau_k) + n(t) \quad (3.16)$$

in which A_k models the attenuation of transmitter k 's signal over the propagation path to the receiver, and τ_k represents time asynchronisms between the clocks of transmitter k and the receiver. The waveform $n(t)$ represents white Gaussian receiver noise. When it is assumed that the receiver is only received the data sent by transmitter 1, if only that signal is present, then

$$r(t) = A_1 s^{(1)}(t - \tau_1) + n(t) \quad (3.17)$$

When appropriately synchronized, e.g., having learned the value of τ_1 (or at least $\tau_1 \bmod N_p \cdot T_f$), the receiver can determine a sequence $\{T_i\}$ of time intervals, with interval T_i containing the waveform representing data bit $d_i^{(1)}$ or $d_{i \bmod N_p}^{(1)}$. When perfectly synchronized to the first signal, the receiver is then confronted with a standard hypothesis testing problem,

$$H_d : r(t) = A_1 w_{bit}(t - \delta \cdot d) + n(t) \quad (3.18)$$

in which d is either 0 or 1, and the observation is over $t \in T_i$. The bit waveform in this time interval is given by

$$w_{bit}(t) = \sum_{j=i \cdot N_s}^{(i+1)N_s-1} w(t - jT_f - c_j^{(1)} \cdot T_c - \tau_1) \quad (3.19)$$

The optimal receiver for this single signal in additive white Gaussian noise is simply a bit-duration correlator employing

$$v_{bit}(t) = w_{bit}(t) - w_{bit}(t - \delta)$$

$$v_{bit}(t) = \sum_{j=i.Ns}^{(i+1)Ns-1} v(t - jT_f - c_j^{(1)}T_c - \tau_1) \quad (3.20)$$

as a template signal, where the embedded one-pulse template signal is

$$v(t) = w(t) - w(t - \delta) \quad (3.21)$$

The corresponding optimal decision rule is

$$H_o \text{ true} \Leftrightarrow \underbrace{\int_{\epsilon T_i} r(t)v_{bit}(t)dt}_{\alpha} > 0 \quad (3.22)$$

When more than one link is communicating in this multiple-access system, the optimal processor for receiving the desired signal is not of the form (3.22), but is a complicated processing structure that takes advantage of all of the receiver's knowledge concerning the form of the interfering signals [22].

Figure 3.6 shows pulse train of UWB pulse with Time Hopping and Pulse Position Modulation (TH-PPM UWB). First is the uniform pulse train with neither modulation nor dithering, or $c_j^{(k)}T_c = 0$ and $\delta d_{[j/Ns]}^{(k)} = 0$. Second row is that the pulse has been shifted to hop position 3 of 8 possible hop positions. Finally, the bottom is the pulse in 4-ary PPM with data 10.

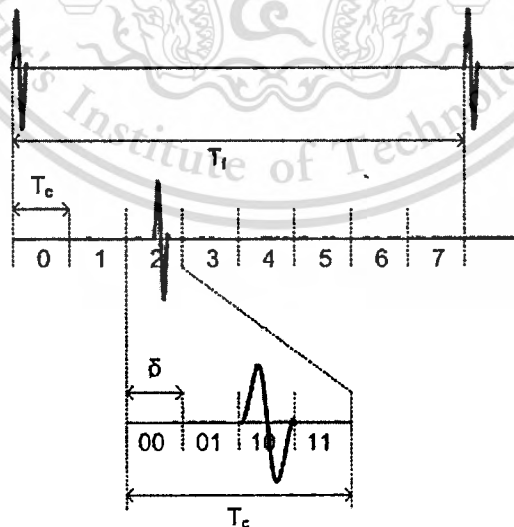


Figure 3. 6. Time Hopping Pulse Position Modulation Principle.

The binary pulse amplitude modulation (PAM) can be presented using antipodal Gaussian pulses. The transmitted binary baseband pulse amplitude modulation information pulse can be presented as

$$S^{(k)}(t) = \sum_j d_j^k \cdot w(t - jT_f - c_j^{(k)}T_c) \quad (3.23)$$

All notations have same means as those in (3.11). j is the bit transmitted, and $d_j^k \in \{-1, +1\}$ is the binary symbol. The main difference between TH-PPM and TH-PAM is that for the TH-PAM scheme the information symbol is imposed on the amplitude of the transmitted pulse, but for the TH-PPM scheme the information symbol is imposed on the beginning time of the transmitted pulse.

3.3.2. Direct Sequence

Using DS techniques, a pseudo-random code is used to spread the data bit into multiple chips, as well as in conventional DS spread spectrum systems. In the case of UWB systems, the pulse waveform takes the role of the chip in DS. Meanwhile PPM modulation is intrinsically a time hopping technique since the bit value is given by the position of the pulse in a transmission slot, the DS spreading approach has been studied for PAM, OOK and PSM modulation schemes. The use of the DS technique as a spreading approach would create a hybrid DS/TH configuration of the signal. The rectangular waveform indicates the individual chip elements. The modulated information signal $s(t)$ for the k^{th} user can be presented as

$$S^{(k)}(t) = \sum_{j=0}^{N-1} w(t - jT_c) c_j^{(k)} d_j^{(k)} \quad (3.24)$$

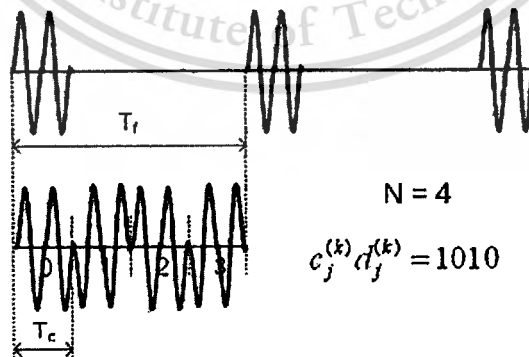


Figure 3.7. Direct Sequence UWB pulse with Binary Phase Modulation

As in (3.11), $S^{(k)}$ is the k th transmitted signal in multi-user system. j is the j th waveform that sits at the beginning of each time frame. $c_j^{(k)}$ is the j th code of the k th user's PN code. $w(t)$ is the pulse waveform. N represents the number of pulses to be used per data bit, and T_c is the chip length. The pseudo random code is bipolar assuming values $\{-1,+1\}$. The bit length is $T_f = NT_c$.

Figure 3.7 shows a pulse train example of Direct Sequence UWB pulse with Binary Phase Modulation (DS-BPM UWB). The uniform pulse train with neither modulation nor spreading is in the first. The bottom is about the pulse that has been spreaded by PN $c_j^{(k)} = 1010$ or $N = 4$, and data $d_j^{(k)} = 1$.



Chapter 4

UWB CHANNEL MODEL

Since UWB signals take ultra wide frequency bandwidth, they can achieve very fine time and range resolution. The capacity and performance of UWB communication systems can also be improved by taking advantage of RAKE receivers, which collect the signals coming from different paths and form a combined signal with better SNR. However, this SNR improvement or UWB communication system performance improvement by RAKE receiver is dependent upon the characteristics of the UWB propagation channel. So the characteristics of UWB propagation channel are very interesting to UWB researchers.

A considerable amount of research has been conducted in modeling UWB signal propagation channels so far. Some representative models are Intel model, Δ -K model, and so on. [23]. As a background, path loss model will be discussed in this chapter. Then multipath models will be discussed since some models have been proposed for wide band communications. Finally, the channel model from Saleh-Vanenzuela proposed and modified by intel [23] will be discussed since the model is used in many UWB communication researches. Most of content in this chapter are taken from [23].

4.1. Path Loss Model

Path loss or path attenuation is the attenuation undergone by an electromagnetic wave in transit between a transmitter and a receiver in a communication system. Path loss may be due to many effects, such as: free space loss, refraction, reflection, diffraction, clutter, aperture-medium coupling loss, and absorption [1].

Free space loss is the major loss of energy due to the spreading out of the wavefront as it travels away from the transmitter. As the distance increases the area of the wavefront spreads out, much like the beam of a torch. This means the amount of energy contained within any unit of area on the wavefront will decrease as distance increases. By the time the energy arrives at the receiving antenna the wavefront is so spread out that the receiving antenna extends into only a very small fraction of the wavefront.

Refraction is in the general case, as redirection of a wavefront passing through (a) a boundary between two dissimilar media or (b) a medium having a refractive index

that is a continuous function of position (e.g., a graded index optical fiber). For two media of different refractive indices the angle of refraction is closely approximated by *Snell's law*.

Reflection is the abrupt change in direction of a wave front at an interface between two dissimilar media so that the wave front returns into the medium from which it originated. Reflection may be *specular* (mirror-like) or *diffuse* (i.e., not retaining the image, only the energy) according to the nature of the interface. Depending upon the nature of the interface (i.e., dielectric-conductor or dielectric-dielectric) the phase of the reflected wave may or may not be inverted.

Diffraction is the *spreading out* of waves. All waves tend to spread out at the edges when they pass through a narrow gap or past an object. The wave spreads out or bends round a corner, such that it diffracts around the corner. A narrow gap is one which is about the same size as the wavelength of the electromagnetic wave or less. The longer the wavelength of a wave the more it will diffract.

Wave clutter is disorganized wave propagation due to a rough surface or interface. The mechanisms leading to clutter are not well known so far, and they are a lot more complex compared with the narrowband case. Understanding the phenomenology of electromagnetic interactions between very short pulses and the complex dielectric ground surface provides an important input to the design of UWB systems, leading to improved clutter cancellation and improved detection performance. The roughness considerably influences the spectral content of the response.

Coupling loss is the loss that occurs when energy is transferred from one medium to another. Aperture-medium coupling loss is the difference between the theoretical gain of the antenna and the gain that can be realized in operation. Aperture-to-medium coupling loss is related to the ratio of *scatter angle* to *antenna beamwidth*.

Absorption is the conversion of the transmitted energy into another form, usually thermal in the transmission of electrical, electromagnetic, or acoustic signals. Absorption is one cause of signal attenuation. The conversion takes place as a result of interaction between the incident energy and the material medium, at the molecular or atomic level.

There have been several proposed path loss models in the literature [1]. Assuming perfect isotropically radiating antennas at the transmitter and receiver the received power as a function of frequency can be expressed as [1]

$$P_R(f) = \frac{P_T(f)G_T(f)G_R(f)c^2}{(4\pi.d)^2 f^2} \quad (4.1)$$

where $P_T(f)$ is the average transmit power spectral density, c is the speed of light, $G_T(f)$ and $G_R(f)$ are the transmit and receive antenna frequency responses, respectively. Clearly, (4.1) depends on the frequency response of the antennas, which may be difficult to generalize, especially when we are dealing with wideband signals. However, the present regulations for UWB requires the transmitter to meet a certain electric field strength limit at a specified range, which is equivalent to a total, limited transmit power spectral density.

It is desirable to have the product $P_T(f).G_T(f)$ to be flat within the bandwidth of interest. As first-order approximation, a flat frequency response isotropic antenna is considered. A perfectly flat UWB waveform occupying the band $f_c - W/2$ to $f_c + W/2$ with power spectral density P_{av}/W and a flat frequency response of the receiving antenna with constant gain across the whole bandwidth (G_R) is considered. The total average received power at the output of the receiving antenna is given by

$$P_{Rav} = \int_{f_c - W/2}^{f_c + W/2} P_R(f) df$$

$$P_{Rav} = \frac{P_{av} G_R c^2}{W(4\pi.d)^2} \left(\frac{1}{f_c - W/2} - \frac{1}{f_c + W/2} \right)$$

$$P_{Rav} = \frac{P_{av} G_R c^2}{W(4\pi.d)^2} \left(\frac{1}{f_c - (W/2 f_c)^2} \right) \quad (4.2)$$

$$P_{Rav} = P_{av}^{NB} \left(\frac{1}{f_c - (W/2 f_c)^2} \right) \quad (4.3)$$

where

$$P_{av}^{NB} = \frac{P_{av} G_R c^2}{W(4\pi.d)^2} \quad (4.4)$$

Here, (4.4) corresponds to the well-known, narrowband, free space path loss model equation. The second term indicated in (4.3) accounts for the difference between the narrowband and wideband models. For the largest fractional bandwidth allowed by current UWB regulations (occupying 3.1–10.6 GHz), P_{Rav} will differ from $P_{NB av}$ by only 1.5 dB, and this difference becomes smaller for smaller fractional

bandwidths. Also note that FCC rules result in $W < 2fc$, so the singularity in the above equation can be ignored at $W = 2fc$.

Alternatively, we can repeat the above analysis for a receiver antenna response of the following form

$$GR(f) = \frac{4\pi \cdot A_R f^2}{c^2} \quad (4.5)$$

where A_R is the effective area of the antenna, when the antenna has a fixed effective aperture). This type of response yields a greater gain for higher frequencies. In this case the above analysis results in the average received power given by

$$P_{Rav} = \frac{P_{av} 4\pi \cdot A_R}{(4\pi \cdot d)^2}$$

$$P_{Rav} = \left[\frac{P_{av} \cdot c^2}{(4\pi \cdot d)^2 f_c^2} \right] \left[\frac{4\pi \cdot A_R \cdot f_c^2}{c^2} \right] \quad (4.6)$$

$$P_{Rav} = P_{av}^{NB} G_R(f_c)$$

where $G_R(f_c)$ is the antenna gain at the center frequency of the transmitted waveform. Therefore, it appears that the narrowband model can be used to approximate the path loss for a UWB system.

4.2. Multipath Model

Time domain models for UWB systems can be expressed as the following channel impulse response model:

$$h(t) = \sum_{l=0}^{L-1} \alpha_l \delta(t - \tau_l) \quad (4.7)$$

where α_l is the amplitude fading factor on path l (could be complex), τ_l is the random delay of path l , L is the number of multipath components, and $\delta(t)$ is the Dirac delta function. There are several parameters that need to be defined to complete this particular model, and each will be addressed in the following subsections.

Table 4. 1 RMS delay spread numbers suggested for the indoor channel

Application	Delay spread	Comments
WPAN (ITU P.1238)	RMS values: 70 nsec for Residential 100 nsec for office 150 nsec for commercial	WSSUS model with tap-delay line and Gaussian distributed taps
802.11 LAN for evaluating HRb proposals	25 nsec 100 nsec 250 nsec	WSSUS model with tap-delay line and Gaussian distributed taps with zero mean (Rayleigh fading)
IEEE 802.15.3 High rate PAN	25 nsec minimum	WSSUS model with tap-delay line and Gaussian distributed taps with zero mean (Rayleigh fading)
Indoor at distances up to 30 meters (results here for 10 meters)	< 20 nsec for LOS < 70 nsec for NLOS for 2.4 GHz	Delay spreads for 2.4 GHz tends to be higher than 11.5 GHz. Delay spread increase with distance separation.
Indoor at ~ 1.5 GHz	Ave. rms delay spreads: Brick: 26-30 ns Concrete: 28-29 ns Office: 25 & 50 ns LOS factory: 96 ns OBS factory: 105 ns	Max rms delay spreads: Brick: < 70 ns Concrete: < 70 ns Office: 50 & 218 ns LOS factory: 300 ns OBS factory: 300 ns
UWB propagation indoor < 10 meters	Delay spreads on the order of 100 nsec observed	Suggests ray tracing not feasible for UWB. Number of dominant paths is much greater than 5 and < 50.
UWB propagation at 6, 10, and 17 m separation	--	Multipath energy varies by at most 5 dB (suggests fading is not of Rayleigh type)
900 MHz in office building environment. Paths were mostly OBS. Distances varied from 1-100 ft.	Mean RMS delays of 16, 40, 55 nsec for 3 different office buildings	Max. RMS delays of 48, 55, 146 nsec. Temporal variations followed closely to lognormal dist. rather than Rayleigh.
12,000 measurements in 2 office buildings in frequency band of 900-1300 MHz	Mean values between 20-30 nsec for 5-30 m antenna separations, values of 11-20 nsec for 10 m separation.	Results agreed with a value of 26 nsec and 25 nsec.
870 channel realizations (LOS and NLOS) in a condo setting using 2-8 GHz frequency band)	Mean RMS delay spread of 12.94 nsec, and mean excess delay of 13.59 nsec.	
300,00 channel realizations collected in 23 homes using 4.375-5.625 GHz frequency band)	Mean RMS delay spread of 8.2 nsec, and mean excess delay of 4.2 nsec.	
906 UWB channel soundings in an office using a 2 GHz center freq. With 1.5 GHz bandwidth pulse.	Mean RMS delay of 5.22 nsec	

4.2.1. RMS Delay Spread

Typical values for the multipath delay spread of indoor channels have been reported to be between 15 nsec in a residence to over 100 nsec in an office to a 150 nsec in a commercial building. Other measurements at 10 meter distances suggest RMS delay spreads of 19-47 nsec. In addition, the multipath delay spread has been found to increase as the separation distance between the receiving and transmitting antenna is increased. Table 4.1 shows some of the published RMS delay spread numbers that have been suggested for the indoor channel [23].

These results suggest that a fairly conservative RMS delay spread of 25 nsec would be a good initial starting point for PAN type applications with antenna separations of about 10 meters or less. Shorter RMS delay spreads could be considered for shorter ranges (5 meters or less). Meanwhile, another results found that average RMS delay spreads of around 17 nsec at these short ranges. As a result of this wide variation, the final multipath model should consider a range of RMS channel delay spreads.

4.2.2. Multipath Model Comparison

The following sections compare different multipath channel models with the Intel [23] measurements to see which model best approximates the measurement data characteristics. Since it is difficult to quantify the ‘best fit’ channel model to the measurements, three key channel characteristics: mean excess delay (τ_m), RMS delay spread (τ_{rms}), and mean number of multipath components with an amplitude within 10 dB of the peak return (NP_{10dB}) is focused. In some cases, non-line-of-sight (NLOS) and LOS channels characteristics were considered separately to determine how the model could be adjusted based upon different channel characteristics.

4.2.2.1. 802.11 Model

The 802.11 model is documented in an IEEE 802.11b standard group’s document, IEEE 802.11-00/282r2. It assumes that the channel impulse responses are output of finite impulse response (FIR) filters. The filter taps are independent complex Gaussian variables with average power profile that decays exponentially as shown in Figure 4.1. The taps are given by

$$h_k = N\left(0, \frac{1}{2}\sigma_k^2\right) + j \cdot N\left(0, \frac{1}{2}\sigma_k^2\right) \quad \text{for } k = 0, 1, \dots, k_{\max} \quad (4.8)$$

where

$$\begin{aligned} k_{\max} &= \lceil 10 \cdot \tau_{rms} / T_s \rceil \\ \beta &= e^{-T_s / \tau_{rms}} \\ \sigma_k^2 &= \sigma_o^2 \beta^k \\ \sigma_o^2 &= \frac{1 - \beta}{1 - \beta^{k_{\max} + 1}} \end{aligned} \quad (4.9)$$

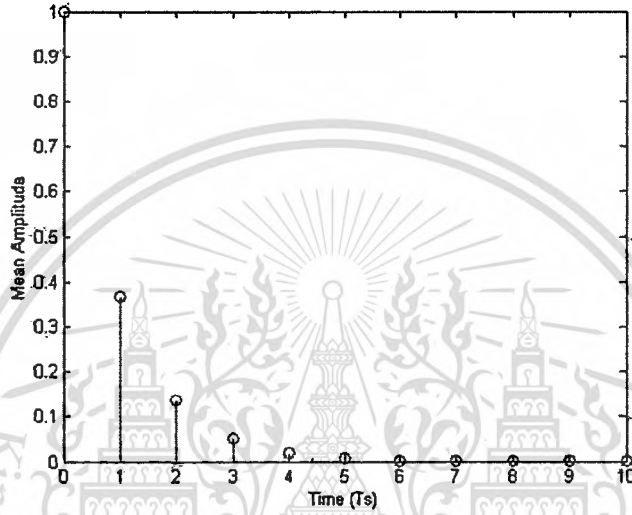


Figure 4. 1. Average power profile of Rayleigh model, taken from [23].

The sampling rate and sampling time at 6 GHz and 167 ps respectively is fixed as an example, as equivalent to the minimum resolution obtained from the channel measurements. Channel realization with RMS delay 5 ns, 10 ns, 15 ns, 20 ns, 25 ns are generated from the model. Then the number of paths that are within -10 dB from the maximum peak path for each channel realization is calculated. The empirical distributions of path numbers are plotted in the following figure. Intel's measurement [23] reports that RMS delays are 7-15 ns, and the mean number of paths is about 33 for a minimum multipath resolvability of 167 psec (corresponding to a 6 GHz measurement bandwidth).

Table 4. 2 Simulated and measured results for Rayleigh model

Simulated	τ_{rms} (ns)	5	10	12.94	15	20	20
	Mean NP _{10dB}	31	53	65	73	91	109
Measured	τ_{rms} (ns)			12.94			
	Mean NP _{10dB}			33			

4.2.2.2. Saleh-Valenzuela Model (S-V)

Unlike the 802.11 model, Saleh-Valenzuela model doesn't assume the arrival of paths on each sampling time interval. Instead, two Poisson models are employed in the modeling of the arrival time. The first Poisson model is for the first path of each path cluster and the second Poisson model is for the paths (or rays) within each cluster. Following the terminology in [24] is defined

T_l = the arrival time of the first path of the l -th cluster;

$\tau_{k,l}$ = the delay of the k -th path within the l -th cluster relative to the first path arrival time, T_l ;

Λ = cluster arrival rate;

λ = ray arrival rate, i.e., the arrival rate of path within each cluster.

By definition, then $\tau_{0,l} = T_l$ is settled. The distribution of cluster arrival time and the ray arrival time are given by

$$\begin{aligned} p(T_l | T_{l-1}) &= \Lambda \exp[-\Lambda(T_l - T_{l-1})], \quad l > 0 \\ p(\tau_{k,l} | \tau_{(k-1),l}) &= \lambda \exp[-\lambda(\tau_{k,l} - \tau_{(k-1),l})], \quad k > 0 \end{aligned} \quad (4.10)$$

The magnitude of the k -th path within the l -th cluster is denoted by β_{kl} . It is Rayleigh distributed with a mean given by

$$\overline{\beta_{kl}^2} = \overline{\beta^2(0,0)} \exp(-T_l / \Gamma) \exp(-\tau_{kl} / \lambda), \quad (4.11)$$

where $\overline{\beta^2(0,0)}$ is the average power of the first arrival of the first cluster.

Illustrations of channel impulse responses are shown below in Figure 4.2 and the double exponential decay model in Figure 4.3.

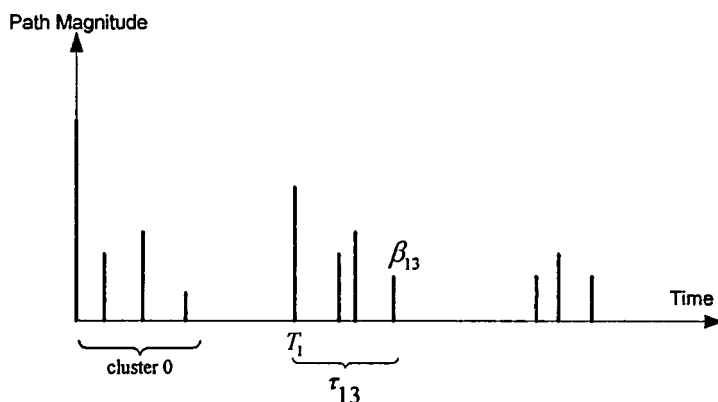


Figure 4. 2. An illustration of channel impulse response [23].

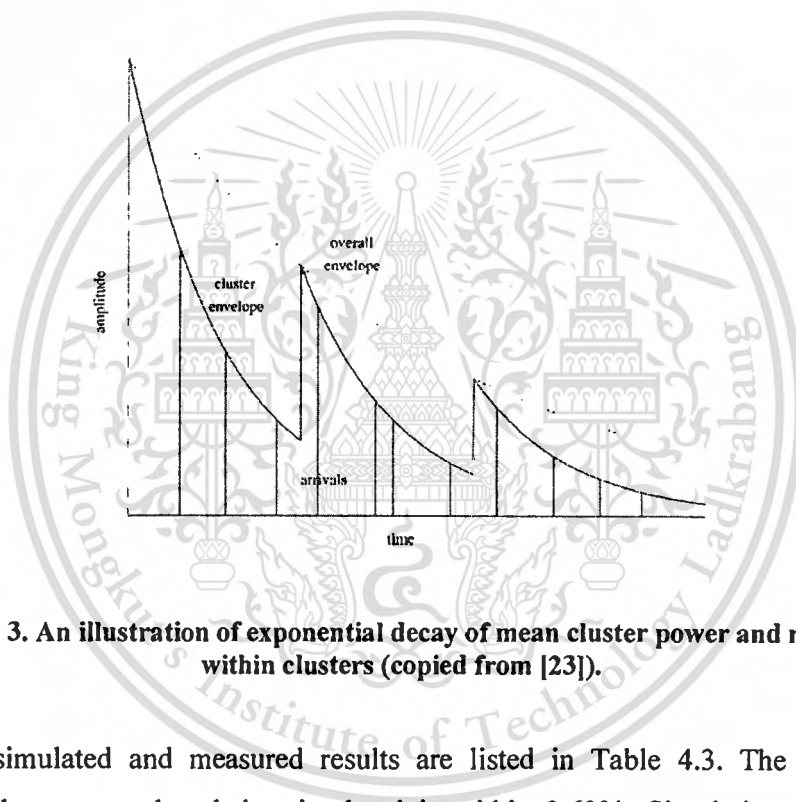


Figure 4. 3. An illustration of exponential decay of mean cluster power and ray power within clusters (copied from [23]).

The simulated and measured results are listed in Table 4.3. The difference between the measured and the simulated is within 3.63%. Simulation results are generated from Saleh-Valenzuela model with $\Gamma=15$ ns, $\gamma=6$ ns, $\Lambda=1/13$ ns, $\lambda=1/0.35$ ns.

Table 4. 3 Simulated and measured results for Saleh-Valenuela[23].

	Simulated	Measured
τ_m (ns)	13.53	13.59
τ_{rms} (ns)	13.41	12.94
Mean NP _{10dB}	34	33

4.2.2.3. Δ -K Model

The Δ -K model was proposed in [25]. A good fit to empirical indoor propagation data using the discrete time version of the model is reported in [26]. The discrete time model is described next. In the model, time axis is partitioned into bins with width Δ . Denote the probability of having a path in bin l as P_l . If there is a path in the previous bin, bin $l-1$, $P_l = K \lambda_l$; otherwise, $P_l = \lambda_l$ where λ_l is given by

$$\begin{aligned} \lambda_1 &= r_1 ; \\ \lambda_l &= \frac{r_l}{(K-1) \cdot r_{l-1} + 1}, \quad 2 \leq l; \end{aligned} \quad (4.12)$$

where r_l is the empirical bin occupancy rate for bin l . The path arrival process exhibits clustering for $K > 1$, and the path arrival tends to be more evenly spaced for $K < 1$. The impulse response of bin l is denoted as α_l , and the path amplitude $|\alpha_l|$ is lognormal distributed with an exponentially decaying multipath intensity profile (MIP). We add path polarity, p_l , to the model to account for pulse inversions caused by channel reflections, where we assume p_l is equiprobable ± 1 . The following equations describe these relationships.

$$\begin{aligned} \alpha_l &= p_l |\alpha_l| \\ 20 \log_{10}(|\alpha_l|) &\propto \text{Normal}(\mu_l, \sigma^2), \text{ or} \\ |\alpha_l| &= 10^{n/20} \text{ where } n \propto \text{Normal}(\mu_l, \sigma^2) \end{aligned} \quad (4.13)$$

$$E[|\alpha_l|^2] = \Omega_0 e^{-T_l/\Gamma}$$

where T_l is the excess delay of bin l and Ω_0 is the mean power of the first path of the first cluster. The μ_l is given by

$$\mu_l = \frac{10 \ln(\Omega_0) - 10T_l/\Gamma}{\ln(10)} - \frac{\sigma^2 \ln(10)}{20} \quad (4.14)$$

Table 4.4 shows the simulated and measured results for Δ -K model evaluation using Intel's results [23]. Simulation results are generated from Δ -K model with

$\Delta=0.125$ ns, $K=2.5$, $\Gamma=13$ ns, $r_i=0.6$, $\sigma=4.8$ dB, Table 4.5 shows the simulated and measured results for LOS UWB channels. Simulation results are generated from Δ -K model with $\Delta=0.125$ ns, $K=2.5$, $\Gamma=4.3$ ns, $r_i=0.15$, $\sigma=4.8$ dB, and Table 4.6 shows the simulated and measured results for NLOS UWB channels. Simulation results are generated from Δ -K model with $\Delta=0.125$ ns, $K=2.5$, $\Gamma=18$ ns, $r_i=0.45$, $\sigma=4.8$ dB.

In Table 4.4, mean excess delay, rms delay, and mean path number generated by the model fit the measurements including LOS and NLOS well. But from Table 4.5 and Table 4.6, the model can't fit both mean excess delay and rms delay at the same time for either LOS or NLOS channels due to the limitation that only one exponential slope is available.

Table 4. 4 Simulated and measured results for Δ -K model evaluation using Intel's results.

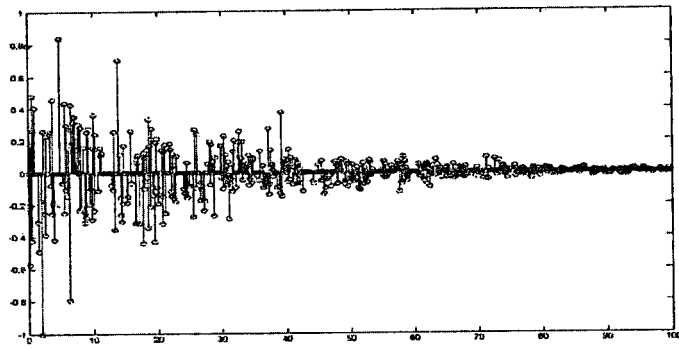
	Simulated	Measured
τ_m (ns)	13.13	13.59
τ_{rms} (ns)	12.82	12.94
Mean NP _{10dB}	34	33

Table 4. 5 Simulated and measured results for LOS UWB channels.

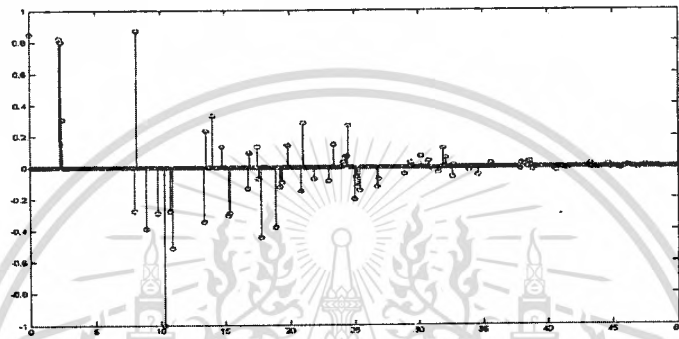
	Simulated	Measured
τ_m (ns)	4.11	4.01
τ_{rms} (ns)	4.21	8.88
Mean NP _{10dB}	7	7

Table 4. 6 Simulated and measured results for NLOS UWB channels.

	Simulated	Measured
τ_m (ns)	17.67	17.36
τ_{rms} (ns)	16.77	14.53
Mean NP _{10dB}	35	35



(a)



(b)



(c)

Figure 4. 4. One channel realization generated from Δ -K model

- (a) using the parameter in Table 4.4
- (b) using the parameter in Table 4.5
- (c) using the parameter in Table 4.6

4.2.3. Proposed Intel Channel Model

The clustering of path arrivals in UWB channels was reported, and also about the clustering effect of other wireless indoor channels [23]. The double-exponential decay model seems to provide enough degrees of freedom to easily match the channel measurements, and, as will be shown below, can be used to match the NLOS and LOS channel characteristics separately. The major difference between the double-exponential model and the single exponential model (embodied in the Δ -K model) is that the path amplitude in each subsequent cluster is not necessarily less than the one in the previous cluster in the double-exponential model.

Based on this clustering phenomenon observed in the measurements, it is proposed an UWB channel model derived from the Saleh-Valenuela model with one slight modification. Using a lognormal distribution is recommended rather than a Rayleigh distribution for the multipath gain magnitude, since the observations show that the lognormal distribution seems to better fit the measurement data. Therefore, the multipath model consists of the following, discrete time impulse response:

$$h(t) = \sum_{l=0}^L \sum_{k=0}^K \alpha_{k,l} \delta(t - T_l - \tau_{k,l}) \quad (4.15)$$

where $\alpha_{k,l}$ is the multipath gain coefficient, T_l is the delay of the l^{th} cluster, and $\tau_{k,l}$ is the delay of the k^{th} multipath component relative to the l^{th} cluster arrival time (T_l).

One consideration for the multipath model channel coefficients, $\alpha_{k,l}$, is whether they should be real or complex (with a magnitude and phase term). Some considerations are the following:

If real coefficients are adopted, then the channel coefficients could be defined as $\alpha_{k,l} = p_{k,l} \beta_{k,l}$, where $p_{k,l}$ is equally likely to take on the values of ± 1 , and $\beta_{k,l}$ is the lognormal fading term. The term $p_{k,l}$ is used to account for the random pulse inversion that can occur due to reflections, as observed in the measurements. Then, the real impulse response of the channel could be convolved with the real UWB transmitted waveform.

If complex coefficients are adopted, the complex, baseband equivalent channel model would need to be convolved with the complex, baseband representation of the

transmitted waveform. For a UWB pulsed system, the meaning of phase is a bit ambiguous since it is not necessarily carrier based. Since phase is directly related to delay for a given center frequency, it might be easier to account for phase for a specific waveform by converting it into a delay given a center frequency of the channel and/or waveform. Since we have not characterized the distribution of the phase term, we can only suggest that a uniformly distributed phase in $[0, 2\pi]$ could be a good model, based upon previous indoor channel models. In this case, the channel coefficients can be modeled as $\alpha_{k,l} = \beta_{k,l} e^{-j\phi_{k,l}}$, where $\phi_{k,l}$ is the random phase term uniformly distributed in $[0, 2\pi]$, and $\beta_{k,l}$ is the lognormal fading term.

Due to the simplicity of the real channel coefficients, and to avoid the ambiguity of phase for an UWB waveform, we suggest adopting $\alpha_{k,l} = p_{k,l} \beta_{k,l}$, where $p_{k,l}$ is equally likely to take on the values of ± 1 , and $\beta_{k,l}$ is the lognormal fading term.

Finally, the proposed model uses similar definitions as previously described for the S-V model, and are repeated here for completeness.

T_l = the arrival time of the first path of the l -th cluster;

$\tau_{k,l}$ = the delay of the k -th path within the l -th cluster relative to the first path arrival time, T_l ;

Λ = cluster arrival rate;

λ = ray arrival rate, i.e., the arrival rate of path within each cluster.

By definition, we have $\tau_{0,l} = T_l$. The distribution of cluster arrival time and the ray arrival time are given by

$$\begin{aligned} P(T_l | T_{l-1}) &= \Lambda \exp[-\Lambda(T_l - T_{l-1})], \quad l > 0 \\ P(\tau_{k,l} | \tau_{(k-1),l}) &= \lambda \exp[-\lambda(\tau_{k,l} - \tau_{(k-1),l})], \quad k > 0 \end{aligned} \quad (4.16)$$

The channel coefficients are defined as follows:

$$\begin{aligned} \alpha_{k,l} &= p_{k,l} \beta_{k,l} \\ 20 \log_{10}(\beta_{k,l}) &\propto \text{Normal}(\mu_{k,l}, \sigma^2) \\ \text{or } |\beta_{k,l}| &= 10^{n/20} \end{aligned} \quad (4.17)$$

where $n \propto \text{Normal}(\mu_l, \sigma^2)$

$$E[\beta_{k,l}^2] = \Omega_0 e^{-T_l/\Gamma} e^{-\tau_{k,l}/\gamma}$$

where T_l is the excess delay of bin l and Ω_0 is the mean power of the first path of the first cluster, and $p_{k,l}$ is equiprobable ± 1 . The μ_l is given by

$$\mu_l = \frac{10 \ln(\Omega_0) - 10T_l/\Gamma - 10\tau_{k,l}/\gamma - \sigma^2 \ln(10)}{\ln(10)} - \frac{\sigma^2 \ln(10)}{20} \quad (4.18)$$

Table 4.7 shows the simulated and measured results for Intel model evaluation using Intel's results. Simulation results are generated from Intel model with $\Gamma=13$ ns, $\gamma=6$ ns, $\Lambda=1/13$ ns, $\lambda=1/0.23$ ns, $\sigma=4.8$ dB. Meanwhile Table 4.8 shows the simulated and measured results for LOS UWB channels using Intel's model. Simulation results are generated from Intel model with $\Gamma=16$ ns, $\gamma=1.6$ ns, $\Lambda=1/60$ ns, $\lambda=1/0.5$ ns, $\sigma=4.8$ dB. And Table 4.9 shows the simulated and measured results for NLOS UWB channels using Intel's model. Simulation results are generated from Intel model with $\Gamma=16$ ns, $\gamma=8.5$ ns, $\Lambda=1/11$ ns, $\lambda=1/0.35$ ns, $\sigma=4.8$ dB.

The model in the following tables are proposed, including both LOS and NLOS channels with antenna separation 1-20 meters. In Table 4.7, mean excess delay, rms delay, and mean path number generated by the model fit the measurements including LOS and NLOS well. Also from Table 4.8 and Table 4.9, the model fit both mean excess delay and rms delay at the same time for either LOS or NLOS channels.

Table 4. 7 Simulated and measured results for Intel model evaluation using Intel's results.

	Simulated	Measured
τ_m (ns)	13.69	13.59
τ_{rms} (ns)	13.80	12.94
Mean NP _{10dB}	33	33

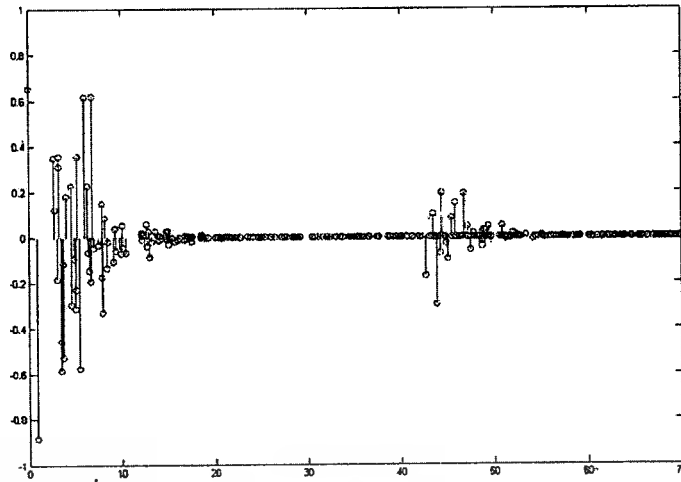


Figure 4. 5. One LOS channel realization generated using the parameter in Table 4.8.

Table 4. 8 Simulated and measured results for LOS UWB channels using Intel's model.

	Simulated	Measured
τ_m (ns)	4.70	4.01
τ_{rms} (ns)	8.81	8.88
Mean NP _{10dB}	7	7

Table 4. 9 Simulated and measured results for NLOS UWB channels using Intel's model.

	Simulated	Measured
τ_m (ns)	17.22	17.36
τ_{rms} (ns)	15.59	14.53
Mean NP _{10dB}	35	35

The above results show that the proposed model fits the measurements taken in the home environment for both LOS and NLOS. Of course, this only represents a small set of channel data, and other environments should also be considered. Therefore, we looked at how the model could be adapted to represent other possible channel conditions that might be appropriate for consideration. As shown above, there are 5 key parameters that define the model:

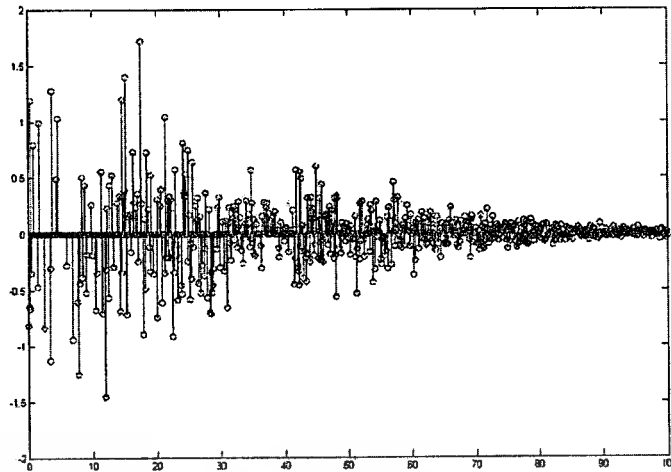


Figure 4. 6. One NLOS channel realization generated using the parameter in Table 4.9.

Table 4. 10 Example multipath channel characteristics and corresponding model parameters.

Channel Characteristics	NLOS*	NLOS#	NLOS#	LOS#	LOS*
Mean excess delay (nsec) (τ_m)	17	22	27	3	4
RMS delay (nsec) (τ_{rms})	15	20	25	5	9
NP_{10dB}	35	40	45	4	7
Model Parameters					
Λ (1/nsec)	1/11	1/14	1/15	1/22	1/60
λ (1/nsec)	1/0.35	1/0.33	1/0.32	1/0.94	1/0.5
Γ	16	22	30	7.6	16
γ	8.5	10	10	0.94	1.6
σ (dB)	4.8	4.8	4.8	4.8	4.8

* Based on Intel measurements.

Example of other possible channel characteristics to test.

Λ = cluster arrival rate;

λ = ray arrival rate, i.e., the arrival rate of path within each cluster;

Γ = cluster decay factor;

γ = ray decay factor;

σ = standard deviation of lognormal fading term (dB).

These model parameters were found using a brute force search to match different channel characteristics, considering mean excess delay (τ_m), RMS delay (τ_{rms}), and

number of significant paths that cross a 10 dB threshold (NP_{10dB}). The following table provides the results of this search.

Note that the above channel characteristics were just simply chosen as representing possible indoor environments that were not covered by the measurements of intel, but they seem to represent reasonable extensions.

A summary of the channel model parameters are given in the following table:

Table 4. 11 Summary of proposed channel model.

Parameter	Model
Path loss	Free space propagation using example link budget model to yield final link margin and proposed minimum sensitivity level.
Multipath model	Time domain multipath model, given by $h(t) = \sum_{l=0}^L \sum_{k=0}^K \alpha_{k,l} \delta(t - T_l - \tau_{k,l})$ with a double-exponential decay intensity profile based on the S-V model.
Channel Characteristics	Table 11 provides 5 different example channel characteristics that represent both LOS and NLOS channels. These characteristics are based on different mean excess delay, RMS delay spread, and mean number of paths.
Multipath Model Parameters	The proposed model requires defining the following parameters: Λ = cluster arrival rate; λ = ray arrival rate, i.e., the arrival rate of path within each cluster; Γ = cluster decay factor; γ = ray decay factor; σ = standard deviation of lognormal fading term (dB). Table 11 provides values for different channel characteristics.

Procedure to generate channel model for each multipath realization using parameters in Table 4.10 is:

1. Determine cluster arrival times (T_l) using the exponential inter-arrival time distribution (stop when $T_l > 10\Gamma$). Round T_l to the next higher multiple of 167 psec to yield a discrete model with minimum resolvable path spacings of 167 psec (corresponding to a 6 GHz waveform).
2. Determine ray arrival times ($\tau_{k,l}$) using the exponential inter-arrival time distribution (stop when $\tau_{k,l} > 10\gamma$). Round $\tau_{k,l}$ to the next higher multiple of 167 psec to yield a discrete model with minimum resolvable path spacings of 167 psec (corresponding to a 6 GHz waveform). Note that, it may be possible for a cluster arrivals and ray arrivals to occur at the same time. When this occurs, we recommend just summing up the arrivals at each time interval.
3. Determine $p_{k,l}$, with are equally likely +/- 1.
4. Set $\Omega_0 = 1$.
5. Determine $\mu_{k,l}$.
6. Determine $\beta_{k,l}$.
7. Determine $\alpha_{k,l} = p_{k,l} \beta_{k,l}$.

8. Compute the total energy of the channel ($E = \sum_{l=0}^L \sum_{k=0}^K |\alpha_{k,l}|^2$).
9. Normalize the total energy of the channel to unity:

$$h(t) = \frac{1}{\sqrt{E}} \sum_{l=0}^L \sum_{k=0}^K \alpha_{k,l} \delta(t - T_l - \tau_{k,l}).$$

Since different UWB waveforms may be proposed, which may have different bandwidths and, thus, different minimum multipath resolution, we suggest allowing the proposers to modify the above model as appropriate to match their analysis/simulation capabilities with their particular UWB waveform. For UWB bandwidths less than 6 GHz, the above model could still be used with minimum path spacings of 167 psec. Alternatively, to reduce the sampling rates for lower bandwidth waveforms, the channel realizations using the above procedure could be low-pass filtered to the desired bandwidth and re-sampled with a higher minimum path spacing. For UWB bandwidths greater than 6 GHz, the above model could still be used, but will not include paths that may arrive at a resolution less than 167 psec. In this case, the proposer could simply use the above model as an approximation (7.5 GHz is the maximum allowable FCC bandwidth, which is not significantly greater than the 6 GHz bandwidth used by measurements to derive the above model parameters), or reduce the minimum path spacing to the inverse of the UWB bandwidth and use the same parameters for the model as given above.

Chapter 5

UWB RECEIVER

Signals that have been generated, transmitted, and propagated, must be received in order to be understood. Receiving a UWB signal is a matter of "matching" the received energy to a predetermined template.

Some research has been conducted in UWB signal processing. In this chapter, the process of data recovery from the transmitted signal will be discussed. The main process, multiplication between the signal and template, is presented as circuit level. Interferences with noise may affect the signal performance. Together with channel model, AWGN noise effect will be discussed in this chapter.

From the mathematics point of view, the template signal is multiplied by the received signal and the resulting product or "correlation" is collected as signal energy in an integrator. Any mismatch between the signal shape and the template shape, or any misalignment in time between the two, results in a reduced efficiency in the collection of the energy. The signal is not as clear as it could possibly be because of the presence of noise.

5.1. Noise and Interference

Additive white Gaussian noise (AWGN), and interference from other systems occupying the spectrum, places a limit on the range and the capacity of a wireless system. Noise includes thermal noise caused by random vibrations of charges on a lossy conductor, interference, and meteorological noise.

Transmitters became "cleaner" and emitted "pure tone" signals, while receivers were tuned more narrowly to exclude as much noise as possible but still pass the information bandwidth. The signal-to-noise ratio S/N or SNR was greatly improved. The receiver-detector efficiency can be expressed as the output SNR divided by the input SNR. Signal-to-noise ratio and bit energy-to-noise density ratio are related in AWGN by taking into account the bit duration T_b , and the signal bandwidth B [27],

$$SNR = \frac{S}{N} = \frac{(E_b/T_b)}{N_0 B} \quad (5.1)$$

E_b/N_0 is the data-bit energy-to-noise density ratio. SNR and E_b/N_0 are equal when the signal bandwidth equals the inverse of the bit duration. In analog systems, B is often

taken to mean the net bandwidth of all the receiver filters, and is often wider than the signal bandwidth. A UWB communication with channel and AWGN is shown in Figure 5.1.

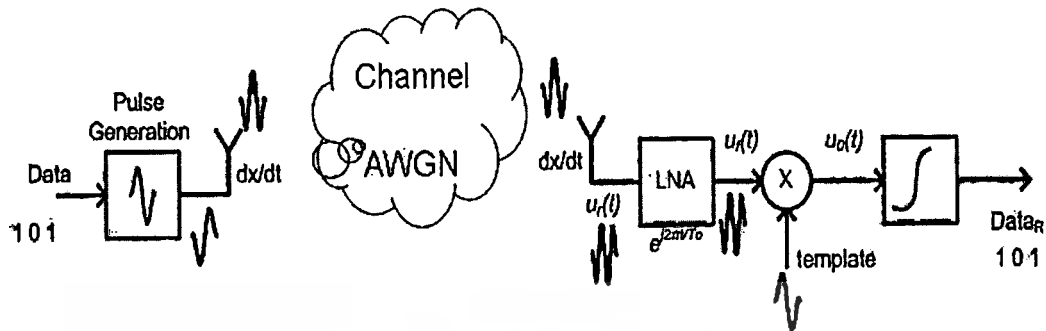


Figure 5. 1 UWB communication with channel and AWGN

The optimal receiver for signals transmitted over an AWGN channel is a correlation or a matched filter receiver, since it maximizes the SNR [5]. The receiver examined consists of a low-noise amplifier (LNA), a correlation circuit and a circuit to provide the template waveform for the correlation. After the received signal is amplified, it is correlated with the template waveform. The output of the correlation is processed by a bit decision circuit that decides which bits are carried by the received pulses. The baseband signal processing circuit is responsible for the bit decision.

To maximize the processing gain and SNR, the template waveform should be the same as that of the received signal. Such a signal is difficult to generate in practice, since the transmitted pulse is distorted by the antennas and the channel. The need to make the template waveform the same as that of the received signal also makes the receiving circuit more complex. One way to avoid this complexity is to approximate the template waveform by using the transmitted pulse, or to make very coarse approximations such as a rectangular pulse. It is also possible to ignore the template waveform altogether and rely on the pulse shaping caused by the finite bandwidth of the transmitting and receiving antennas [5].

In an ideal environment, the received pulse shape is the second derivative of the signal transmitted, since both antennas act as differentiators. The amplitude of the correlation result between the first and the third derivatives is 80% of the autocorrelation of the received waveform [5]. This means that using the transmitted waveform as the template reduces the performance of the correlator by less than 1 dB.

The correlation circuit consists of an integrator, and a multiplier that multiplies the received signal with the template waveform. The result of the multiplier is integrated over the bit duration to maximize the received signal power and to minimize the noise component. Having a train of pulses to integrate over, the correlated signal is raised from the noise and the possible signals of other users. From this it can be seen that the more pulses there are in a pulse train, the better SNR is attained, since more correlated energy is put into each symbol.

5.2. Multiplier for UWB

A multiplier circuit used for Ultra WideBand communications is proposed. A gigahertz V-I wideband four quadrant multiplier and the application for UWB pulse are described. The proposed multiplier circuit in this paper uses MOS cascade concepts [28,3] since it is very simple and applies fewer components.

As the UWB Communication Block Diagram is shown in Figure 5.1, it consists of a UWB pulse generation that convert data to UWB pulse in the transmitter side. In the receiver, the multiplier is followed by an integrator. The role of the multiplier is to convert the received RF signal to baseband for detection. Multiplier is further integrated to produce a robust signal level for A-to-D conversion.

The circuit multiplies two voltage inputs, but the output is in the current mode. It is more easily to sum and subtract the signal in the current mode than in the voltage mode. The output can be converted to the voltage using linear I-V converter described in the next section. Using this method, the output voltage has reference to ground. The proposed multiplier has -3dB bandwidth 13 GHz.

5.2.1. Multiplier Circuit Principle

5.2.1.1. Cascade MOS Operation

Consider transistors M1 in Figure 5.2, the simple MOS transistor model in saturation region and in triode region is expressed respectively as

$$I_D = \frac{K}{2}(V_{GS} - V_{TH})^2, \quad (5.2)$$

for $V_{GS} > V_{TH}, V_{DS} \geq V_{GS} - V_{TH}$

$$I_D = K(V_{GS} - V_{TH} - V_{DS}/2)V_{DS},$$

for $V_{GS} > V_{TH}, V_{DS} < V_{GS} - V_{TH}$ (5.3)

where $K = \frac{1}{2}\mu_0 C_{ox}(W/L)$ is the transconductance parameter of transistor, μ_0 is the electron mobility, C_{ox} is the gate oxide capacitance per unit area, W/L is the transistor aspect ratio, V_{GS} is the gate-to-source voltage, V_{DS} is the drain-to-source voltage and V_{TH} is threshold voltage of the MOS transistor.

Figure 5.3 shows the cascade MOS operation. X and Y are proper dc bias voltage. If M2 works in triode region and M1 works in saturation region, then M1 behaves as a source follower and V_{DS} of M2 is controlled by x through the source follower M1. According to the large signal model in the triode region of M2 as in (5.3), I_D can be expressed as

$$I_D = K\left(Y + y - V_{TH} - \frac{x}{2}\right)x \quad (5.4)$$

The output currents are obtained from (5.4) as follows

$$I_1 = K\left(Y + y - V_{TH} - \frac{x}{2}\right)x \quad (5.5)$$

$$I_3 = K\left(Y - y - V_{TH} - \frac{x}{2}\right)x$$

The difference of output current yields a multiplication as

$$I_1 - I_3 = 2K.x.y \quad (5.6)$$

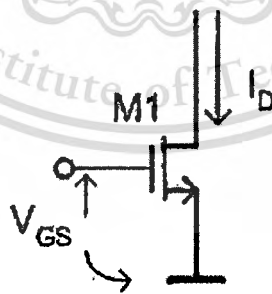


Figure 5. 2 MOS operation

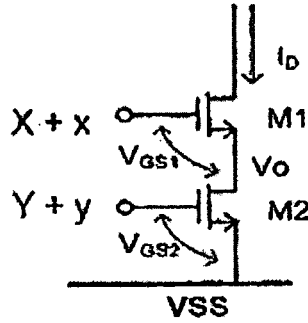


Figure 5. 3 Cascade MOS Operation

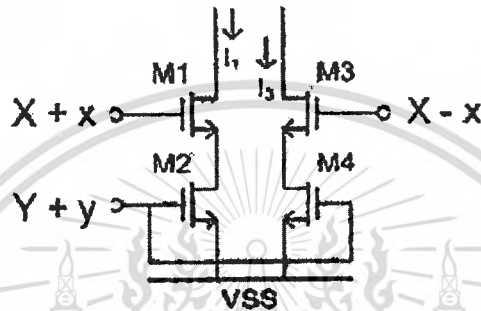


Figure 5. 4 Two-quadrant Multiplier

5.2.1.2. Four Quadrant V-I Multiplier

A Fully differential configuration improves the linearity and power supply rejection ratio. The configuration using four MOS is shown in Figure 5.5. Based on (5.4), the difference between I_A and I_B can be considered as input multiplication, as follows

$$I_A - I_B = (I_1 - I_3) + (I_5 - I_7) \quad (5.7)$$

$$I_A - I_B = 2K.x.y + 2K.x.y \quad (5.8)$$

$$I_A - I_B = 4K.x.y \quad (5.9)$$

It is shown in (5.9) that the current subtraction $I_A - I_B$ is the simple multiplication of the input voltages x and y .

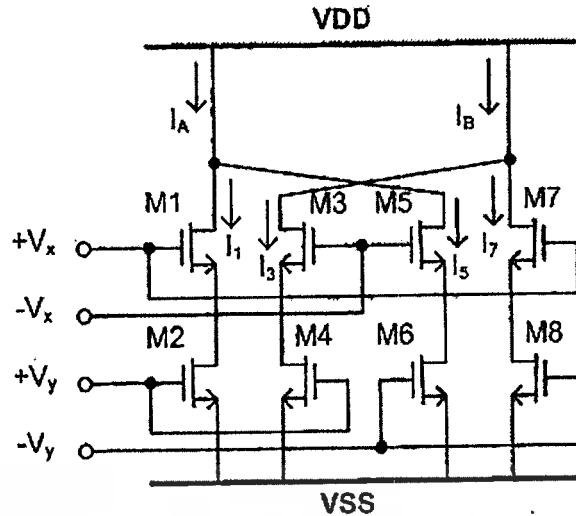


Figure 5. 5 Four-quadrants Multiplier

5.2.2. The Proposed Multiplier Circuits

The principle of operation of the proposed multiplier is based on Figure 5.6 that has equation in (5.9). This is a voltage to current (V-I) multiplier. The proposed analog multiplier circuit is shown in Figure 5.6.

To get and subtract the currents I_A and I_B , three current mirrors are used. The MOS M9 M13 pair in Figure 5.6 is the current mirror for I_A , while the M10 M11 pair is for I_B . The drain current of MOS formed in (5.2), or $I_B = f(V_{GS_{M10}})$. Based on (5.2), the inverse function $V_{GS_{M10}} = f^{-1}(I_B)$ can be written as

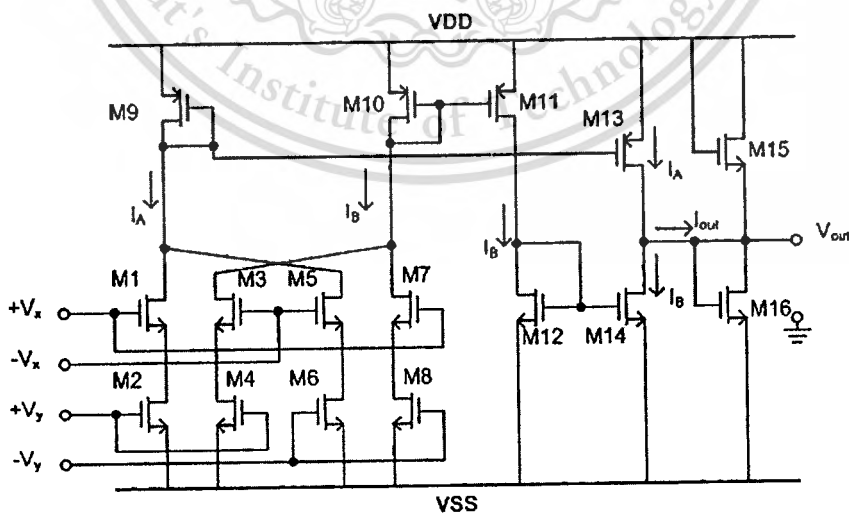


Figure 5. 6 The Proposed Multiplier Circuit

$$V_{GS_{M10}} = V_{TH} + \sqrt{\frac{I_B}{K}} \quad (5.10)$$

The same equation is implemented also for M11. Since M10 and M11 are identical, and $V_{GS_{M10}} = V_{GS_{M11}}$, then

$$\begin{aligned} I_{10} &= I_{11} = I_B \\ I_9 &= I_{13} = I_A \end{aligned} \quad (5.11)$$

The M12 M14 pair is given to subtract between I_A and I_B . I-V conversion can be reached using M15 and M16 in Figure 5.6. Based on (5.2), the drain currents respectively are

$$\begin{aligned} I_{15} &= K(V_{DD} - V_{out} - V_{15})^2 \\ I_{16} &= K(V_{out} - V_{SS} - V_{16})^2 \end{aligned}$$

Since $I_{Out} = I_{16} - I_{15}$, $V_{SS} = -V_{DD}$ and $V_{TH1} = V_{TH2} = V_{TH}$, the output voltage can be written as

$$V_{Out} = \frac{I_{out}}{4K(V_{DD} - V_{TH})} \quad (5.12)$$

Substitution (5.8) into (5.12) concludes that the output voltage of the proposed multiplier circuit shown in Fig. 5 is the multiplication of the both input voltages, and can be formed as

$$V_{out} = \frac{V_x V_y}{(V_{DD} - V_{TH})} \quad (5.13)$$

5.2.3. Performance analysis

The performances of the proposed analog multiplier circuit are simulated using HSPICE with level 49 model of 0.18 μ m MOS parameter. The voltage supply are $V_{DD} = -V_{SS} = 1V$.

The complete circuit of the current multiplier is viewed in Figure 5.6, and the simulation use 0.18 μ m CMOS with $L/W = 0.18/0.18 \mu$ m. The simulation result of the DC characteristic shown in Figure 5.7. Input of V_x and V_y are from -250mV to +250 mV. As shown in Figure 5.6, by the voltage supply of $V_{DD} = -V_{SS} = 1V$, the result is linear for the range of the voltages input sweep of -250 mV to +250 mV. Figure 5.8 shows the frequency response of the multiplier in Fig 5.6. The graph is about V_{out}/V_x in dB. The graphics shows that -3 dB response of the multiplier is very high, at 13

GHz. It is convenient for the UWB signal communications that need 10.5 GHz maximum. Table 5.1 shows the specifications of the multiplier circuit and the result.

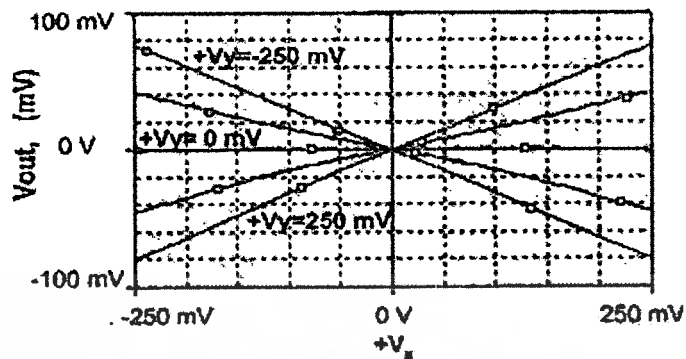


Figure 5. 7 DC Characteristics

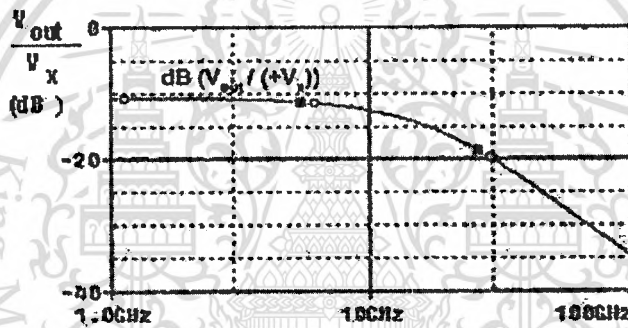


Figure 5. 8 Frequency Response

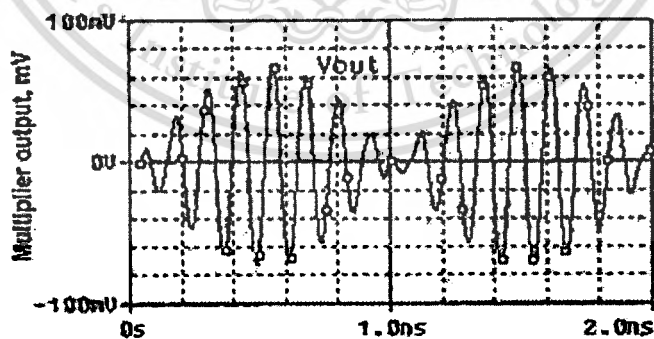


Figure 5. 9 Transient simulation for 2 sine waves

Table 5. 1 Multiplier circuit specifications

dB in 1 GHz or less	-10.7 dB
Freq in -3 dB (-13.7 dB)	13.0 GHz
Power Supply	± 1 Volt
Input Amplitude (V_x)	± 0.25 V
Input V_y	± 0.25 V

Table 5. 2 Input signal of Figure 5.9

Supply voltage	± 1 Volt
Input Amplitude V_x	± 0.25 V
Frequency V_x	500 MHz
Input Amplitude V_y	± 0.25 V
Frequency V_y	8 GHz

Figure 5.9 shows the transient analysis of the multiplier in Figure 5.6. The amplitude of input voltages V_x and V_y are 0.25 V. The frequency of V_x and V_y are 500 MHz and 8 GHz respectively. Table 5.2 shows the specifications of the signals.

5.2.4. The Application for UWB Pulse

Figure 5.10 shows about the UWB pulse generation circuit and its pulse, as described in chapter 2. The circuit has advantages in simplicity that using few components. All circuits are simulated using HSPICE level 49 of 0.18 μ m CMOS parameter from mosis [18]. The UWB pulse generation circuit specifications is shown as Table 2.3.

The input is a step signal or pulse that the width is in such a way that the Gaussian pulse can be performed. L/W in CMOS inverters (NOT) and NAND used in this research are respectively 0.36/0.36 μ m and 0.18/0.27 μ m.

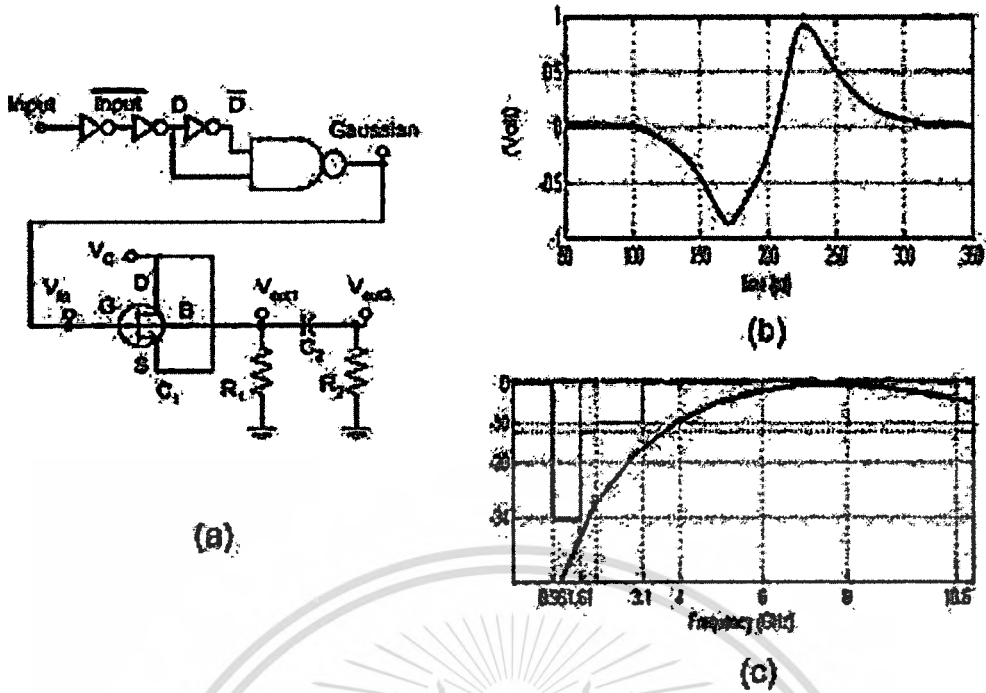


Figure 5.10 The UWB pulse generation circuit and its pulse

Figure 5.10 (b) shows the time diagram of Gaussian monocycle pulse at the V_{out1} node. The monocycle has 200 ps width (100 ps to 300 ps), and peak to peak value 874 mV and 906 mV.

Figure 5.10 (c) shows the normalized Power Spectral Density (PSD) of the derivative of the monocycle pulse from the circuit. If a monocycle pulse is transmitted, due to the derivative characteristics of the antenna, the output of the transmitter antenna can be modeled by the first derivative of the pulse [19].

As in chapter 2, when the time diagram is shown in Figure 5.10 (b), called $x(t)$, the derivative can be achieved by the basics of differential calculus

$$x^{(1)}(t) = \lim_{dt \rightarrow 0} \frac{x(t + dt) - x(t)}{dt} \quad (5.14)$$

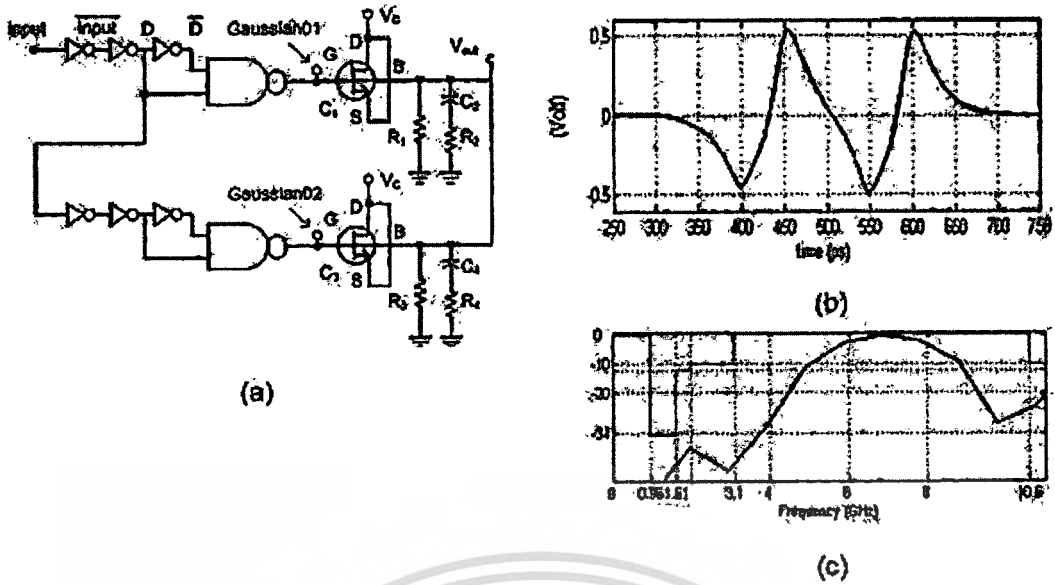


Figure 5.11 The improvement of the proposed circuit and its pulse

PSD of the deterministic power signal, $w(t)$, is

$$P(f) = \lim_{T \rightarrow \infty} \left(\frac{|X(f)|^2}{T} \right) \quad (5.15)$$

where T is the pulse spacing interval. $X(f)$ is the Fourier transform of the pulse, i.e. $x(t)$. $P(f)$ has units of watts per hertz. When $X(f)$ is attained, the peak emission frequency, i.e. f_M , can be found as the frequency at which the maximum value of $|X(f)|$. The normalized PSD can be defined as

$$|P(f)| = \frac{|X(f)|^2}{|X(f_M)|^2} \quad (5.16)$$

The normalized PSD in Figure 5.10 (c) applies (5.16) in which $X(f)$ is the Fourier Transform of the differential of the pulse in Figure 15. The differentiation uses the equation in (5.14). The normalized PSD is used due to comply the FCC spectral mask of the pulse that is transmitted by antenna [6,19,29]. Figure 16 shows that PSD complies the spectral mask, unless it is over the tail of the frequency (10.6 GHz).

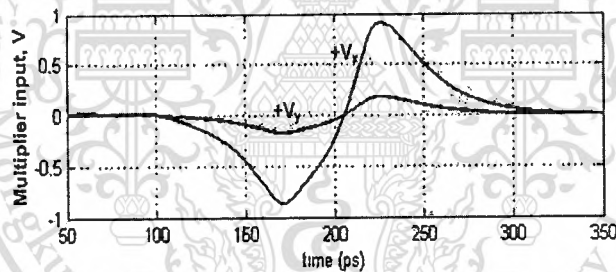
Figure 5.11 shows the improvement of the Gaussian monocyte pulse circuit generation. The second monocyte pulse is generated after being delayed by two NOT's. Then both monocytes are connected to generate UWB pulse 4th derivative of the Gaussian pulse shape. The equation of the 4th derivative of the Gaussian pulse can be written as follows;

$$x^{(4)}(t) = \frac{dx^4(t)}{dt^4} = [A_3u^3 - A_4u] \cdot e^{-2u^2} \quad (5.17)$$

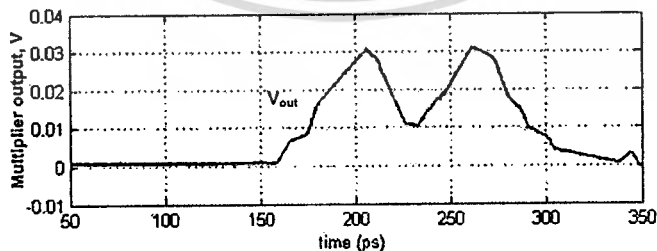
where $u = \pi t/T_c$ in (5.4). The values A_3 and A_4 are the amplitudes. Figure 18 shows the time diagram of Gaussian monocycle pulse at the V_{out} node. The figure shows that the graphic has four peaks of signal which conducts as the fourth differential function of Gaussian pulse in (5.17).

Figure 5.11 (c) shows the normalized Power Spectral Density (PSD) of the UWB pulse derivative from the circuit in Figure 5.11 (b), using (22). As shown in Figure 5.11(c) the normalized PSD complies the FCC spectral mask.

The multiplier is simulated under a 0.18- μm CMOS process. Figure 5.12 shows about the transient analysis for Ultra wideband impulse radio done by two monocycle pulses with same width of 0.2 ns with different amplitudes as shown in Figure 5.12(a). The two pulses of 0.2ns are generated by using a monocycle pulse generation circuit in Figure 5.10. Figure 5.12(b) shows that the result is relatively only in positive voltage, means that the correct output is obtained at the output of the multiplier.



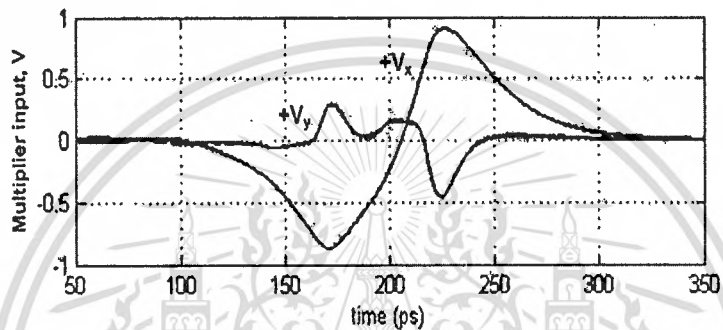
(a) Two inputs of the monocycle pulse



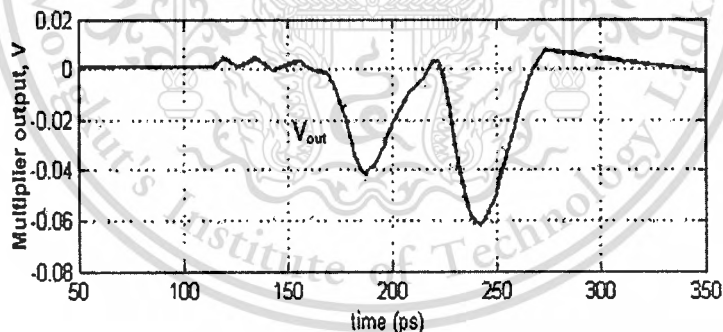
(b) Output Result

Figure 5. 12 Two monocycle pulses multiplication

Figure 5.13 shows about the transient analysis for Ultra wideband impulse radio done by the monocycle pulse and its second derivative inputs, as shown in Figure 5.13(a). This is to consider that in the real correlator that the received signal is weaker than the template signal, and the received signal has been differentiated in each antenna (see Figure 1). In ideal environment, the received pulse shape is the second derivative of the transmitted since both antennas act as differentiators. The amplitude of correlation between the first derivative of UWB Gaussian pulse and its second derivative is 80% of the autocorrelation of the received waveform [5]. Figure 5.13(b) shows that the correct output is obtained at the output of the correlation.

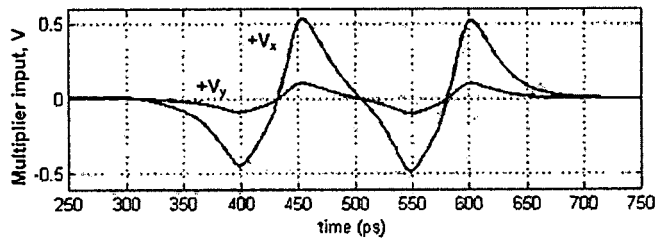


(a) The monocycle pulse and its second derivative inputs

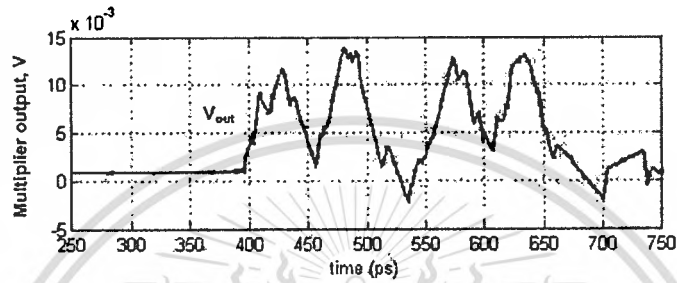


(b) Output Result

Figure 5. 13 The monocycle and its second derivative pulses multiplication

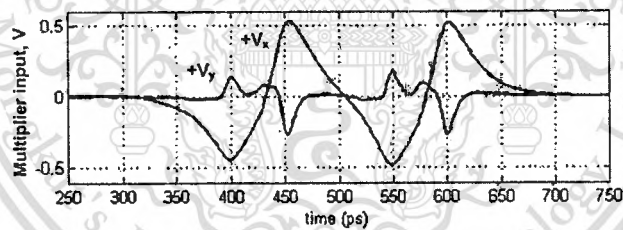


(a) Two inputs of the triplet UWB pulse

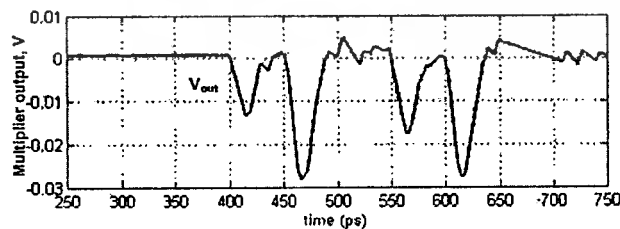


(b) Output Result

Figure 5. 14 Two UWB triplet pulses multiplication



(a) the UWB triplet pulse and its second derivative inputs



(b) Output Result

Figure 5. 15 The UWB triplet and its second derivative pulses multiplication

The transient analysis of the improved Ultra wideband impulse radio is shown in Figure 5.14(a). Circuit in Figure 17 generates the UWB triplet pulses of 0.4ns. As the result in Figure 5.12(b), the result is relatively only in positive voltage as shown in Figure 5.14(b), means that the correct output is obtained at the output of the multiplier.

Figure 5.15 shows about the transient analysis for Ultra wideband impulse radio done by the triplet pulse and its second derivative inputs, as shown in Figure 5.15(a). Figure 5.15(b) shows that the correct output is obtained at the output of the correlation.

5.2.5. Discussion

[30,31,32] are voltage mode multipliers that relatively have complex circuits. [33,34] are current mode. [30] is relatively complex, and [34] is relatively simple, but both have the frequency response relatively low, in MHz. [35] proposed an analog multiplier in voltage mode for UWB. However, the circuit is still more complex than this proposed circuit. The voltage to current conversion of this proposed multiplier will subtract the signals in the current mode that is easier to be implemented. The current mode output increases the operation of bandwidth. Without adding inductors as in [35], this circuit has 13 GHz Bandwidth. In addition, by converting back to the voltage mode, the output signal has reference to ground.

The UWB pulse generation has advantage also in simplicity and low cost power that are main focus in the UWB point of view. It applies 3 (three) NOTs, 1 (one) NAND, 2 (two) resistors, 1 (one) capacitor, and 1 (one) MOS as capacitor. Totally it implements 11 MOS. As comparison, Azakkour [11] based on Choi [8] has proposed a gated pulse generator for UWB. Since it used VCO and on-off switch, it was more complicated than our design. A wavelets generation circuit for UWB proposed by Gerrits [8], combined the output signals of four bipolar differential pairs to generate the second derivative of the Gaussian function as output signal. The circuit implemented 8 (eight) MOS's but it is excluding 4 (four) current sources applied in the circuit.

5.3. IR-UWB Interference over Modified S-V Channel Model

As in chapter 2, Figure 5.1 shows a block diagram of the transmitter-receiver communication. Transmitter sends Data bit packet by packet, and Receiver read the

packet. Transmitter converts the bits in packet to be UWB pulses, and then send to the antenna to be transmitted. In Figure 5.1, $u_r(t)$ is the received signal at time instance t . The signal then through LNA (Low Noise Amplifier) and becomes $u_f(t)$. Then it is demodulated using template pulse.

The UWB pulse is the generated monocycle or triplet pulse described previously. The classic binary pulse amplitude modulation (BPAM) is implemented in Pulse Generation block in Figure 5.1. It can be presented using e.g. two antipodal Gaussian pulses. The transmitted binary baseband pulse amplitude modulated information signal (t) can be presented as [5]

$$x(t) = d_j \cdot w_r(t) \quad (5.18)$$

where $w_r(t)$ represents the UWB pulse waveform, j represents the bit transmitted that $j=1$ then $d_j = 1$ and $j= '0'$ then $d_j=-1$.

A channel happens between transceiver and receiver. In this paper, an UWB channel model derived from the Saleh-Valenuela model with one slight modification is proposed. This is the proposed model that fits the measurements taken in the home environment for both LOS and NLOS [30]. There are 5 key parameters that define the model: Λ = cluster arrival rate; λ = ray arrival rate, i.e., the arrival rate of path within each cluster; Γ = cluster decay factor; γ = ray decay factor; and σ = standard deviation of lognormal fading term (dB).

Table 5.3 Channel model parameters.

Model Parameters	LOS	NLOS
Λ (1/nsec)	1/60	1/11
λ (1/nsec)	1/0.5	1/0.35
Γ (nsec)	16	16
γ (nsec)	1.6	8.5
σ (dB)	4.8	4.8

This research uses one of channel realization generated from S-V model using the parameters as in Table 5.3 from [30] the BER analysis. The channel is shown in Figure 5.16.

In an ideal environment, the received pulse shape is the second derivative of the signal transmitted due to differentiator effect in transmitter and receiver antennas. However, the amplitude of correlation result between the first and the third derivatives of the Gaussian pulse is 80% of the autocorrelation of the received

waveform [5]. This means that using the transmitted waveform as the template reduces the performance of the correlator by less than 1 dB. Therefore, the receiver still can use the same template waveform as the transmitter has to demodulate the signals.

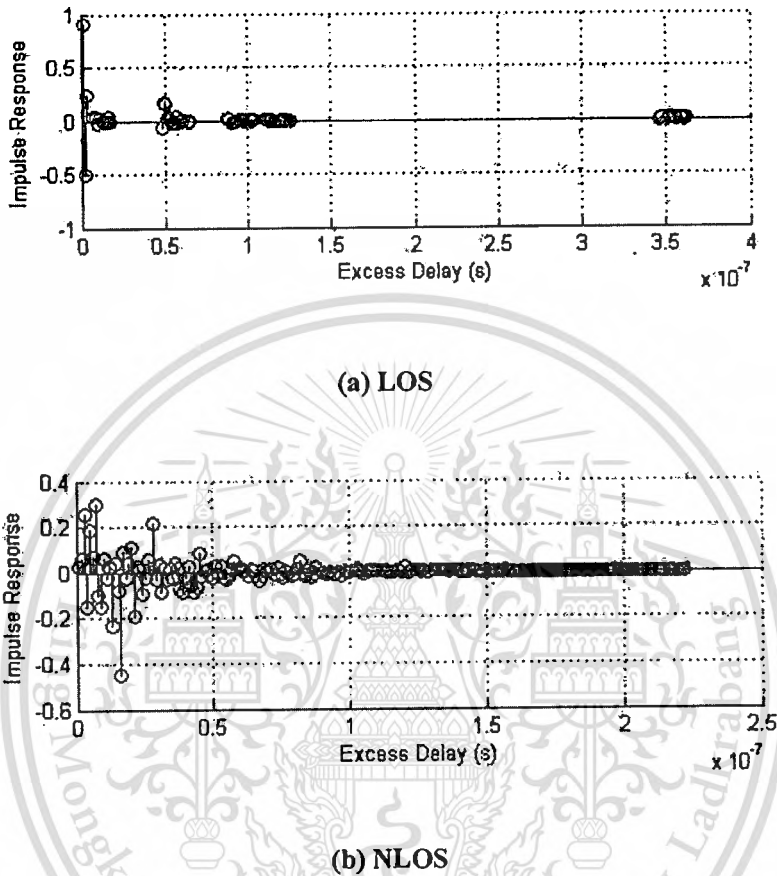


Figure 5.16 The generated channel model

5.4. BER Analysis Results

The implementation is based on Block Diagram in Figure 5.1. The transceiver converts bits into UWB pulses, then the UWB pulses are reconverted the pulse back into bits by receiver. Both monocycle and triplet is implemented. Also the channel model, both LOS and NLOS model is implemented. There are many channel model can be generated using model parameters in Table 5.3 to implement (7) until (10). We used one of them as shown in Figure 5.16. Transceiver sends Data bit packet by packet. BPAM is implemented for modulation.

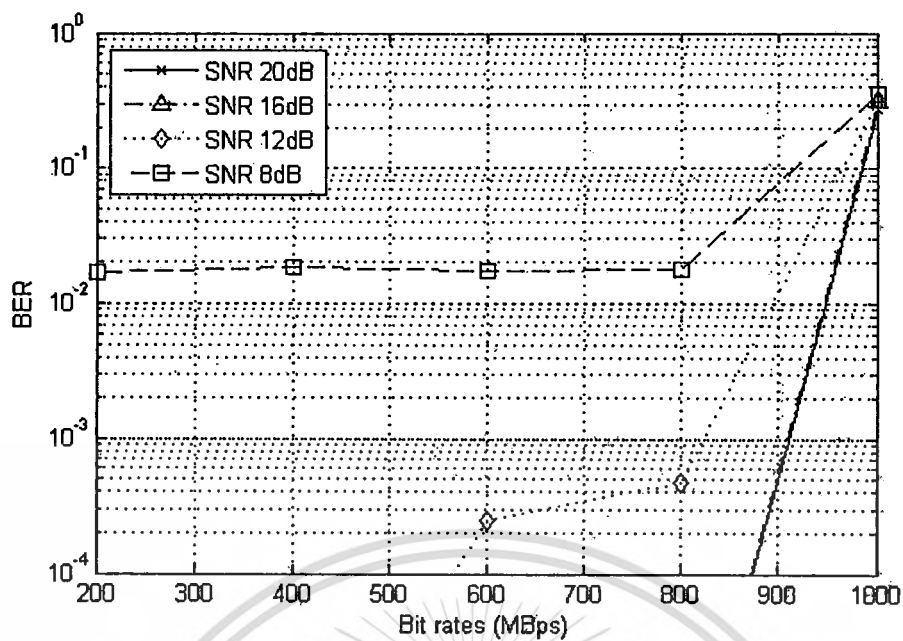
In our experiments, there are around 10^4 bits sent from the transceiver to receiver, and later being analyzed. The bits are sent periodically, so that give a bit rate value in Mbps. The various bit rates and its BER can be seen in Figure 5.17. The result shows that interference of multipath gives high effect to make an error. The LOS channel model in Figure 5.17 (a) has the last significant paths that cross a 10 dB threshold (NP10dB) at 0.5×10^{-7} sec and it has only 5 multipaths. It gives low BER until hundreds Mbps. Meanwhile, the NLOS channel has many multipaths that influence the pulses, so that it can not be sent in high bit rates. The NLOS channel model in Figure 10 (b) has the last significant paths that cross a 10 dB threshold (NP10dB) at around 1.0×10^{-7} sec and it has around 33 multipaths, so that it is much thicker. The bit rates drops drastically in the NLOS channel model.

Table 5. 4 Estimate of highest bit rates (HBR)

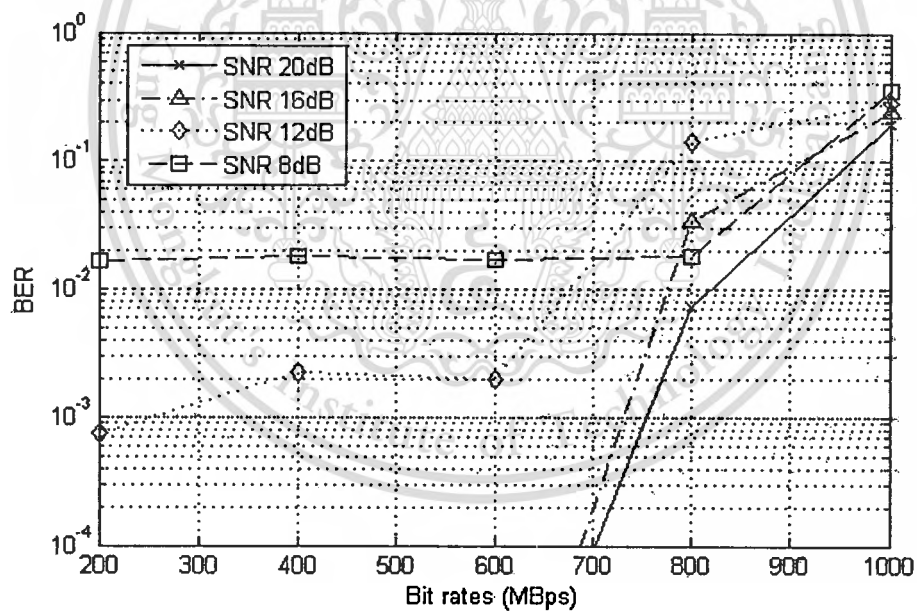
Model	Bit rates (Mbps)		
	SNR 20 dB	SNR 16 dB	SNR 12 dB
LOS monocycle	800	800	800
LOS triplet	600	600	200
NLOS monocycle	30	-	-
NLOS triplet	20	-	-

Figure 5.17 shows the result of the BER of the monocycle and triplet pulses through the LOS and NLOS channel models. Figure 5.17 shows that the influence of inter multipaths occurs in higher bit rates. In the LOS channel, it gives high error after 800 Mbps. For bit rate below than 800 Mbps, BER is relatively low (in 10^{-4} or lower) in high SNR of AWGN. In the NLOS channel, high error occurs after 30 Mbps. For bit rate below than 30 Mbps, BER is relatively low (in 10^{-4} or lower) in high SNR. Note that in order to draw the line in Figure 5.17, the value of $\log(10^{-6})$ is given instead of BER = 0, since log zero is infinity.

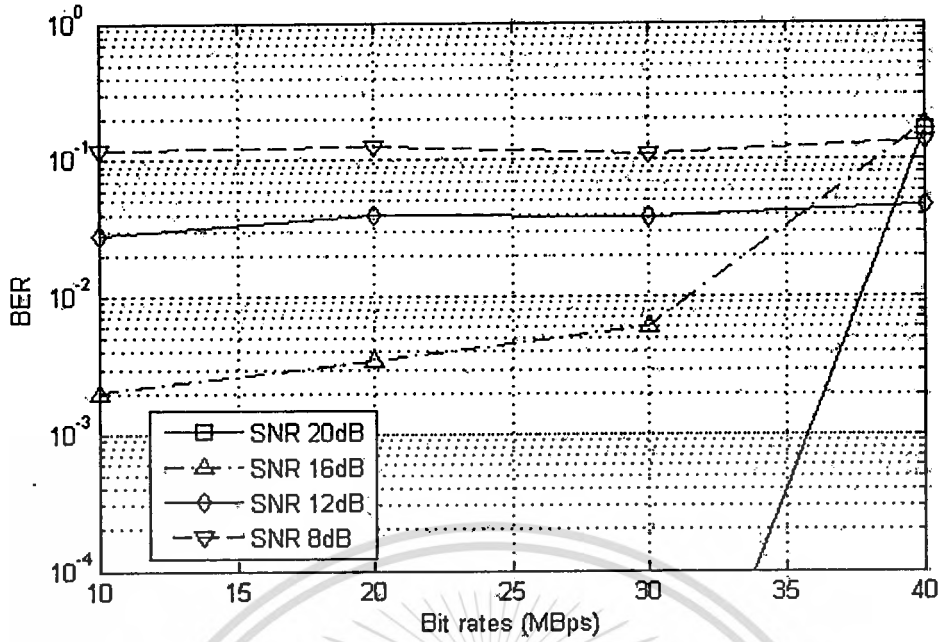
Figure 5.17 (a) shows data sent using monocycle pulse over the LOS channel model. The result shows that SNR 8 dB AWGN gives high BER. SNR 12 dB gives no error (or error lower than 10^{-4}) until 400 Mbps and has error in 10^{-4} level until 800 Mbps. BER also increases drastically after 800 Mbps. SNR 16 and 20 dB has no error (or error lower than 10^{-4}) until 800 Mbps, but it has much higher BER afterwards.



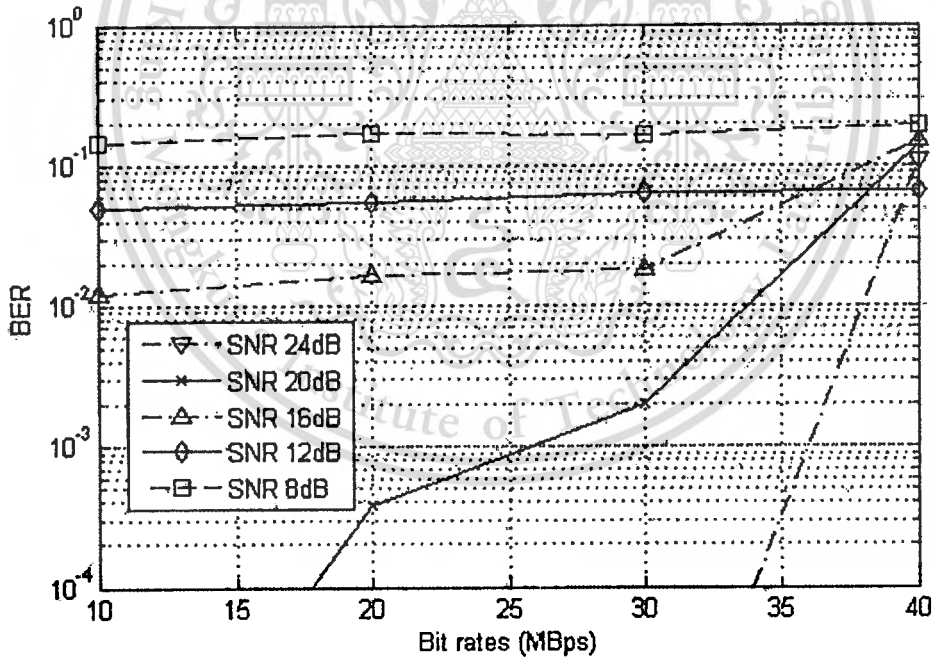
(a) UWB monocycle pulse over LOS channel



(b) UWB triplet pulse over LOS channel



(c) UWB monocyte pulse over NLOS channel



(d) UWB triplet pulse over NLOS channel

Figure 5. 17 BER of the UWB pulses through the LOS and NLOS channel models

Figure 5.17 (b) shows data sent using triplet pulse over the LOS channel model. SNR 8 dB AWGN gives high BER. SNR 12 dB gives small error (in 10^{-4} level) within 200 Mbps and error in 10^{-3} level until 600 Mbps. BER also increases drastically after 600 Mbps. SNR 16 and 20 dB has no error (below 10^{-4}) until 600 Mbps, and the value of BER increases drastically afterwards.

Different from the LOS channel that has much higher bit rates, the NLOS channel gives lower bit rates for the communication. In Figure 5.17 (c), data are sent using monocycle pulse over NLOS channel model. It has high BER until SNR 12 dB. SNR 16 dB gives BER in 10^{-3} level occurs for bit rates below 30 Mbps and increases drastically after 30 Mbps. SNR 20 dB has no error (or error lower than 10^{-4}) until 30 Mbps, but it also has higher BER afterwards.

In Figure 5.17 (d), data are sent using triplet pulse over the NLOS channel model. It has high BER until SNR equals to 12 dB. SNR 16 dB gives BER in 10^{-2} level for 30 Mbps and below and increases drastically afterwards. SNR 20 dB has no error (lower than 10^{-4}) for 10 Mbps, 10^{-4} level BER for 20 Mbps, and 10^{-3} level for 30 Mbps. It has higher BER for above 30 Mbps. Finally, SNR 24 dB has no error (lower than 10^{-4}) until 30 Mbps and has higher BER afterwards.

All results in Figure 5.17 show that if the SNR of AWGN increases, then BER decreases. In this simulation, SNR 20 – 24 dB AWGN has good performances of BER value. Comparing monocycle and triplet pulse, the result shows that for the same channel, the monocycle has more robust of AWGN. Figure 5.17 (a) and (b) shows that the monocycle has error in 10^{-4} level until 800 Mbps, while the triplet begins to have more error since 600 Mbps. In Figure 5.17 (c) monocycle has no error until 30 Mbps at SNR 20 dB, while SNR 24 dB has no error until 30 Mbps for triplet in Figure 5.17 (d).

From the results, it can be said that UWB pulse communication is appropriate in the LOS channel, i.e., has high bit rates (hundreds Mbps). Nevertheless, this communication can be used until several Mbps in NLOS channel model.

Table 5.4 shows estimation of highest bit rates without error (or error in 10^{-4} level is tolerable). If the less BER is desired, then lower bit rate can be implemented. However, in high SNR environment, the high bit rate can still be implemented. It shows that monocycle pulse over LOS channel gives the best bit rates. By looking at the UWB reference standard and compare to the others as shown in Table 5.5[1], it seems that this communication model is preferable for the LOS channel.

Table 5.5 Comparison of UWB bit rate with other standards.

Speed (Mbps)	Standard
480	UWB, USB 2.0
200	UWB (4 m minimum)
110	UWB (10 m minimum)
90	Fast Ethernet
54	802.11a
20	802.11g
11	802.11b
10	Ethernet
1	Bluetooth

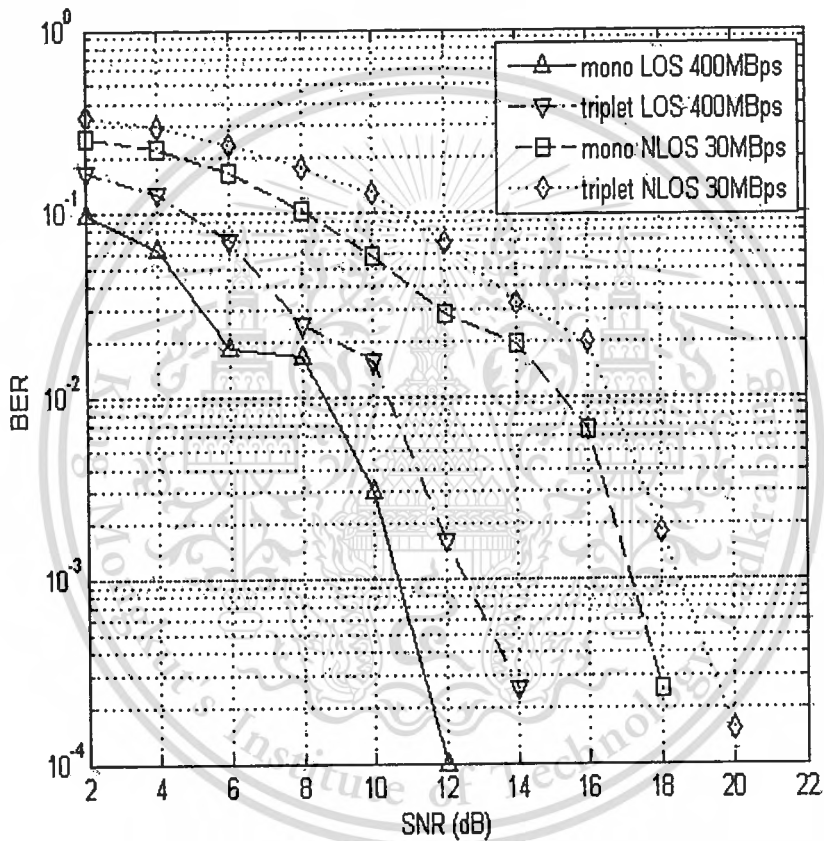


Figure 5. 18 BER performances over AWGN channels

Based on Figure 5.17 (a)-(d), some samples of bit rate are chosen to take a closer look at each pulse over LOS and NLOS channels. For the LOS channel based on Table 5.5, 400 Mbps is chosen for the monocycle and triplet pulse. However, since the maximum bit rates for NLOS channel is only 30 Mbps, this rate is chosen.

There are 10^4 bits sent from the transceiver to receiver. Figure 5.18 shows the BER performance of the UWB pulses through the LOS and NLOS channel models in the chosen bit rates. Fig 5.18 shows that the monocycle pulse is more robust than triplet both in LOS and NLOS channels.

For the monocycle pulse over the LOS channel, 400 Mbps is chosen. That means the pulse is sent in 2.5ns periodic time. It has BER in 10^{-3} level for SNR 10 dB, and BER in 10^{-4} level for SNR 12 dB, respectively. By estimation of the graph in Figure 5.18, data communication that needs BER 10^{-5} or less can be applied in SNR 13 dB or more.

For the triplet pulse over the LOS channel, 400 Mbps is also chosen. BER occurs in 10^{-3} level for SNR 12 dB, and in 10^{-4} level for SNR 14 dB, respectively. It can be estimated that BER 10^{-5} or less can be applied in SNR 15 dB or more.

For the monocycle pulse over the NLOS channel, 30 Mbps is implemented (0.33 ns pulse periodic time). It has BER in 10^{-4} level for SNR 18 dB. From the graph in Figure 5.18, it can be estimated that data communication with BER less than 10^{-4} level needs SNR 19 dB or more.

For the triplet pulse over the NLOS channel, 30 Mbps is chosen, since it is also the maximum rate. It has BER in 10^{-4} level at SNR 20 dB. Data communication that needs BER 10^{-5} or less can be applied in SNR 21-22 dB or more.

Chapter 6

CONCLUSIONS AND FUTURE RESEARCH

6.1. Conclusions

This Chapter summarizes the findings and concludes the dissertation. This dissertation consists of six chapters in total, and each of the previous five chapters addresses on one aspect of the UWB communication systems. The originalities and contributions of each chapter are summarized as follows.

After introduction, a new method of Ultra Wideband monocycle pulse generation is proposed in the chapter two. The circuit is based on $0.18\ \mu\text{m}$ CMOS. The design complies the spectral mask ruled by FCC. The proposed circuit has advantages in avoiding complexity and high power consumption. Reasonably good agreement between the measured and calculated results was also relatively achieved. The simplicity, low cost, and good performance of this circuit makes it attractive for various UWB radar and communications systems.

Chapter three describes about UWB modulation in the impulse radio (IR) systems systems. Some various modulation of impulse radio is presented. IR systems have the significant advantage of simplicity, and so are potentially lower cost. In addition, IR is essentially a baseband technique. The IR UWB concepts investigated support many modulation schemes including orthogonal and antipodal schemes. Basic modulation must also include some form of spectrum randomization techniques to limit the interference caused by the transmitted pulse train.

Chapter four describes about path loss model and channel model for UWB communication systems. It presents the time domain multipath model based on the S-V model. Different example channel characteristics that represent both LOS and NLOS channels is also presented. These characteristics are based on different mean excess delay, RMS delay spread, and mean number of paths. A new model based on S-V model is proposed.

An ultra high frequency analog multiplier is proposed in chapter five. The multiplier based on the MOS cascade operation circuit. The inputs are in voltage mode and become in current mode after multiplication. The simulation has shown that the multiplier has a flat frequency response up to 13GHz and can be applied for UWB communications. A new method of Ultra Wideband monocycle pulse generation is

applied. The circuit is based also on 0.18 μm CMOS. The design complies the spectral mask ruled by FCC. Reasonably good agreement between the measured and calculated results was also relatively achieved. The simplicity, low cost, and good performance of this circuit makes it attractive for various UWB radar and communications systems. The circuit is based on 0.18 μm CMOS technology simulated using HSPICE with level 49 and operates in $\pm 1\text{V}$.

The chapter also presents about The BER analysis of the Impulse Radio Ultra Wideband pulse communication over modified S-V channel model. The pulse is generated from circuit with HSPICE CMOS model level 49. The channel model is using generated of modified S-V model. Binary Pulse Amplitude Modulation is applied, and BER is measured over several of bit rates. The result shows that monocycle pulse over LOS and NLOS channel gives the best bit rates. Moreover, UWB communication is appropriate with high bit rates in LOS channel.

6.2. Future Research

Since UWB technology has a promising future for high-speed short-range applications, such as wireless LAN, home entertainment, wireless video downloading, etc., there still exist a significant amount of research opportunities in the future.

Conventional research issues inside the physical layer, such as UWB ISI reduction, data acquisition, clock synchronization, Doppler effects on UWB systems, UWB channel environments, multiple access, etc., are still attracting research attention. As the data rate becomes higher, new research issues across physical layer, link layer, and even upper layers are very attracting.

Other technologies such as wide band antennas, digitally tunable RF front end, software defined radio, ADC with higher sampling rate and more bits per sample, high-speed digital signal processor, etc., are also critical to the deployment of UWB communication systems. The future of UWB technology is bright and the research in this area will remain active in at least the near future.

REFERENCES

- [1] M. Ghavami, L. B. Michael, R. Kohno, "Ultra Wideband Signals and Systems in Communication Engineering," John Wiley & Sons, Ltd, West Sussex UK, 2004.
- [2] FCC 04-48 "First Report and Order in the Matter of Revision of Part 15 of the Commission's Rules Regarding Ultra-wideband Transmission Systems," Feb.14, 2002.
- [3] B. Razavi, T. Aytur, C. Lam, F. Yang, K. Li, R. Yan, H. Kang, C. Hsu, C. C. Lee, "A UWB CMOS Transceiver," IEEE Journal of Solid Stated Circuits, vol. 40, no. 12, pp. 2555-2562, Dec. 2005.
- [4] P. Prommasuksakul, P. Supanakoon, S. Promwong, and J. Takada, "Power Spectral Density Analysis of Ultra Wideband Signal Using Pulse Shape Modulation," Proc. of the 4th International Conference, ECTI-CON2007, Chiang Rai, pp.1186-1189, May 2007.
- [5] I. Oppermann, M. Hamalainen, J. Iinatti, "UWB Theory and Applications," John Wiley & Sons, West Sussex, 2004
- [6] S. Roy, J. R. Foerster, V. S. Somayazulu, and D. G. Leeper, "Ultrawideband radio design: the promise of high-speed, short-range wireless connectivity," Proc. IEEE, vol. 92, no. 2, pp. 295-311, Feb. 2004.
- [7] X. Chen, and S. Kiaei, "Monocycle shapes for ultra wideband system," Proc. of IEEE International Symposium on Circuits and Systems, vol. 1, pp. 597-600, May 2002.
- [8] J. F. M. Gerrits, and J. R. Farserotu, "Wavelet generation circuit for UWB impulse radio applications," Electronics Letters, vol. 38, issue 25, pp. 1737-1738, Dec. 2002.
- [9] H. Kim, D. Park, and Y. Joo, "Design of CMOS Scholtz's monocycle pulse generator," Proc. of IEEE Conference on Ultra Wideband Systems and Technologies, pp. 81-85, Nov. 2003.
- [10] H. Kim, D. Park, and Y. Joo, "All-digital low-power CMOS pulse generator for UWB system," Electronics Letters, Vol. 40, Issue 24, pp. 1534-1535, Nov. 2004.

- [11] A. Azakkour, M. Regis, F. Pourchet, and G. Alquie, "A new integrated monocycle generator and transmitter for ultra-wideband (UWB) communications," Proc. of IEEE Symposium on Radio Frequency integrated Circuits, pp. 79–82, June 2005.
- [12] S. Yoshizumi, T. Terada, J. Furukawa, Y. Sanada, and T. Kuroda, "All digital transmitter scheme and transceiver design for pulse-based ultra-wideband radio," Proc. of IEEE Conference on Ultra Wideband Systems and Technologies, p.438– 442, Nov. 2003.
- [13] J. Han, and C. Nguyen, "A new ultra-wideband, ultra-short monocycle pulse generator with reduced ringing," IEEE Microwave and Wireless Components Letters, vol. 12, issue 6, pp. 206–208, June 2002.
- [14] R. Hidayat, K. Dejhani, P. Moungnoul, and Y. Miyanaga, "A 0.18 μ m CMOS Gaussian Monocycle Pulse Generated for Ultra-Wideband system," Proc. of The International Technical Conference on Circuits/Systems, Computers and Communications, pp. I-5–I-8, July 2006.
- [15] T. Y. Choi, W. I. Cho, and D. W. Kim, "A simple CMOS delay model for wide applications," Proc. of IEEE Asia Pacific Conference on Circuits and Systems, pp. 77–80, Nov. 1996.
- [16] D. A. Hodges, H. G. Jackson, and R. A. Saleh, ed., Analysis and Design of Digital Integrated Circuits, McGraw-Hill, 2003.
- [17] Y. Tsividis, Operation and Modeling of The MOS Transistor, McGraw Hill, 1999.
- [18] <http://www.mosis.org/Technical/Testdata/tsmc-018-prm.html>
- [19] G. Breed, "A Summary of FCC Rules for Ultra Wideband Communications ," <http://www.highfrequencyelectronics.com/Archives/Jan05/>
- [20] Y. H. Choi, "Gated UWB Pulse Signal Generation," Proc. of IEEE Conference on Ultra Wideband Systems and Technologies, pp. 122-124, May 2004.
- [21] R. Scholtz, "Multiple access with time-hopping impulse modulation," Proc. of IEEE Conference on Military Communications, MILCOM '93, vol. 2, pp.447 – 450, Oct. 1993
- [22] M. .Z. Win, R. A. Scholtz, "Ultra-Wide Bandwidth Time-Hopping Spread-Spectrum Impulse Radio for Wireless Multiple-Access Communications," *IEEE Trans. Commun.*, vol. 58, no. 4, pp.679-691, April 2000.

- [23] J. Foerster, Q. Li, "UWB Channel Modeling Contribution from Intel," IEEE JSAC 2002.
- [24] A. M. Saleh, R. A. Valenzuela, "A statistical model for indoor multipath propagation," *IEEE Journal on Selected Areas In Communications*, vol. SAC-5, no. 2, pp. 128- 137, Feb. 1987.
- [25] H. Suzuki, "A Statistical Model for Urban Radio Propagation," IEEE Transactions on Communications, pp. 673-680, July 1977.
- [26] H. Hashemi, "Impulse Response Modeling of Indoor Radio Propagation Channels," IEEE JSAC, Vol. 11, No. 7, pp. 967-978, Sept. 1993.
- [27] K. Siwiak, D. McKeown, "Ultra-Wideband Radio Technology," John Wiley & Sons, West Sussex, 2004
- [28] H. Gunhee, S. Sanchez-, "MOS transconductance multipliers: a tutorial," IEEE Transactions on Circuits and Systems II: Analog and Digital Signal Processing, vol. 45, Issue 12, pp. 1550–1563, Dec. 1998.
- [29] S. Hongsan, P. Orlik, A.M. Haimovich, L. J. Jr. Cimini, and Z. Jinyun, "On the Spectral and Power Requirements for Ultra-Wideband Transmission," Proc. of IEEE Conf. on Communications vol. 1, pp. 738 – 742, May 2003.
- [30] H. J. Song, C. K. .Kim, "An MOS four-quadrant analog multiplier using simple two-input squaring circuits with source followers," IEEE Journal of Solid-State Circuits, vol. 25, Issue 3, pp. :841 – 848, June 1990.
- [31] B. Boonchu, W. Surakamponorn, "A new NMOS four-quadrant analog multiplier," Proc. of IEEE Int. Symp. on Circuits and Systems, ISCAS, 23-26, vol. 2, pp. 1004 – 1007, May 2005.
- [32] S. Szczepanski, S. Koziel, "1.2V low-power four-quadrant CMOS transconductance multiplier operating in saturation region," Proc. of Int. Symp. on Circuits and Systems, vol. 1, pp. I-1016-19, May 2004
- [33] M. Kumngern, K. Dejhan, "Versatile dual-mode class-AB four-quadrant analog multiplier," International Journal of Signal Processing, vol. 2, No. 3, pp. 214-221, Dec. 2005.
- [34] R. J. Wiegerink, "A CMOS four-quadrant analog current multiplier," Proc. of IEEE Int. Symp. on Circuits and Systems, vol. 4, pp. 2244-2247, June 1991.

- [35] L Zhou., Y. P. Xu, F. Lin, "A gigahertz wideband CMOS multiplier for UWB transceiver," Proc of IEEE Int. Symp. on Circuits and Systems, vol. 523-26, pp. 5087–5090, May 2005.



LIST OF PUBLICATIONS

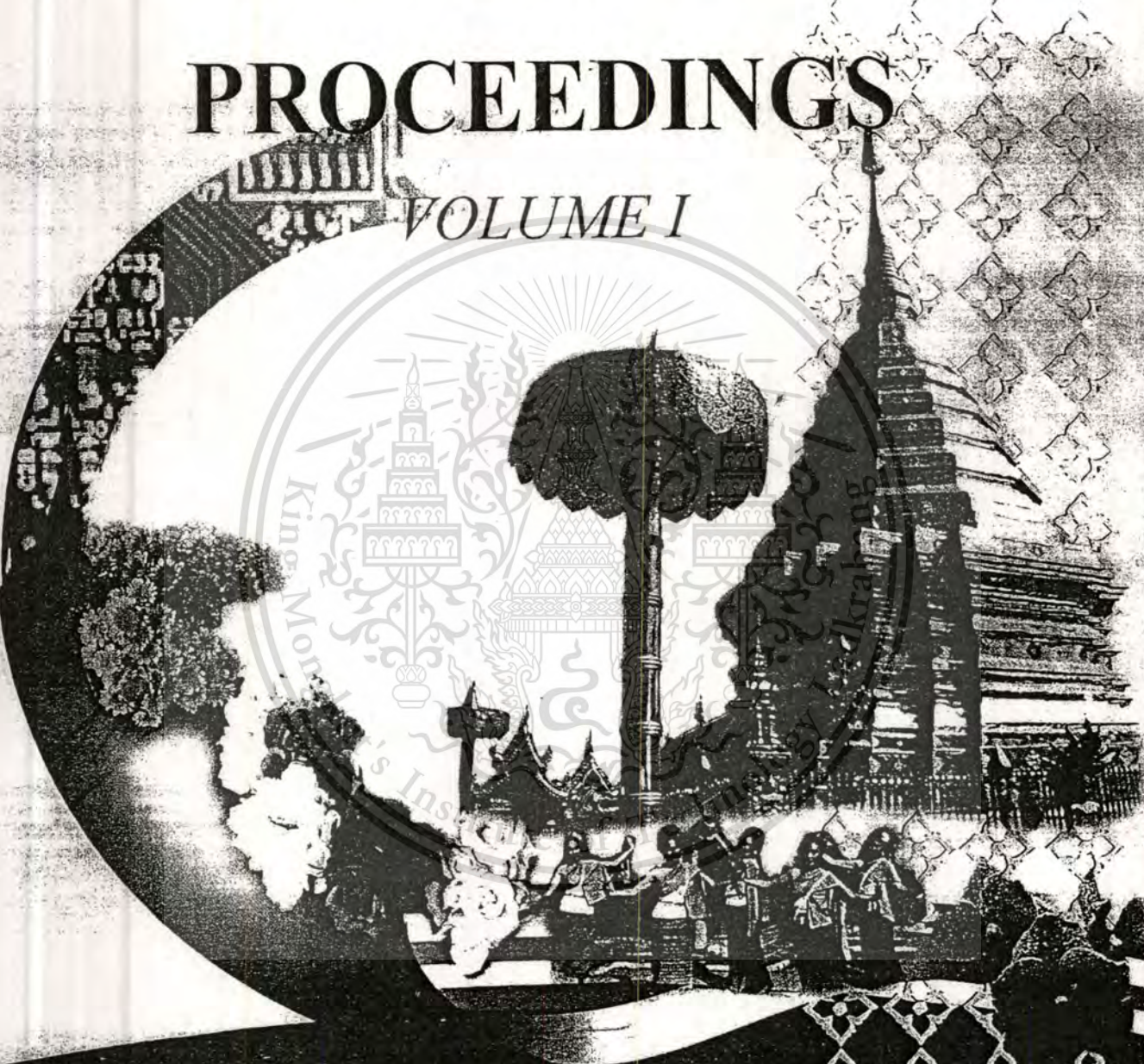
1. R Hidayat, K Dejhan, P Moungnoul, Y Miyanaga , “0.18 μm CMOS Gaussian Monocycle Pulse Generated for Ultra-Wideband System,” Proc. of International Technical Conference on Circuits/Systems, Computers and Communications (ITC-CSCC 2006), pp. I-5 – I-8, Chiang Mai, Thailand, 10-13 July, 2006.
2. R Hidayat, K Dejhan, P Moungnoul, Y Miyanaga , “A 0.18 μm CMOS Gaussian Monocycle Pulse Circuit Design for UWB,” Proc. of IEEE Asia Pacific Conference on Circuits and Systems (APCCAS2006), pp. 89-92, Singapore, 4 - 7 December, 2006.
3. R Hidayat, K Dejhan, P Moungnoul, Y Miyanaga , “A GHz Analog Multiplier for UWB Communications,” Proc. of Asia Pacific Conference on Communications 2007 (APCC 2007), pp. 55-58, Bangkok, Thailand, 18 - 20 October, 2007.
4. R Hidayat, K Dejhan, P Moungnoul, Y Miyanaga , “BER Analysis of IR-UWB Communication Over Modified S-V Channel Model,” Proc. of The 2007 Joint International Conference on Information Communication Technology (JICT 2007), pp.227-232, National University of Laos (NUOL), 19-22 Dec, 2007.
5. R Hidayat, K Dejhan, P Moungnoul, Y Miyanaga , “A GHz Simple CMOS Squarer Circuit,” Proc. of International Symposium on Communications and Information Technologies 2008 (ISCIT 2008), pp. 539-542, Vientiane, Lao PDR, 21 - 23 October, 2008.
6. R Hidayat, K Dejhan, P Moungnoul, Y Miyanaga , “BER Analysis of IR-UWB Communication Over Modified S-V Channel Model,” accepted to be published in Journal of Signal Processing, September 2009, Japan.

ITC-CSCC 2006

*The International Technical Conference on
Circuits/Systems, Computers and Communications*

PROCEEDINGS

VOLUME I



Sponsored By

THE ELECTRICAL ENGINEERING/ELECTRONICS, COMPUTER, TELECOMMUNICATIONS AND INFORMATION ASSOCIATION (ECTI), THAILAND

THE INSTITUTE OF ELECTRONICS ENGINEERS OF KOREA (IEEK), KOREA

THE INSTITUTE OF ELECTRONICS, INFORMATION AND COMMUNICATION ENGINEERS (IEICE), JAPAN

NATIONAL ELECTRONICS AND COMPUTER TECHNOLOGY CENTER, THAILAND

In association with IEEE THAILAND SECTION

© 2006 IEEE. All rights reserved. This material is reserved for educational use only, not allowed for commercial use.

Forbidden to modify the content, and cite the document when use.

0.18 μm CMOS Gaussian Monocycle Pulse Generated for Ultra-Wideband System

Risanuri Hidayat Kobchai Dehjan Phichet Moungnoul Yoshikazu Miyanaga*

Faculty of Engineering and Research Center for Communication and Information Technology
King Mongkut's Institute of Technology Ladkrabang, Chalongkrung Road, Bangkok 10520, THAILAND
Phone: +66-2-3264242, Fax: +66-2-3264554, E-mail: (risanuri,kobchai,phichet)@telecom.kmitl.ac.th

*Graduate School of Information Science and Technology Engineering, Hokkaido University, Sapporo 060-8628, JAPAN

ABSTRACT

This paper proposes the new method of monocycle pulse generation in this paper, to generate Gaussian pulse, and then generate first derivative of the pulse to get a Scholtz's monocycle pulse. The circuit simulated the generation based on 0.18 μm CMOS technology achieved using HSPICE (Level 49). The Gaussian pulse is generated by CMOS inverter of which we apply the delay time to perform the Gaussian pulse.

Keywords: UWB, monocycle pulse generation

1. INTRODUCTION

Ultra-Wideband (UWB) radio is defined as wireless technology to transmit data over the very wide spectrum of frequency bands with very low signal power [3]. Since signal has very short pulse duration in time, very high data rate can be achieved for next generation wireless communication systems. Federal Communications Commission (FCC) released unlicensed 3.1-10.6 GHz frequency band for Ultra-Wideband (UWB) related applications [3].

Several monocycle pulse shapes were introduced [5]. Some researches have published pulse generators for UWB in circuit level [1],[3],[4]. This paper, attempts to generate Gaussian monocycle using CMOS technology. The pulse generation is achieved by CMOS inverter that have same delay of time in the response of the step input, and the Gaussian function can be approximated by hyperbolic tangent (\tanh) function of the second inverter. The circuit is simulate the pulse generation based on 0.18 μm CMOS technology achieved using HSPICE (Level 49)

In section 2, it will be discussed about Gaussian monocycle pulse shape that is considered within the FCC emission limitation. In section 3, the way to generate Gaussian monocycle pulse will be proposed. In section 4, the proposed monocycle pulse generation circuit is explained and simulated. Finally, section 5 is summarized.

2. GAUSSIAN PULSE FOR UWB

Ultra Wideband (UWB) technology is at present defined by the Federal Communications Commission

(FCC) as any wireless transmission scheme that occupies a fractional bandwidth $W/f_c \geq 20\%$ where W is the transmission bandwidth and f_c is the band center frequency, or more than 500 MHz of absolute bandwidth. The FCC recently approved the deployment of UWB on an unlicensed basis in the 3.1-10.6 GHz band subject to a modified version of Part 15.209 rules. The essence of this ruling is to limit the *power spectral density* (PSD) measured in a 1-MHz bandwidth at the output of an isotropic transmit antenna is shown in Fig. 1.

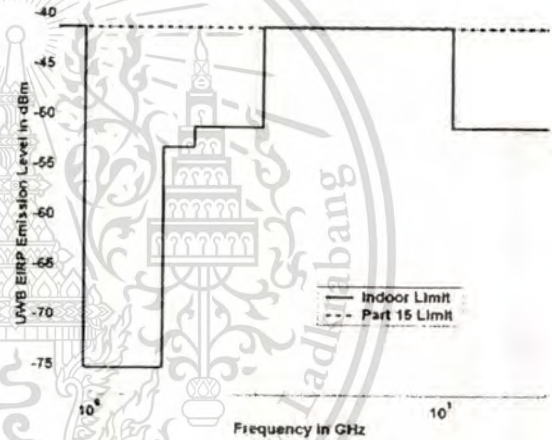


Fig 1: UWB spectral mask and FCC Part 15 limit.

Some references have represented several kind formula of Gaussian pulse [3],[5], but we can conclude Gaussian monocycle, its first derivative (monocycle) and its second derivative (monocycle) represented by

$$x(t) = A_1 \cdot e^{-A_2 t^2} \quad (1)$$

The first derivative of Gaussian pulses are usually called as 'monocycle' is given by (2).

$$\dot{x}(t) = A_2 t \cdot e^{-A_2 t^2} \quad (2)$$

Fig. 2 shows the Gaussian pulse waveform and monocycle of the pulse.

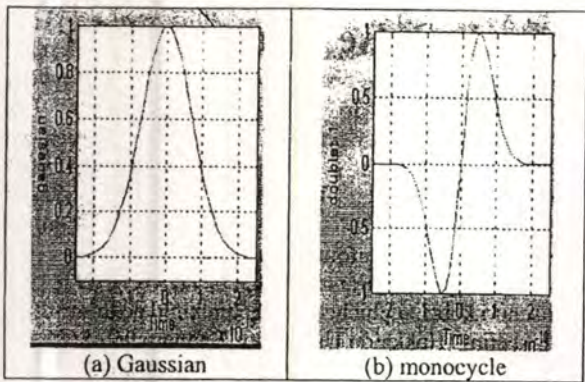


Fig. 2: Gaussian pulse waveform

3. CMOS INVERTER

A paper proposed about time delay of the inverter [5]. In high frequency, a CMOS includes capacitance. The capacitance is comprised of three components: the self-loading, the wire and the fanout capacitances [2]. Suppose that the wire is very short such that the wire capacitance can be eliminated. For delay calculation, to sum these individual quantities to obtain a lumped capacitance.

$$C_L = C_{self} + C_{wire} + C_{fanout} \quad (3)$$

The capacitances for each fanout, assume that all inverters have the same value, are illustrated in Fig. 3.

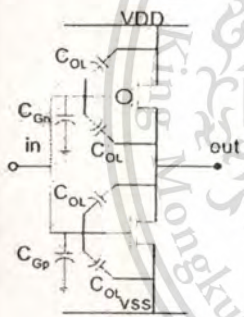


Fig. 3: Input/fanout capacitance

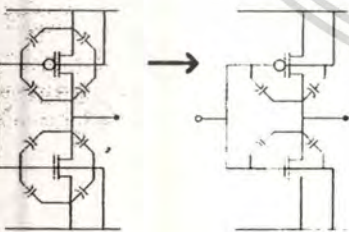


Fig. 4: Output/self capacitance

Each transistor has a term due to the thin-oxide and two terms due to the overlap capacitance. The capacitances that must be taken into account are C_{Gm} , C_{Gp} , and C_{OL} . The self-capacitance is the sum of the capacitances connected to the output. Fig. 4 shows the important terms to include in the self-capacitance.

There are four main capacitances for each transistor: C_{GS} , C_{GD} , C_{DB} and C_{SB} . Eliminate four of them, C_{GSp} , C_{SBp} , C_{GSn} and C_{SBn} , since these are not connected to the output. If there is a step input in either direction, one transistor is always off while the other one is in saturation. Suppose that t_{PHL} or t_{PLH} involves a transition to the 50% point, it can be assumed that the transistors are in saturation or cutoff. In either region, the gate-to-drain capacitance, C_{GD} is negligible. This leaves only the overlap capacitances from gate-to-drain, and one junction capacitance per device, C_{DBn} and C_{DBp} .

The total self-capacitance of the inverter now can be computed. It is simply the junction capacitances plus the overlap capacitances due to fringing and lateral diffusion.

$$\begin{aligned} C_{self} &= C_{DBn} + C_{DBp} + 2C_{OL} + 2C_{OL} \\ &= C_{jn} W_n + C_{jn} W_p + 2C_{ov} (W_n + W_p) \\ &= C_{eff} (W_n + W_p) \end{aligned} \quad (4)$$

The propagation delay for step case in one inverter is computed by equation as follows, [2]

$$i_{out} = i_{max} = C_L \frac{dV_{out}}{dt} = C_L \frac{(V_{DD} - V_{SS})/2}{t_{PHL,step}} \quad (5)$$

$$t_{PHL,step} = C_L \frac{(V_{DD} - V_{SS})/2}{i_{max}}$$

The propagation delay for ramp case can be derived as follows,

$$t_{PHL,RAMP} = \frac{t_r}{4} + \frac{C_L (V_{DD} - V_{SS})/2}{i_{max}} \quad (6)$$

$$t_{PHL,RAMP} = \frac{t_r}{4} + t_{PHL,step}$$

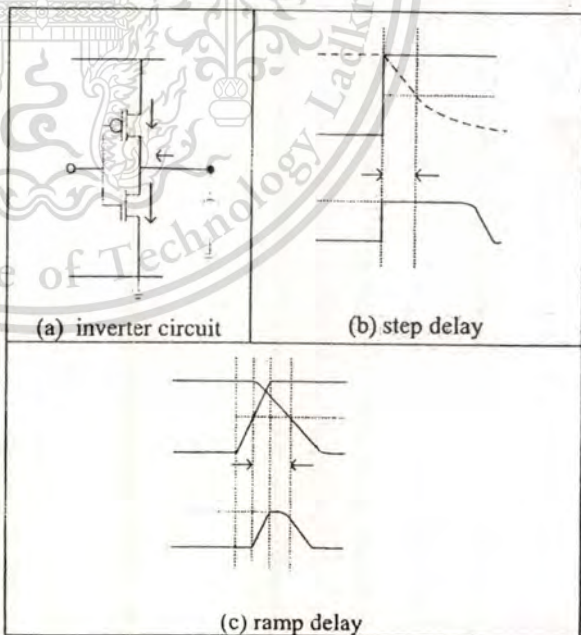


Fig. 5: Propagation delay of inverter

If we use the approximation that $t_r \cong 2t_{PHL_step}$, then

$$t_{PHL_RAMP} = \frac{t_{PHL_step}}{2} + t_{PHL_step} \quad (7)$$

Fig. 5 shows about the propagation delay.

On the other hand, Voltage Transfer Characteristic (VTC) of CMOS inverter can be considered as hyperbolic tangent function $\tanh(x)$, as shown in Figure 6. Since the inverter delay becomes input of the next inverter and the VTC, we can perform a Gaussian function using inverters.

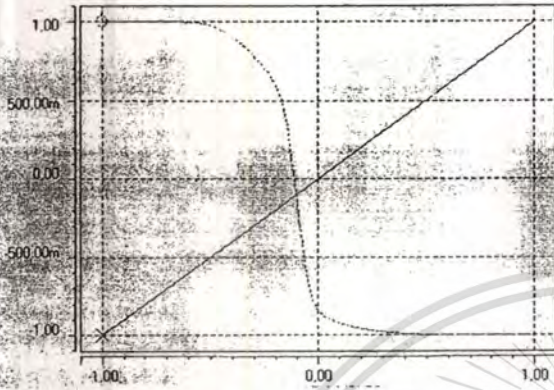


Fig 6: VTC of inverter

4. SIMULATION RESULTS

Fig. 7 shows the proposed technique to generate the UWB Gaussian monocycle. It consists of three inverters, and derivative circuits. The input is pulse of which the width is compromised with the inverter delay. By satisfying that requirement, a Gaussian pulse then can be performed.



Fig 7: Monocycle pulse generation circuit

The whole circuit is designed using standard 0.18 μm CMOS technology with ± 1 V power supply and simulated in HSPICE (Level 49). The first and second inverter use small size of CMOS ($L=0.5$, $W=1.5$), such that the delay in node INVI is relatively very small.

The third inverter uses much larger size ($L=0.5$, $W=700$), and it generates the derived delay. Figure 8 shows the timing diagram from the circuit. First row is the input pulse coming from data. Suppose that Data has been processed and generates an appropriate pulse, 0.14ns pulse width. Since node INVI delay is so little, we concern only to the delay in node IN2. Output IN2

generates a delay to appreciate the pulse input, as shown the second row in the fig. 8.

The delay function is not really linear as shown in Figure 8. However, voltage transfer characteristic still generates response of tanh function, as shown in the third row in the figure. By using pulse input, it will yield a Gaussian pulse at node GS0. Finally, the fourth row is the derivative of the Gaussian, by using RC circuit at node GS1. We observe delay performance from simulation in Table 1. Note that Gaussian Pulse width is observed from 5% of $(V_{DD}-V_{SS})$, or -0.8 V.

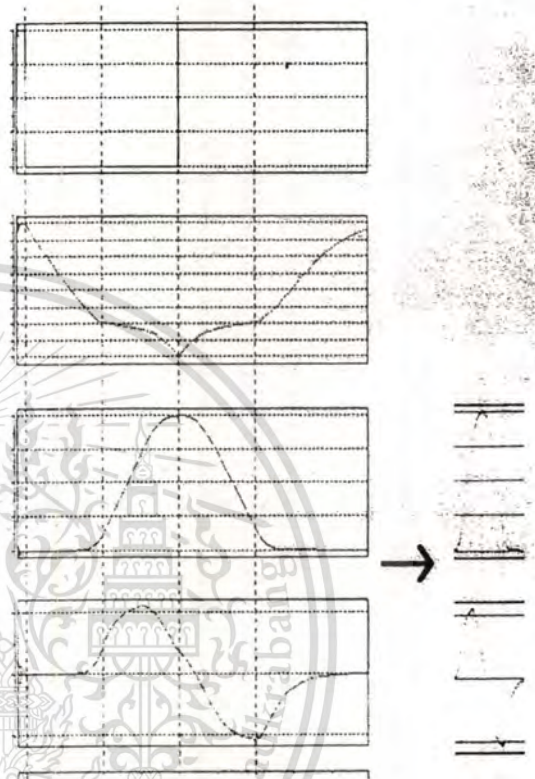


Fig. 8: Timing diagram

For monocycle pulse (the first derivative of Gaussian pulse), it is noted that there is no smooth pulse in monocycle. To supposed that comes from unsmooth of Gaussian pulse but it can be negligible because it is very little. But in monocycle, the unsmooth graph becomes more visible, also for doublet 2, doublet 3, and so on.

Table 1. Delay Performance

Input Pulse width	2 ns
t_{PHL_step}	0.78 ns
t_{PLH_step}	0.27 ns
Delay time	0.525 ns
Gaussian Pulse width	2.08 ns

5. CONCLUSION

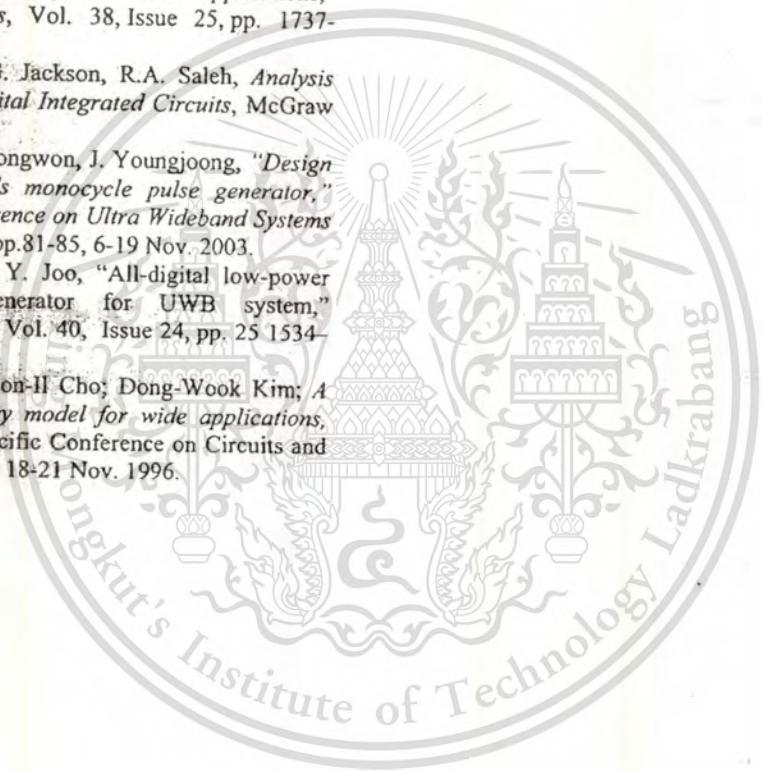
The generated Gaussian pulse, and then generated first derivative of the pulse applying delay of inverter to get a Scholtz's monocycle pulse has been proposed. Simulation of the generation based on 0.18 μm CMOS technology achieved using HSPICE (Level 49). The result shows that the pulses are appreciated for Gaussian pulse and has unsmooth pulse for first derivative pulse. The proposed generation is not appropriate for more derivative Gaussian pulse.

6. ACKNOWLEDGMENTS

The authors would like to thank ASEAN University Network/Southeast Asia Engineering Education development Network (AUN/SEED-Net) for the financial support of this research.

7. REFERENCES

- [1] J.F.M. Gerrits, J.R. Farserotu, "Wavelet generation circuit for UWB impulse radio applications," *Electronics Letters*, Vol. 38, Issue 25, pp. 1737-1738, Dec. 2002.
- [2] D.A. Hodges, H.G. Jackson, R.A. Saleh, *Analysis and Design of Digital Integrated Circuits*, McGraw Hill, 2003.
- [3] K. Hyunseok, P. Dongwon, J. Youngjoong, "Design of CMOS Scholtz's monocycle pulse generator," *2003 IEEE Conference on Ultra Wideband Systems and Technologies*, pp.81-85, 6-19 Nov. 2003.
- [4] H. Kim, D. Park, Y. Joo, "All-digital low-power CMOS pulse generator for UWB system," *Electronics Letters*, Vol. 40, Issue 24, pp. 25 1534-1535, Nov. 2004.
- [5] Tae-Yong Choi, Won-II Cho, Dong-Wook Kim, *A simple CMOS delay model for wide applications*, 1996 IEEE Asia Pacific Conference on Circuits and Systems, pp. 77-80, 18-21 Nov. 1996.



IEEE Catalog Number : 06EX1378C
ISBN 1-4244-0387-1
Library of Congress: 2006923660

Proceedings

APCCAS 2006

2006 IEEE Asia Pacific Conference on Circuits and Systems

4-7 December 2006
Singapore

- Welcome
- Committees
- Table of Contents
- Keynotes
- Technical Program
- Author Index
- Search



© 2006 IEEE. Personal use of this material is permitted. However, permission to reprint / republish this material for advertising or promotional purposes or for creating new collective works for resale or redistribution to servers or lists, or to reuse any copyrighted component of this work in other works must be obtained from the IEEE.

Tuesday - December 5, 2006

D1-AM1-RM4 - Smart Multi-Media Systems (Special Session)

Time : 1120 - 1250
Room : Galleria !!!
Chair(s) : Yoshikazu Miyanaga

- | | | |
|--------------|---|----|
| D1-AM1-RM4.1 | 3D Shape Acquisition and Arbitrary View Image Generation from Monocular Image based on Primitive Decomposition
K Kondo, A Yamachika, S Kobashi, Y Hata
University of Hyogo, JAPAN | 73 |
| D1-AM1-RM4.2 | Cauchy Based Rate-Distortion Optimization Model for H.264 Rate Control
N Eiamjumrus, S Aramvith
Chulalongkorn University, THAILAND | 77 |
| D1-AM1-RM4.3 | A Fast Watermarking System for H.264/AVC Video
C V Nguyen, D B H Tay, G Deng
La Trobe University, AUSTRALIA | 81 |
| D1-AM1-RM4.4 | A New Efficient Approach for Removal of Impulse Noise for Color Images
Y Wakabayashi, A Taguchi
Musashi Institute of Technology, JAPAN | 85 |
| D1-AM1-RM4.5 | A 0.18 μ m CMOS Gaussian Monocycle Pulse Circuit Design for UWB
R Hidayat, K Dejhan, P Moungnoul, *Y Miyanaga
King Mongkut's Institute of Technology, Ladkrabang, THAILAND
*Hokkaido University, JAPAN | 89 |
| D1-AM1-RM4.6 | VLSI Implementation of a 600-Mbps MIMO-OFDM Wireless Communication System
S Yoshizawa, Y Miyanaga
Hokkaido University, JAPAN | 93 |

A 0.18 μm CMOS Gaussian Monocycle Pulse Circuit Design for UWB

Risanuri Hidayat, Kobchai Dejhan,
Phichet Moungroul

Faculty of Engineering and Research Center for
Communication and Information Technology.

King Mongkut's Institute of Technology Ladkrabang,
Ladkrabang, Bangkok 10520, Thailand.

Email: {risanuri,kobchai, phichet}@telecom.kmitl.ac.th

Yohikazu Miyanaga

Division of Media and Network technologies
Graduate School of Information Science and Technology,

Hokkaido University

Sapporo 060-8628, Japan

Email: miya@ist.hokudai.ac.jp

Abstract—This paper proposes a new method of monocycle pulse generation by generating the Gaussian pulse, and generate first derivative of the pulse to get a Scholtz's monocycle pulse. The simulation result of the generation is based on 0.18 μm CMOS technology which achieved using HSPICE (Level 49). The Gaussian pulse is generated by using CMOS inverter of which is applied the delay time to perform the Gaussian pulse.

Keywords—gaussian pulse, monocycle pulse, CMOS inverter, UWB

I. INTRODUCTION

Ultra-Wideband (UWB) radio is defined as a wireless technology to transmit data over a very wide spectrum of frequency bands with very low power [1]. Since its signal has very short pulse duration in time, very high data rate can be achieved for next generation wireless communication systems. Federal Communications Commission (FCC) released unlicensed 3.1-10.6 GHz frequency band for Ultra-Wideband (UWB) related applications [1].

Several monocycle pulse shapes were introduced [1]. Some researches have published pulse generators for UWB in circuit level [1] [2] [3]. In this paper, the authors attempt to generate Gaussian monocycle using CMOS technology. The pulse generation is achieved by CMOS inverter that have some delay of time in the response of step input, and the Gaussian function can be approximated by hyperbolic tangent (tanh) function of the second inverter. The simulation is carried out for the pulse generation based on 0.18 μm CMOS technology achieved using HSPICE (Level 49).

II. GAUSSIAN PULSE FOR UWB

Some references have represented several kind formula of Gaussian pulse [1] [4], but it can be concluded that Gaussian pulse and its first derivative (monocycle) represented by the expression

$$x(t) = A_1 \cdot e^{-2\left(\frac{\pi t}{T_c}\right)^2} \quad (1)$$

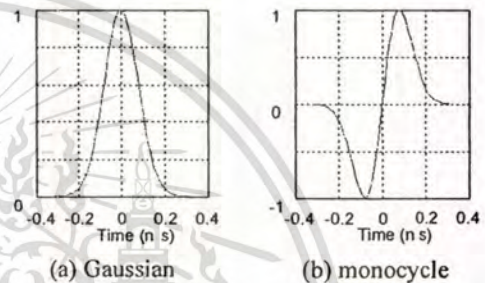


Figure 1. Gaussian pulse waveform.

The first derivative of Gaussian pulses are usually called as 'monocycle' is given by

$$\dot{x}(t) = \frac{dx(t)}{dt} = A_2 t \cdot e^{-2\left(\frac{\pi t}{T_c}\right)^2} \quad (2)$$

where T_c is the width of the pulse, and A_k are amplitudes. Fig. 1 shows the Gaussian pulse waveform and monocycle of the pulse, and also shows their frequency spectra.

III. CMOS INVERTER

Some papers have proposed about time delay of the inverter [4]. In high frequency, a CMOS includes capacitance. Fig. 2 shows about the capacitance of the CMOS inverter. The capacitance is comprised of three components: the self-loading, the wire and the fanout capacitances [5]. Suppose that the wire is very short such that the wire capacitance (C_{wire}) can be eliminated. For delay calculation the sum of these individual quantities can be obtained as a lumped capacitance.

$$C_L = C_{\text{self}} + C_{\text{wire}} + C_{\text{fanout}} \quad (3)$$

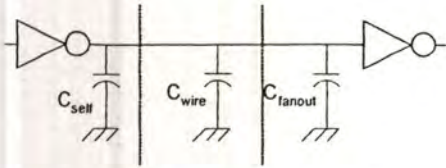


Figure 2. Gaussian pulse waveform.

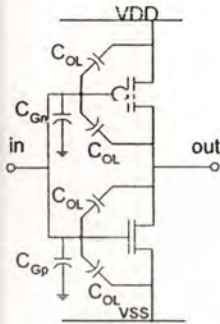


Figure 3. Input/fanout capacitance

where C_L is total load capacitance, C_{self} is the self capacitance, can be defined as the output capacitance of the first inverter, and C_{fanout} is fanout capacitance, that is the input capacitance of the second inverter in Fig. 2.

The capacitances for each fanout, assuming that they are all inverters, are illustrated in Fig. 3. Each transistor has a term due to the thin-oxide and two terms due to the overlap capacitance. C_{fanout} is the capacitance connected to the input of the inverter. Since both PMOS and NMOS have thin-oxide and also overlap capacitances, C_{fanout} can be expressed as [5],

$$C_{fanout} = C_{Gn} + C_{OLGDn} + C_{OLGSp} + C_{Gp} + C_{OLGDp} + C_{OLGSp} \quad (4)$$

where $C_{Gn,p}$ is the capacitances of the thin-oxide for MOS. $C_{OLGDn,p}$ and C_{OLGSp} are the overlap capacitances between gate-drain and between gate-source. The subscript either n or p identify for NMOS and PMOS respectively. The thin-oxide capacitance has expression as, [5]

$$C_{Gn,p} = \frac{1}{2} C_{ox} W_{n,p} L_{n,p} \quad (5)$$

$$C_{ox} = \frac{\epsilon_{ox}}{t_{ox}} \quad (6)$$

where C_{ox} is the thin-oxide capacitance per unit area. W and L are channel width and channel length. ϵ_{ox} is the permittivity of the oxide and t_{ox} is the oxide thickness. The

overlap capacitance, C_{OL} , is comprised of the overlap capacitances between gate-drain (C_{OLGD}) and between gate-source (C_{OLGS}). These can be expressed as [5]

$$C_{OLGD} = C_{GDO} \cdot W$$

$$C_{OLGS} = C_{GSO} \cdot W \quad (7)$$

C_{GDO} is the gate-drain overlap capacitances per unit gate width, and C_{GSO} is the gate-source overlap capacitances per unit gate width. The values are modeled in the SPICE simulation. When C_{GDO} and C_{GSO} values are the same, then $C_{OLGD} = C_{OLGS} = C_{OL}$. Therefore, eq. (4) can be expressed as

$$C_{fanout} = (C_{ox} L)(W_n + W_p) + 2C_{OLn} W_n + 2C_{OLp} W_p \quad (8)$$

The self-capacitance, C_{self} , is the capacitances connected to the output. Fig. 4 illustrates the important terms to include in the self-capacitance. Suppose that delay time (t_{PHL} or t_{PLH}) involves a transition to the 50% point, it can be assumed that the transistors are in saturation or cutoff. In either region, the thin-oxide gate-drain capacitance is negligible [5]. The total self-capacitance can be expressed as the junction capacitances plus the overlap capacitances as follows,

$$C_{self} = 2C_{OLGDn} + 2C_{OLGDp} + C_{DBn} + C_{DBp} \quad (9)$$

where $C_{OLGDn,p}$ is the overlap capacitances from gate-to-drain. Again, the subscript either n or p identify for NMOS and PMOS respectively. These have a double value of the capacitance because of commonly referred as Miller effect modeling [5]. $C_{DBn,p}$ are the one junction capacitance between drain-bulk per device. The capacitances are formulated in eq. (10).

$$C_{DBn,p} = \frac{CJ \cdot A_D}{\left(1 - \frac{V_J}{PB}\right)^{MJ}} + \frac{CJSWG \cdot P_D}{\left(1 - \frac{V_J}{PB}\right)^{MJSWG}} \quad (10)$$

where CJ and $CJSWG$ are the source/drain bottom junction capacitance and the zero-bias gate-edge sidewall bulk junction capacitance, respectively. MJ and $MJSWG$ respectively are the grading coefficient of the bottom-wall junction capacitance and grading coefficient of the gate-edge sidewall junction capacitance. PB is the built-in potential of the bottom-wall junction capacitance. A_D and P_D are respectively the drain area and drain perimeter. Finally, V_J is the junction voltage, voltage drop across the junction of the transistor.

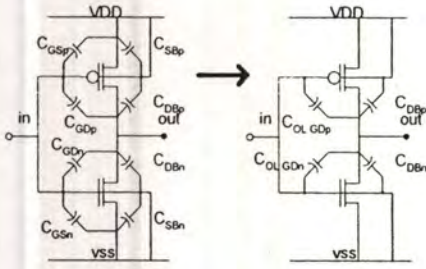


Figure 4. Output/self capacitance

The CMOS inverter then can be illustrated as in Fig. 5, with C_L is described in eq. (3). The propagation delay for step case and ramp case in one inverter can be expressed respectively as,

$$t_{PHL,step} = \left(\frac{(V_{DD} - V_{SS})/2}{i_{max}} \right) \cdot C_L \quad (11)$$

$$t_{PHL} = t_{PHL,RAMP} \approx \frac{t_{PHL,step}}{2} + t_{PHL,step} \quad (12)$$

As t_{PHL} or t_{PLH} involves a transition to the 50% point, the delay for an inverter can be calculated as in eq. (13), and illustrated in Fig. 5 [5].

$$t_{PHL} = R_{eff,NMOS} \frac{L}{W} \cdot C_L \quad (13)$$

$$t_{PLH} = R_{eff,PMOS} \frac{L}{W} \cdot C_L$$

where t_{PHL} and t_{PLH} are delay time from high to low and from low to high respectively, while R_{eff} is the effective resistance of the transistor. L , W and C_L have the same definition previously.

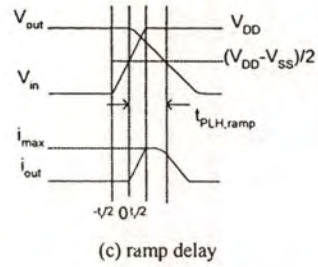
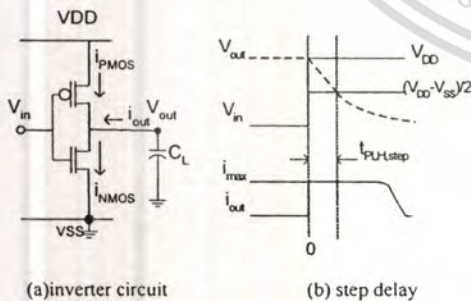


Figure 5. Propagation delay of inverter

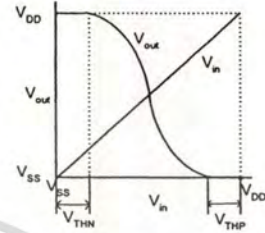


Figure 6. VTC of the CMOS inverter

IV. GUSSIAN PULSE GENERATION

Voltage Transfer Characteristic (VTC) of CMOS inverter in Fig. 5(a) can be considered as hyperbolic tangent function $\tanh(x)$, as shown in Fig. 6. V_{THN} and V_{THP} are threshold voltage of NMOS and PMOS respectively. Since the inverter delay becomes input of the next inverter and the VTC, let perform a Gaussian function using inverters.

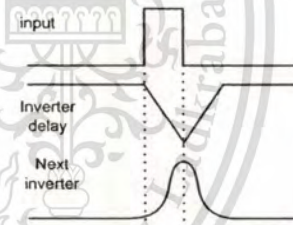


Figure 7. The Gaussian pulse generation principle

Fig. 7 shows about the principle of the Gaussian pulse generation. A square pulse input has delay, and it will be responded by inverters to perform a Gaussian pulse. Once the Gaussian pulse is gotten, it can be differentiated by a differential circuit to get its differential function as shown in eq. (2).

V. SIMULATION RESULTS

Fig. 8 shows the proposed technique to generate the UWB Gaussian monocycle. It consists of three inverters, and derivative circuits. The input is pulse of which the width is compromise with the inverter delay. By satisfying that requirement, a Gaussian pulse then can be performed.

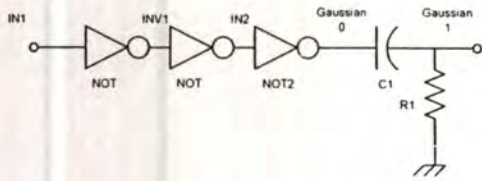


Figure 8. Monocycle pulse generation circuit

The whole circuit is designed using standard $0.18 \mu\text{m}$ CMOS technology with $\pm 1 \text{ V}$ power supply and simulated in HSPICE (Level 49). The first and second inverter use small size of CMOS's ($L/W=0.18 \mu\text{m} / 0.27 \mu\text{m}$), such that the delay in node INV1 is relatively very small.

The third inverter use much larger size ($L/W=0.18 \mu\text{m} / 2.7 \mu\text{m}$), and it generates the derived delay. Fig. 9 shows the timing diagram from the circuit. First row, Fig. 9(a), is the input pulse coming from data. Suppose that Data has been processed and generates an appropriate pulse. The pulse width minimum is 0.14ns . The delay at INV1 is negligible; the attention is to the delay at IN2. Output of IN2 generates a delay to appreciate the pulse input, as shown in the second row, Fig. 9(b).

The delay function is not really linear as shown in Fig. 9(b). However, the voltage transfer characteristic still generates response of tanh function, as shown in the third row, Fig. 9(c). By using pulse input, it will generate a Gaussian pulse at GS0. Finally, the fourth row, Fig. 9(d), is the derivative of the Gaussian, by using RC circuit at GS1. The performance is shown in Table 1. The table shows both the simulation and calculation results. The calculation uses equations in eq. (13) and its roots above. There are differences between them, but it is in tolerances.

For monocycle pulse (the first derivative of Gaussian pulse), it is noted that there is no smooth pulse in monocycle, and can estimate it comes from unsmooth of Gaussian pulse but it can be negligible because it is very little. But in monocycle, the unsmooth graph becomes more visible, also for the more derivative pulse, doublet 2, doublet 3, and so on.

VI. CONCLUSION

The monocycle pulse generation is proposed in this paper. To generate Gaussian pulse, and then generate first derivative of the pulse applying delay of inverter to get a Scholtz's monocycle pulse have been proposed. Simulation of the generation based on $0.18 \mu\text{m}$ CMOS technology achieved using HSPICE (Level 49). The result shows that the pulses is appreciated for Gaussian pulse and has unsmooth pulse for first derivative pulse. The proposed generation is not appropriate for more derivative Gaussian pulse.

REFERENCES

- [1] H. Kim, D. Park, Y. Joo, Design of CMOS Scholtz's monocycle pulse generator, IEEE Conference on Ultra Wideband Systems and Technologies, 16-19 Nov. 2003, pp. 81-85.

- [2] J. F. M. Gerrits, J. R. Farserotu, "Wavelet generation circuit for UWB impulse radio applications," Electronics Letters, vol. 38, no. 25, pp. 1737-1738, Dec. 2002.
- [3] H. Kim, D. Park, Y. Joo, "All-digital low-power CMOS pulse generator for UWB system," Electronics Letters, vol. 40, no. 24, pp. 1534-1535, Nov. 2004.
- [4] T. Y. Choi, W. Cho, D. W. Kim, "A simple CMOS delay model for wide applications," IEEE Asia Pacific Conference on Circuits and Systems, 18-21 Nov. 1996, pp. 77-80
- [5] D. A. Hodges, H. G. Jackson, R. A. Saleh, Analysis and Design of Digital Integrated Circuits, New York, McGraw Hill, 2003

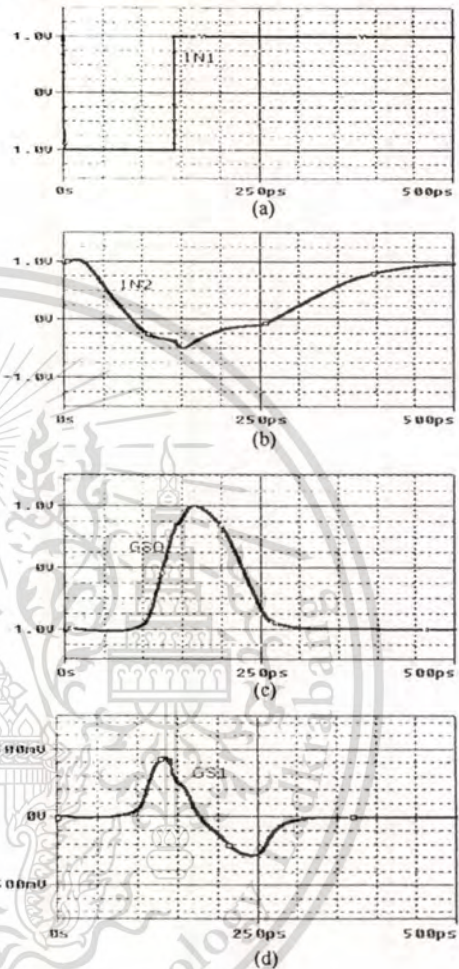
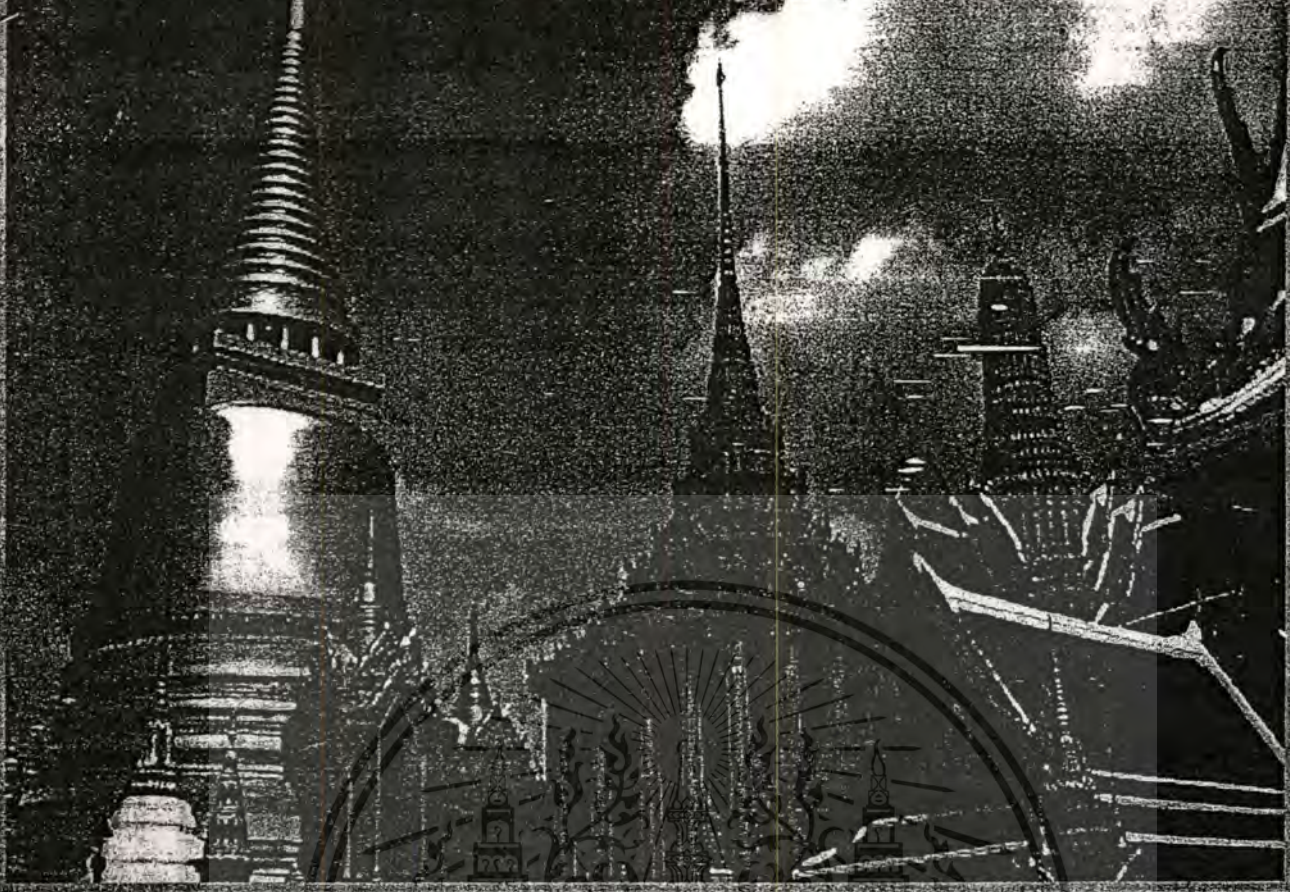


Figure 9. Timing diagram

TABLE I. PERFORMANCES

	Simulation	Calculation
L/W NOT	0.18/0.27 μm	0.18/0.27 μm
L/W NOT2	0.18/2.7 μm	0.18/2.7 μm
C	0.01fF	0.01fF
R	1 Meg	1 Meg
t_{PHL} (IN2)	85.86ps	73.89ps
t_{PLH} (IN2)	231.61ps	177.3ps
PULSE Width	0.14ns	120.0ps
Gaussian Width	229.37ps	323.13ps
Freq. center (monocycle)	4 GHz	3.09 GHz



APCC 2007

2007 Asia-Pacific Conference on Communications

October 18-20, 2007

Bangkok, Thailand

PROCEEDINGS



IEEE COMMUNICATIONS SOCIETY
THAILAND CHAPTER



IEEE CAS Society
Thailand Chapter



IEEE MTT/AP/ED
THAILAND CHAPTER



IEEE
COMMUNICATIONS
SOCIETY

A GHz Analog Multiplier for UWB Communications

R. Hidayat, K. Dejhan, P. Moungnoul¹, Y. Miyanaga²

¹ Faculty of Engineering and Research Center for Communication and Information Technology (ReCCIT) King Mongkut's Institute of Technology Ladkrabang (KMUTL), Bangkok, Thailand

² Division of Media and Network technologies, Graduate School of Information Science and Technology Hokkaido University, Sapporo, Japan

Abstract- A gigahertz wideband analog multiplier is proposed. The multiplier based on the MOS cascade operation circuit. The inputs are in voltage mode and become in current mode after multiplication. The result shows that the multiplier can be applied for UWB communications. The circuit is based on 0.18 μm CMOS technology simulated using HSPICE with level 49

I. INTRODUCTION

Since Ultra WideBand technology has been presented for telecommunication, many papers both in concepts and hardware's have been proposed to develop the technology. FCC (Federation Communication Commission) has proposed 7.5 GHz (3.6-10.1 GHz) bandwidth, and the IERP (Isotropic Effective Radiation Power) regulation for UWB wireless communications [1].

Multiplier is applied in many electronic circuit aspects, such as signal processing, and communications. In the telecommunication, a multiplier is used for the detection process, and/or in the some modulation process. Many researches have proposed on behalf of multiplier circuits. Some techniques based on MOS cascade operation circuit, and work in the voltage mode has been presented [2]. Recently some other techniques are also developed [3][4]. Both voltage and current mode multiplier are currently developed [6]-[8]. However, most of them operate only up to MHz bandwidth.

This paper is to propose a multiplier circuit used for Ultra WideBand communications. It is used for correlation circuit of UWB communication. The proposed circuit in this paper uses MOS cascade concepts [2][9], because it is very simple and applies fewer components. A complex circuit of MOS will decrease the response. The capacitances effect may increase the signal delay and decrease the bandwidth. Therefore, the simpler circuit is more appropriate for UWB that needs wide bandwidth.

The circuit multiplies two voltage inputs, but the output is in the current mode. It is more easily to sum and subtract the signal in the current mode than in the voltage mode. The output can be converted to the voltage using linear I-V converter described in the next section. Using this method, the output voltage has reference to ground. The proposed multiplier has -3dB bandwidth 13 GHz.

The paper is organized as follows. Section I is the introduction that describe the background of the research.

Section II describes about the circuit descriptions. It is about basic concepts of the circuit and its application on the research. The proposed circuit and its results will be explained in section III and IV respectively. Finally, after discussion in section V, the conclusion will appear in section VI.

II. CIRCUIT DESCRIPTIONS

A. Cascade MOS Operation

Considering transistors M1 in Fig. 1 to be in saturation region, and neglecting channel-length modulation, mobility degradation (due to high field and/or short channel) and body effect, the drain current can be expressed as [9].

$$I_D = K(V_{GS} - V_{TH})^2 \tag{1}$$

$$\text{or } \sqrt{I_D} = \sqrt{K}(V_{GS} - V_{TH}) \tag{2}$$

where $K = \frac{1}{2}\mu_0 C_{ox} (W/L)$ is transconductance parameter of transistor, μ_0 is the electron mobility, C_{ox} is the gate oxide capacitance per unit area, W/L is the transistor aspect ratio, V_{GS} is the gate-to-source voltages and V_{TH} is threshold voltage of the MOS transistor, respectively.

Fig 2 shows about a cascade MOS circuit and can work as a multiplier circuit. Based on (2), the drain current through transistor M1 is known as

$$I_D = K(V_{GS} - V_{TH})^2 \tag{3}$$

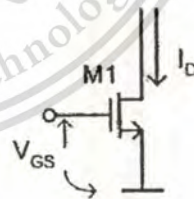


Figure 1. MOS Operation

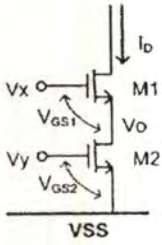


Figure 2. Cascade MOS Operation

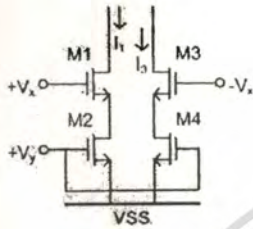


Figure 3. Two Quadrant Multiplier

Multiplication with $\sqrt{I_D}$ on the both side becomes

$$I_D = \sqrt{K} (V_{GS1} - V_{TH}) \sqrt{I_D} \quad (4)$$

Suppose that both transistors operate in saturation region. Since the current I_D is also through M2, then (1) can be substituted to (4). Then

$$I_D = K (V_x - V_0 - V_{TH}) (V_y - V_{TH}) \quad (5)$$

where $V_{GS1} = (V_x - V_0)$, $V_{GS2} = (V_y - VSS)$, and $VSS = 0V$ (ground). The equation in (5) shows that the drain current is the multiplication of two input V_x and V_y with some shifting. A simple form can be written as follows,

$$I_D = K (V_x - a) (V_y - b) \quad (6)$$

where $a = -(V_0 + V_{TH})$ and $b = -V_{TH}$.

B. Two and Four Quadrant Multiplier

Fig. 2 is one quadrant multiplier that is based on the cascade operation. It can be explored to two or four quadrant by adding the opposite voltage of the input. Fig. 3 is about a two quadrants multiplier. Based on (6), the difference between I_1 and I_3 is easily computed as,

$$I_1 - I_3 = 2KV_x (V_y - b) \quad (7)$$

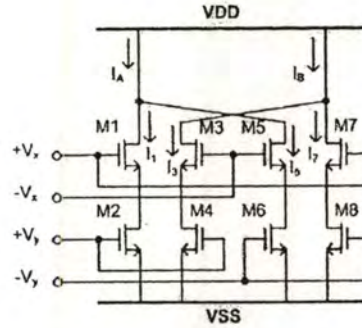


Figure 4. Four Quadrants Multiplier

The four quadrants multiplier is shown in Fig. 4. The multiplication can be gotten by subtraction of the two quadrant multipliers as shown in the figure. Based on (5) and (6), the difference between I_A and I_B can be considered as input multiplication, as follows

$$\begin{aligned} I_A - I_B &= (I_1 - I_3) + (I_5 - I_7) \\ I_A - I_B &= 2KV_x (V_y - b) - 2KV_x (-V_y - b) \\ I_A - I_B &= 4KV_x V_y \end{aligned} \quad (8)$$

It shows in (8) that the current subtraction $I_A - I_B$ is the simple multiplication of the input voltages V_x and V_y .

III. THE PROPOSED CIRCUITS

The principle of operation of the proposed multiplier is based on Fig. 4 that has equation in (8). This is a voltage to current (V-I) multiplier. The proposed analog multiplier circuit is shown in Fig. 5.

To get and subtract the currents I_A and I_B , three current mirrors are used. The MOS M9 M13 pair in Fig. 5 is the current mirror for I_A , while the M10 M11 pair is for I_B . The drain current of MOS formed in (1), or $I_B = f(V_{GS M10})$. Based on (1), the inverse function $V_{GS M10} = f^{-1}(I_B)$ can be written as

$$V_{GS M10} = V_{TH} + \sqrt{\frac{I_B}{K}} \quad (9)$$

The same equation is implemented also for M11. Since M10 and M11 are identical, and $V_{GS M10} = V_{GS M11}$, then

$$\begin{aligned} I_{10} &= I_{11} = I_B \\ I_9 &= I_{13} = I_A \end{aligned} \quad (10)$$

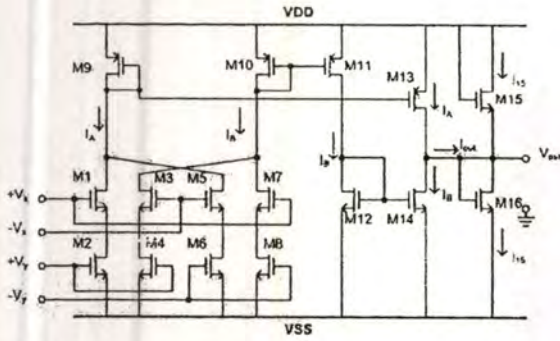


Figure 5. The Proposed Circuit

The M12 M14 pair is given to subtract between I_A and I_B . I-V conversion can be reached using M15 and M16 in Fig. 5. Based on (1), the drain currents respectively are

$$I_{15} = K(V_{DD} - V_{out} - V_{TH15})^2$$

$$I_{16} = K(V_{out} - V_{SS} - V_{TH16})^2$$

Since $I_{Out} = I_{16} - I_{15}$, $V_{SS} = -V_{DD}$ and $V_{TH15} = V_{TH16} = V_{TH}$, then the output voltage can be written as

$$V_{out} = \frac{I_{out}}{4K(V_{DD} - V_{TH})} \quad (10)$$

Substitution (8) into (10) concludes that the output voltage of the proposed multiplier circuit shown in Fig. 5 is the multiplication of the both input voltages, and can be formed as

$$V_{out} = \frac{V_x V_y}{(V_{DD} - V_{TH})} \quad (11)$$

IV. SIMULATION RESULTS

The performances of the proposed analog multiplier circuit are simulated using HSPICE with level 49 model of $0.18\mu\text{m}$ MOS parameter. The voltage supply are $V_{DD} = -V_{SS} = 1\text{V}$.

The complete circuit of the current multiplier is viewed in Fig. 5, and the simulation use $0.18\mu\text{m}$ CMOS with $L/W = 0.18/0.18\mu\text{m}$. The simulation result of the DC characteristic shown in Fig. 6. Input of V_x and V_y are from -250mV to $+250\text{mV}$. As shown in Fig. 6, by the voltage supply of $V_{DD} = -V_{SS} = 1\text{V}$, the result is linear for the range of the voltages input sweep of -250mV to $+250\text{mV}$. Fig. 7 shows the frequency response of the multiplier in Fig. 5. The graph is about V_{out}/V_x in dB. The graphics shows -3dB response of the multiplier is very high, at 13GHz . It is convenient for the UWB signal communications that need 10.5GHz maximum. Table 1 shows the specifications of the circuit and the result.

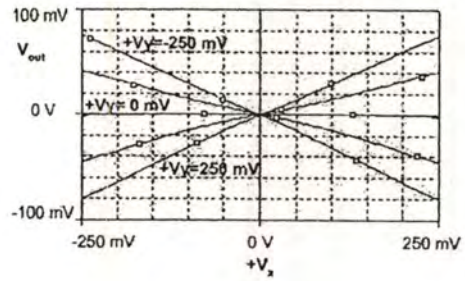


Figure 6. DC Characteristics

TABLE I
CIRCUIT SPECIFICATIONS

dB in 1 GHz or less	-10.7 dB
Freq in -3 dB (13.7 dB)	13.0 GHz
Power Supply	± 1 Volt
Input Amplitude (V_x)	± 0.25 V
Input V_y	± 0.25 V

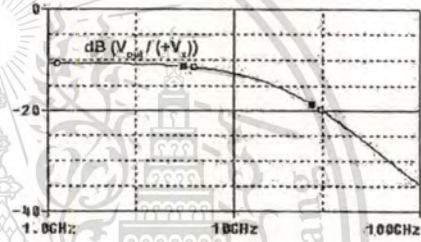


Figure 7. Frequency Response

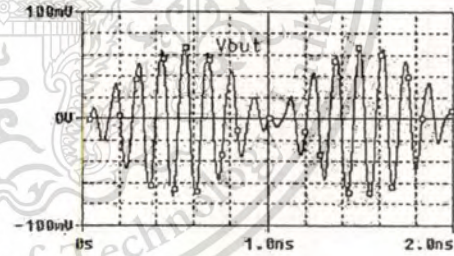


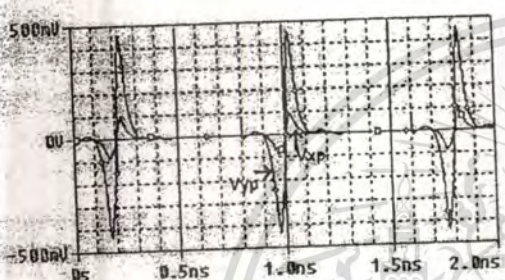
Figure 8. Transient simulation for 2 sine waves

TABLE II
INPUT SIGNAL OF FIG. 8.

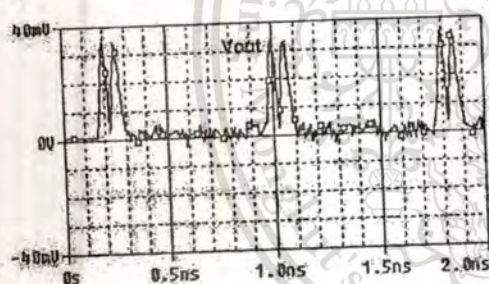
Supply voltage	± 1 Volt
Input Amplitude V_x	± 0.25 V
Frequency V_x	500 MHz
Input Amplitude V_y	± 0.25 V
Frequency V_y	8 GHz

Fig. 8 shows the transient analysis of the multiplier in Fig 5. The amplitude of input voltages V_x and V_y are 0.25 V. The frequency of V_x and V_y are 500 MHz and 8 GHz respectively. Table 2 shows the specifications of the signals.

Transient analysis for Ultra wideband impulse radio is done by two monocycle pulses with same width of 0.2 ns with different amplitudes. This is to consider that in the real correlator, the received signal is weaker than the template signal. The pulse with small amplitude is applied to gates of the lower transistors, while the large pulse is to the upper transistors. The two pulses of 0.2ns are generated by using a monocycle pulse generation circuit that also based on 0.18 μ m CMOS technology. Fig. 9 shows the transient simulation result. Fig. 9 (a) is the two input pulses and (b) the output of the multiplier. Fig. 9 shows that the correct output is obtained at the output of the multiplier. It shows that the multiplier has sufficient bandwidth and is able to work with the sub-nano second pulse inputs.



(a) Inputs



(b) Output Result

Figure 9. Transient simulation for UWB inputs

V. DISCUSSION

[4][5][6] are voltage mode multipliers that relatively have complex circuits. [3][7] are current mode. [4] is relatively complex, and [7] is relatively simple, but both have the frequency response relatively low, in MHz. [8] proposed an analog multiplier in voltage mode for UWB. However, the circuit is still more complex than this proposed circuit. The

voltage to current conversion of this proposed multiplier will subtract the signals in the current mode that is easier to be implemented. The current mode output increases the operation of bandwidth. Without adding inductors as in [8], this circuit has 13 GHz Bandwidth. In addition, by converting back to the voltage mode, the output signal has reference to ground.

VI. CONCLUSION

An ultra high frequency analog multiplier is proposed. The multiplier based on the MOS cascade operation circuit. The inputs are in voltage mode and become in current mode after multiplication. The simulation has shown that the multiplier has a flat frequency response up to 13GHz and can be applied for UWB communications. The circuit is based on 0.18 μ m CMOS technology simulated using HSPICE with level 49 and operates in $\pm 1V$.

ACKNOWLEDGMENT

The authors would like to thank to the AUN/SEED-Net project that is mainly supported by the Japan International Cooperation Agency (JICA) for providing the Doctoral Degree Sandwich Programs scholarship under Collaborative Research between Research Center for Communication and Information Technology (ReCCIT), King Mongkut's Institute of Technology Ladkrabang (KMUTL) and the Division of Media and Network technologies, Graduate School of Information Science and Technology, Hokkaido University, Japan.

REFERENCES

- [1] FCC 04-48 "First Report and Order in the Matter of Revision of Part 15 of the Commission's Rules Regarding Ultra-wideband Transmission Systems." Feb.14, 2002.
- [2] H.Gunhee, S. Sanchez-. "MOS transconductance multipliers: a tutorial", IEEE Transactions on Circuits and Systems II: Analog and Digital Signal Processing, vol. 45, Issue 12, pp. 1550-1563, Dec. 1998.
- [3] M. Kumngorn, K. Dejhan, "Versatile dual-mode class-AB four-quadrant analog multiplier," International Journal of Signal Processing, vol. 2, No.3, pp. 214-221, Dec. 2005.
- [4] H. J. Song, C. K. Kim, "An MOS four-quadrant analog multiplier using simple two-input squaring circuits with source followers", IEEE Journal of Solid-State Circuits, vol. 25, Issue 3, pp. 841 - 848, Jun 1990.
- [5] B. Boonchu, W. Surakamponporn, "A new NMOS four-quadrant analog multiplier", IEEE International Symposium on Circuits and Systems, ISCAS, 23-26, vol. 2, pp. 1004 - 1007, May 2005.
- [6] S. Szczepanski, S. Koziel, "1.2V low-power four-quadrant CMOS transconductance multiplier operating in saturation region", Proc. of Int. Symp. on Circuits and Systems, vol. 1, pp. 1-1016-19, May 2004
- [7] R.J. Wiegink, "A CMOS four-quadrant analog current multiplier", IEEE Int. Symp. on Circuits and Systems, vol. 4, pp. 2244-2247, June 1991.
- [8] L. Zhou, Y. P. Xu, F. Lin, "A gigahertz wideband CMOS multiplier for UWB transceiver", IEEE Int. Symp. on Circuits and Systems, vol. 523-26, pp. 5087 - 5090, May 2005.
- [9] B. Razavi, "Design of Analog Integrated Circuits", New York: McGraw-Hill, 2001, pp. 126-129.

JICT
2007

Proceedings

Joint International Conference on Information Communication Technology



19-22 December 2007

Donchan Palace Hotel, Vientiane, Lao PDR



JICT
2007

JICT
2007

JICT
2007

JICT
2007

JICT
2007

JICT
2007

This material is reserved for educational use only, not allowed for commercial use.

Forbidden to modify the content, and cite the document when use.

BER ANALYSIS OF IR-UWB COMMUNICATION OVER MODIFIED S-V CHANNEL MODEL

Resanuri Hidayat, Kobchai Dejhan, Phichet Moungnoul¹, Yoshikasu Miyanaga²

¹ Faculty of Engineering and Research Center for Communication and Information Technology (ReCCIT) King Mongkut's Institute of Technology Ladkrabang (KMITL), Bangkok, Thailand

² Division of Media and Network technologies, Graduate School of Information Science and Technology Hokkaido University, Sapporo, Japan
{risanuri, kobchai, phichet}@telecom.kmitl.ac.th, miya@ist.hokudai.ac.jp

ABSTRACT

This paper proposes BER of the Impulse Radio Ultra Wideband pulse communication over modified S-V channel model. The pulse is generated from circuit with HSPICE level 49. The channel model is using generated of modified S-V model presented in [4]. Binary Pulse Amplitude Modulation is applied, and BER is measured over several of bits per packet. The result shows that monocycle pulse over LOS channel gives the best bit rates. The triplet pulse has rougher bit and has bit rates more quickly in NLOS channel.

2. UWB PULSE

2.1. Gaussian Pulse

Some references have represented several kind formulas of Gaussian pulse [6] [7] [8]. A monocycle pulse is the first derivative of Gaussian pulse. The Gaussian pulse has formula as described in (1), while the monocycle as in (2).

$$x(t) = A_1 \cdot e^{-2\left(\frac{\pi t}{T_c}\right)^2} \quad (1)$$

$$x^{(1)}(t) = \frac{dx(t)}{dt} = A_2 \cdot t \cdot e^{-2\left(\frac{\pi t}{T_c}\right)^2} \quad (2)$$

$$f_c = \frac{1}{T_c} \quad (3)$$

1. INTRODUCTION

Since Ultra WideBand technology has been presented for telecommunication, many papers both in concepts and hardware's have been proposed to develop the technology. FCC (Federation Communication Commission) has proposed 7.5 GHz (3.6-10.1 GHz) bandwidth, and the IERP (Isotropic Effective Radiation Power) regulation for UWB wireless communications [1].

This paper analyzes BER of Ultra Wideband pulse communication over channel model by simulation. The UWB pulse in this research is an Impulse Radio UWB generated from circuit using HSPICE level 49 models. The channel model is introduced and modified from S-V model [2] [3] [4]. Data sent by the transceiver is converted to UWB pulse using Binary Pulse Amplitude Modulation (BPAM) [5] and then received by the receiver. In the receiver the pulse is then converted to be data again. Comparison between data sent by transmitter and data in receiver give the BER value. The data is sent in packet, and this paper will report about the number of bit per packet that effectively capable to be transmit over the channel without any failure.

The paper is organized as follows. Section I is the introduction that describe the background of the research. Section II describes about UWB pulse principles. It is about basic concepts of the UWB and its generation circuit. The channel model and the simulation method will be explained in section III and IV respectively. Finally, after the results in section V, the conclusion will appear in section VI.

where T_c is the width of the pulse, A_1 and A_2 are amplitudes, and T_c is the width of the pulse. Figure 1 shows the Gaussian pulse waveform and monocycle of the pulse.

The Federal Communications Commission (FCC) recently approved the deployment of UWB on an unlicensed basis in the 3.1-10.6 GHz band subject to a modified version of Part 15.209 rules. The essence of this ruling is to limit the power spectral density (PSD) measured in a 1-MHz bandwidth at the output of an isotropic transmit antenna to that shown in Fig. 2. [1].

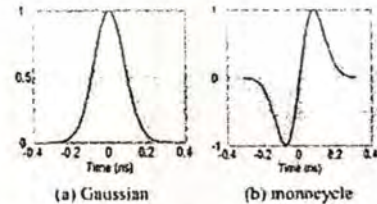


Figure 1. Gaussian pulse waveform

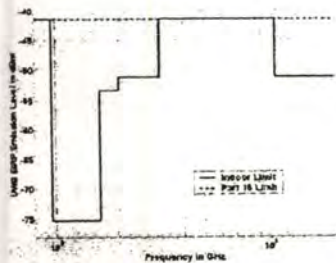


Figure 2. UWB spectral mask and FCC Part 15 limits.

2.2. Generated UWB Pulse

The Gaussian pulse generation used in this paper is introduced. The circuit is shown in Fig. 3. All circuits are simulated using HSPICE level 49 of 0.18 μ m CMOS parameter from mosis [9]. The input is a step signal or pulse that the width is in such a way that the Gaussian pulse can be performed. Fig. 4 shows the time diagram of Gaussian monocycle pulse at the V_{out1} node that conducts to (2). Fig. 5 shows the normalized Power Spectral Density (PSD) of the derivative of the monocycle pulse from the circuit. When a pulse is transmitted, due to the derivative characteristics of the antenna, the output of the transmitter antenna can be modeled by the first derivative of the pulse [10]. The derivative can be achieved by the basics of differential calculus

$$x^{(1)}(t) = \lim_{dt \rightarrow 0} \frac{x(t+dt) - x(t)}{dt} \quad (4)$$

PSD of the deterministic power signal, $w(t)$, is

$$P(f) = \lim_{T \rightarrow \infty} \left(\frac{|X(f)|^2}{T} \right) \quad (5)$$

where T is the pulse spacing interval. $X(f)$ is the Fourier transform of the pulse, i.e. $x(t)$. $P(f)$ has units of watts per hertz. When $X(f)$ is attained, the peak emission frequency, i.e. fM, can be found as the frequency at which the maximum value of $|X(f)|$. The normalized PSD is used due to comply the FCC spectral mask of the pulse that is transmitted by antenna [1][10][11]. The normalized PSD can be defined as follows

$$|P(f)| = \frac{|X(f)|^2}{|X(f_M)|^2} \quad (6)$$

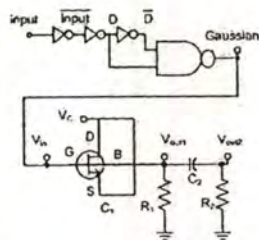


Figure 3. Monocycle Circuit

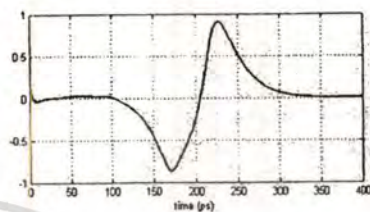


Figure 4. The generated Gaussian monocycle pulse

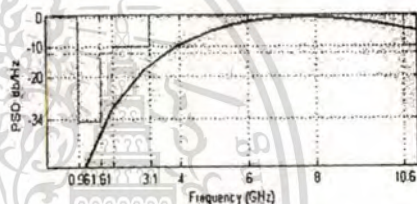


Figure 5. PSD of the derivative monocycle pulse in Fig. 4

Fig. 6 shows the improvement of the Gaussian monocycle pulse generation. The second monocycle pulse is generated after being delayed by two NOT's. Then both monocycles are connected to generate UWB pulse 3th derivative of the Gaussian pulse shape. The time diagram of node Gaussian02 is the same as in Fig. 17 with some delays. Fig.7 shows the time diagram of Gaussian monocycle pulse at the V_{out} node. The figure shows that the graphic has four peaks of signal which conducts as the triplet pulse or the 3th derivative of Gaussian pulse. Fig. 8 shows the normalized Power Spectral Density (PSD) of the derivative of the UWB pulse from the circuit in Fig. 6, using (4). As shown in Fig. 8 the normalized PSD complies the FCC spectral mask.

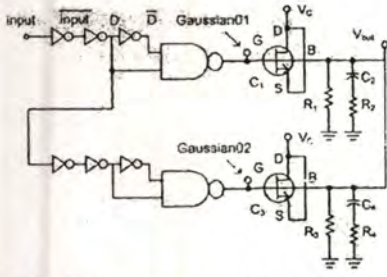


Figure 6. The improvement of the proposed circuit.

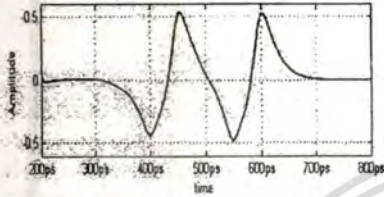


Figure 7. The time diagram of Fig. 6.

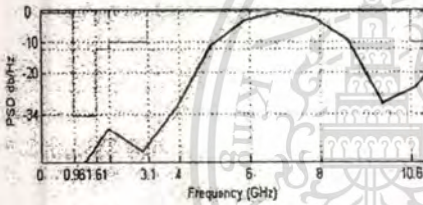


Figure 8. The normalized PSD of the derivative pulse Fig. 7.

3. CHANNEL MODEL

Nowadays, there are several channel models used for analyzing wireless communication system that is designed suitable for specific situation such as indoor and outdoor environment. For the time-of-arrival statistics, the model of Saleh-Valenzuela (S-V) is used as the channel measurements showed multipaths arriving in clusters [2]. This is partly a result of the very fine resolution that ultra-wideband waveforms provide, as multipath results from reflections off walls, ceilings, furniture, people, and other objects that may be present within a room. Since UWB waveforms can be up to 7.5 GHz wide, for example, paths separated by more than about 133 ps (equivalent to 4 cm pathlength difference) can be individually resolved at the receiver [3]. The realistic channel for IEEE 802.15 study group 3a has been developed by Saleh-Valenzuela (S-V model) and proposed for the real indoor channel model, where the

clusters and rays are multi-path components [4]. This multi-path channel can be expressed as

$$h(t) = \sum_{l=0}^L \sum_{k=0}^K \alpha_{k,l} \delta(t - T_l - \tau_{k,l}) \quad (7)$$

where $\alpha_{k,l}$ is the multipath gain coefficient, T_l is the delay of the l^{th} cluster, and $\tau_{k,l}$ is the delay of the k^{th} multipath component relative to the l^{th} cluster arrival time (T_l).

As suggested in [4], $\alpha_{k,l} = p_{k,l} \beta_{k,l}$ is adopted, where $p_{k,l}$ is equally likely to take on the values of ± 1 , and $\beta_{k,l}$ is the lognormal fading term, due to the simplicity of the real channel coefficients, and to avoid the ambiguity of phase for an UWB waveform.

The proposed channel model uses similar definitions as previously described for the S-V model, and are repeated here for completeness. T_l is the arrival time of the first path of the l -th cluster; $\tau_{k,l}$ is the delay of the k -th path within the l -th cluster relative to the first path arrival time, T_l ; Λ is cluster arrival rate; and λ = ray arrival rate, i.e., the arrival rate of path within each cluster.

So, $\tau_{0l} = T_l$. The distribution of cluster arrival time and the ray arrival time are given by

$$\begin{aligned} p(T_l | T_{l-1}) &= \Lambda \exp[-\Lambda(T_l - T_{l-1})], \quad l > 0 \\ p(\tau_{k,l} | \tau_{(k-1),l}) &= \lambda \exp[-\lambda(\tau_{k,l} - \tau_{(k-1),l})], \quad k > 0 \end{aligned} \quad (8)$$

The channel coefficients are defined as follows:

$$\alpha_{k,l} = p_{k,l} \beta_{k,l}$$

$\beta_{k,l}$ is obtained by this expression

$$20 \log_{10}(\beta_{k,l}) \propto \text{Normal}(\mu_{k,l}, \sigma^2)$$

$$\text{or } |\beta_{k,l}| = 10^{n/20}$$

where

$$n \propto \text{Normal}(\mu_l, \sigma^2) \quad (9)$$

$$E[\beta_{k,l}^2] = \Omega_0 e^{-T_l/\Gamma} e^{-\tau_{k,l}/\gamma}$$

where T_l is the excess delay of bin l and Ω_0 is the mean power of the first path of the first cluster, and $p_{k,l}$ is ± 1 . The μ_l is given by

$$\mu_l = \frac{10 \ln(\Omega_0) - 10T_l/\Gamma - 10\tau_{k,l}/\gamma - \sigma^2 \ln(10)}{\ln(10)} \quad (10)$$

4. SIMULATION METHOD

Fig. 9 shows a block diagram of the transmitter-receiver communication. Transmitter sends Data bit packet by packet, and Receiver read the packet. Transmitter converts the bits in packet to be UWB pulses, and then send to the antenna to be transmitted. In Fig. 9, $u_r(t)$ is the received signal at time instance t . The signal then through LNA (Low Noise Amplifier) and becomes $u_f(t)$. Then it is demodulated using template pulse.

The UWB pulse is the generated monocycle or triplet pulse described previously. The classic binary pulse amplitude modulation (BPAM) is implemented in Pulse Generation block in Fig. 9. It can be presented using e.g. two antipodal Gaussian pulses. The transmitted binary baseband pulse amplitude modulated information signal (t) can be presented as [5]

$$x(t) = d_j \cdot w_r(t) \quad (11)$$

where $w_r(t)$ represents the UBW pulse waveform, j represents the bit transmitted that $j=1$ then $d_j = 1$ and $j='0'$ then $d_j = -1$.

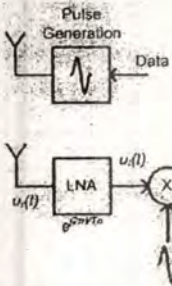


Figure 9. Tx-Rx Communication Block Diagram

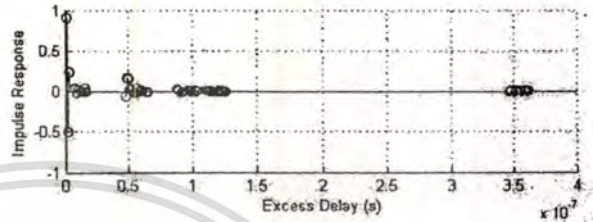
A channel happens between transceiver and receiver. In this paper, an UWB channel model derived from the Saleh-Valenuela model with one slight modification is proposed. This is the proposed model that fits the measurements taken in the home environment for both LOS and NLOS [4]. There are 5 key parameters that define the model: Λ = cluster arrival rate; λ = ray arrival rate, i.e., the arrival rate of path within each cluster; Γ = cluster decay factor; γ = ray decay factor; and σ = standard deviation of lognormal fading term (dB).

Table 1. Channel model parameters.

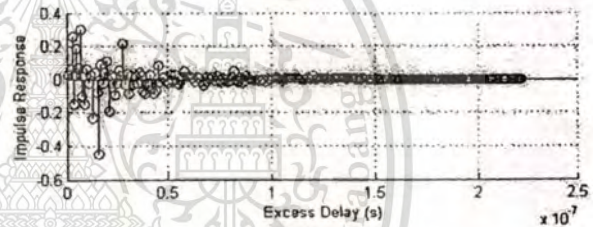
Model Parameters	LOS	NLOS
Λ	1/60	1/11
λ	1/0.5	1/0.35
Γ	16	16
γ	1.6	8.5
σ	4.8	4.8

This paper uses one of channel realization generated from S-V model using the parameters as in Table 1 from [4] the BER analysis. The channel is shown in Fig 10.

In an ideal environment, the received pulse shape is the second derivative of the signal transmitted due to differentiator effect in transmitter and receiver antennas. However, the amplitude of correlation result between the first and the third derivatives of the Gaussian pulse is 80% of the autocorrelation of the received waveform [5]. This means that using the transmitted waveform as the template reduces the performance of the correlator by less than 1 dB. Therefore, the receiver still can use the same template waveform as the transmitter has to demodulate the signals.



(a) LOS



(b) NLOS

Figure 10. The generated channel model

5. RESULTS

The implementation is based on Block Diagram in Fig. 9. Transceiver converts the bits in packet to be UWB pulses. Both monocycle and triplet is implemented. Also the channel model, both LOS and NLOS model is implemented. There are many channel model can be generated using model parameters in Table 1 to implement (7) until (10). We used one of them as shown in Fig. 10. Transceiver sends Data bit packet by packet. BPAM is implemented for modulation. There are 10^4 bits sent in the research. Fig. 11 shows the result of the BER of the monocycle and triplet pulses through the LOS and NLOS channel model. Fig. 11 (a) shows data sent using monocycle pulse over LOS channel model. Until 200 bit

per packet, there is no BER. Then BER relatively increase proportionally with the bit per packet increasing. However, there is no BER using triplet pulse over LOS channel model even until maximum bits per packet as shown in Fig. 11 (b). In Fig. 11 (c), data sent using monocycle pulse over NLOS channel model. Here, data is without error in 30 bit per packet, but the BER increase after that. In Fig. 11 (d), data sent using triplet pulse over NLOS channel model, data has BER increase after 40 bit per packet is sent.

Table 2. Bit rates results.

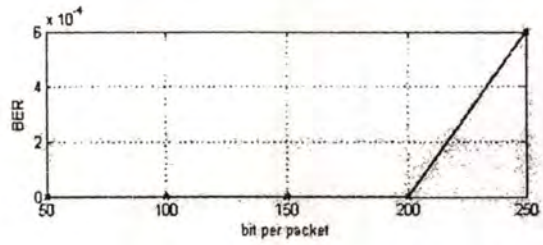
Model	Bit rates
LOS monocycle	4.0 Gbps
LOS triplet	2.5 GBps
NLOS monocycle	300 Mbps
NLOS triplet	400 Mbps

Table 3. BER performance in AWGN channels.

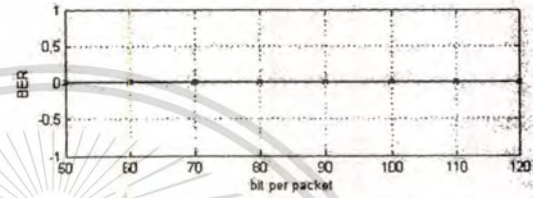
SNR	BER			
	LOS mono	LOS triplet	NLOS mono	NLOS triplet
1	5.19e-2	1.74e-2	9.41e-2	1.05e-1
2	4.53e-2	1.30e-2	6.99e-2	9.57e-2
3	4.05e-2	6.16e-3	5.58e-2	7.34e-2
4	3.28e-2	5.25e-3	4.72e-2	5.11e-2
5	2.40e-2	3.16e-3	2.81e-2	3.39e-2
6	1.97e-2	1.50e-3	2.38e-2	1.91e-2
7	1.34e-2	4.16e-4	1.87e-2	1.52e-2
8	8.82e-3	0.00e-0	1.13e-2	8.98e-3
9	6.40e-3	8.33e-5	1.01e-2	6.64e-3
10	4.45e-3	0.00	7.42e-3	3.51e-3
11	1.64e-3	-	5.31e-3	2.73e-3
12	3.90e-4	-	3.59e-3	1.17e-3
13	7.81e-5	-	2.57e-3	6.25e-4
14	0.00	-	2.42e-3	3.12e-4
15	0.00	-	1.40e-3	2.34e-4
16	0.00	-	1.01e-3	3.12e-4
17	0.00	-	1.01e-3	0.00
18	0.00	-	3.12e-4	0.00
19	0.00	-	4.68e-4	0.00
20	0.00	-	3.12e-4	0.00

From the model in Fig. 10 (a), suppose that the LOS model has no effect after around 0.5×10^{-7} second, and data is periodically sent at this time. The number of pulse maximum is $0.5 \times 10^{-7} / (2 \times 10^{-12}) = 250$ for monocycle. Since data is still correct for 200 bit per packet, the bit rate becomes $200 / (0.5 \times 10^{-7}) = 4$ Gbps for monocycle, Fig. 11(a). For the triplet pulse, this is excellent as shown in Fig. 11(b). The bit rate becomes $1/\text{pulsewidth}$, i.e. 2.5 Gbps. From the model in Fig. 10 (b), suppose that the NLOS model has minimum effect after around 1×10^{-7} second; since data is still correct for 30 bit per packet for monocycle, the bit rate becomes $30 / (1 \times 10^{-7}) = 300$ Mbps for monocycle, Fig. 11 (c), and $40 / (1 \times 10^{-7}) = 400$ Mbps

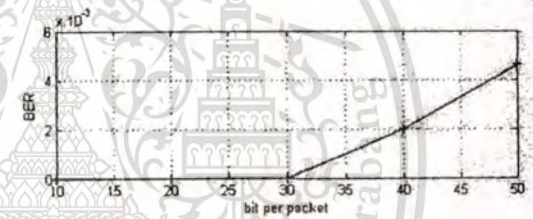
for triplet pulse in Fig. 11 (d). By looking at the UWB standard reference and compare to the others, it seems that this communication model is preferable. Table 2 shows the bit rates.



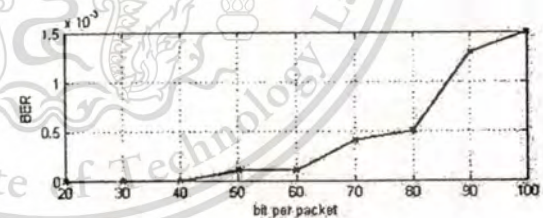
(a) UWB monocycle pulse over LOS channel



(b) UWB triplet pulse over LOS channel



(c) UWB monocycle pulse over NLOS channel



(d) UWB triplet pulse over NLOS channel

Figure 11. BER of the UWB pulses through the LOS and NLOS channel models

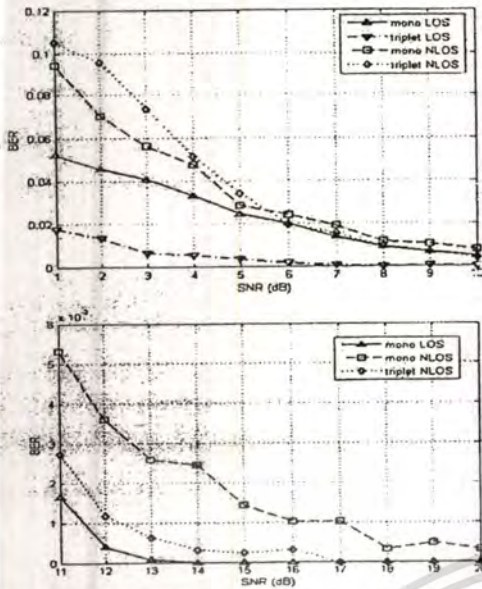


Figure 12. BER performances over AWGN channels

Fig. 12 shows the BER performance of the UWB pulses through the LOS and NLOS channel models with AWGN impact. Based on Fig. 11(a)-(d), the monocycle pulse over LOS channel is 128 bits per packet. The triplet over LOS is 64 bits per packet, monocycle over NLOS is 32 bits per packet, and triplet over NLOS is 32 bits per packet, respectively. All BER are good start from more than 8 dB SNR unless triplet LOS is good from 3 dB SNR. The triplet pulse is more robust than monocycle in the case of AWGN impact. Table 3 shows the BER performance of the pulse in AWGN channels.

6. CONCLUSION

The BER analysis of the Impulse Radio Ultra Wideband pulse communication over modified S-V channel model is presented. The pulse is generated from circuit with HSPICE CMOS model level 49. The channel model is using generated of modified S-V model. Binary Pulse Amplitude Modulation is applied, and BER is measured over several of bits per packet. The result shows that monocycle pulse over LOS channel gives the best bit rates. The triplet pulse is more robust and has bit rates more quickly in NLOS channel.

REFERENCES

- [1] FCC 04-48 "First Report and Order in the Matter of Revision of Part 15 of the Commission's Rules Regarding Ultra-wideband Transmission Systems." Feb.14, 2002.
- [2] Saleh A. M., Valenzuela R. A., "A statistical model for indoor multipath propagation," *IEEE Journal on Selected Areas In Communications*, vol. SAC-5, no. 2, pp. 128-137, Feb. 1987.

- [3] Molisch, A.F.; Foerster, J.R.; Pendergrass, M., "Channel models for Ultra wideband personal area networks", *IEEE Wireless Communications*, vol. 10, Issue 6, pp. 14-21, Dec. 2003
- [4] Foerster J., Li Q., "UWB Channel Modeling Contribution from Intel," submitted to IEEE JSAC 2002.
- [5] Oppermann I., Hamalainen M., and Linatti J., *UWB Theory and Applications*, John Wiley & Sons Ltd, West Sussex, 2004
- [6] X. Chen, and S. Kiaei, "Monocycle shapes for ultra wideband system", *Proc. IEEE International Symposium on Circuits and Systems*, vol. 1, pp. 597-600, May 2002.
- [7] H. Kim, D. Park, and Y. Joo, "Design of CMOS Scholtz's monocycle pulse generator", *Proc. IEEE Conference on Ultra Wideband Systems and Technologies*, pp. 81-85, Nov. 2003.
- [8] Azakkour, M. Regis, F. Pourchet, and G. Alquie, "A new integrated monocycle generator and transmitter for ultra-wideband (UWB) communications", *Proc. IEEE Symposium on Radio Frequency integrated Circuits*, pp. 79-82, June 2005.
- [9] <http://www.mosis.org/Technical/Testdata/tsmc-018-prm.html>
- [10] G. Breed, "A Summary of FCC Rules for Ultra Wideband Communications", <http://www.highfrequencyelectronics.com/Archives/Jan05/>
- [11] S. Hongsan, P. Orlik, A.M. Haimovich, L. J. Jr. Cimini, and Z. Jinyun, "On the Spectral and Power Requirements for Ultra-Wideband Transmission", *Proc. IEEE on Communications vol. 1*, pp. 738 - 742, May 2003.

INTERNATIONAL SYMPOSIUM ON COMMUNICATIONS AND INFORMATION TECHNOLOGIES 2008



COVER

MESSAGES

KEYNOTES

SESSIONS

Copyrighted 2008, National University of Laos, All Rights Reserved.

decor



decor





Session: D3-CL Analog Circuits, Filters and Data Conversion (2)
Date: Thursday, 23 Oct 2008
Time: 9:00-10:20



CMOS Adiabatic Driver with Bootstrap Technique for Driving Large Capacitive Loads

Jos'e C.Garc'ra (Institute for Applied Microelectronics, University of Las Palmas de Gran Canaria, Spain);
Juan A. Montiel-Nelson (Institute for Applied Microelectronics, University of Las Palmas de Gran Canaria, Spain);
Saeid Nooshabadi (Department of Information and Communication Gwangju Inst. of Science and Technology (GIST) Republic of Korea, Korea)



A GHz Simple CMOS Squarer Circuit

Risanuri Hidayat (Faculty of Engineering, KMITL,Thailand);
Kobchai Dejhan (Faculty of Engineering, KMITL,Thailand);
Phichet Moungnoul (Faculty of Engineering, KMITL,Thailand);
Yoshikazu Miyanaga (Division of Media and Network technologies, Hokkaido University, Japan)



Electronically Tunable Voltage-Mode All-Pass Filter Using Simple CMOS OTAs

Montree Kumngern (Faculty of Engineering, KMITL,Thailand);
Jirasak Chanwutitum (Instrumentation and Electronics Engineering Department, Faculty of Engineering, King Mongkut's University of Technology North Bangkok, Thailand);
Kobchai Dejhan (Faculty of Engineering, KMITL,Thailand)



Novel High-Speed Architecture for 32-Bit Binary Coded Decimal (BCD) Multiplier

Sreehari Veeramachaneni M.B. Srinivas (Centre for VLSI and Embedded System Technologies International Institute of Information Technology-Hyderabad Hyderabad, 500032, India.)



Multi-Module of X-Ray Array Detectors

Woranut Iampa (Faculty of Engineering, KMITL,Thailand);
Chousak Jantaco (Faculty of Engineering, KMITL,Thailand);
Chuchart Pintavirooj (Faculty of Engineering, KMITL,Thailand);
Manas Sangworasil (Faculty of Engineering, KMITL,Thailand)

SESSIONS

[HOME](#)

ISCIT 2008 , 21-23 October
Donchan Palace Hotel, Vientiane, Lao PDR.

line decor



line decor

A GHz Simple CMOS Squarer Circuit

Risanuri Hidayat, Kobchai Dejhan, Phichet Moungnoul, Yoshikazu Miyanaga*
Faculty of Engineering and Research Center for Communication and Information Technology,
King Mongkut's Institute of Technology Ladkrabang, Bangkok 10520, Thailand

*Division of Media and Network technologies, Graduate School of Information Science and Technology,
Hokkaido University, Sapporo, Japan

Abstract- A simple CMOS squarer circuit is proposed. The circuit has a Giga Hertz frequency response that has advantages to be used in communication systems. The proposed circuit focuses on the extension to ultra wide bandwidth. The circuit is based on 0.18 μm CMOS technology simulated using PSPICE level 7. The circuit has wide dynamic range, GHz-bandwidth response and low power consumption. The proposed circuit has been simulated with SPICE and achieved -3dB bandwidth of 10.96GHz. The power consumption is about 86.5 μW with a $\pm 1\text{V}$ power supply voltage. Simulation result shows that the proposed squarer can accommodate the whole UWB bandwidth.

I. INTRODUCTION

Recently, the low voltage analog circuit design has been widely increasing. The CMOS technology is one good choice for this requirement and is interesting for analog circuit designing in the past two decades. There are many advantages, such as, low cost technology, small size, easily scaled and high packing density, low power consumption, and capable to operate under low supply voltage while the performance still maintains. Therefore, the analog circuit designs with CMOS technology can be presented in many literatures [1]-[4].

The squarer circuit is widely used in analog signal processing applications such as multiplier, modulating, frequency doubling, frequency dividing and adaptive filtering. Presently, there is growing interest in current-mode circuit [1]-[5] for high-frequency performance and the trend to lower supply voltage which will reduce the dynamic range of voltage-mode circuits.

Nowadays, the squarer circuit has been implemented by various techniques. One indirect method, by common the analog multiplier to obtain the squaring output. Although this is an easy way and can apply to proposed multiplier circuit, the large numbers of the transistors are required.

This paper proposes low-voltage squarer circuit that uses the simple differential amplifier without any passive component. The circuit operates as source follower and all MOS transistors are in saturation region. The simulation of the proposed circuit by using PSPICE level 7 is based on 0.18 μm CMOS technology is carried out with MOSIS transistor model. This circuit is very suitable for low-voltage application and IC implementation. The GHz-bandwidth response and low power consumption is very suitable for the UWB applications.

II. CIRCUIT DESCRIPTION

Considering the circuit in Fig. 1, while both transistor work in saturation region is expressed as,

$$\begin{aligned} I_1 &= \frac{K_1}{2} (V_{GS1} - V_{TH1})^2 \\ I_2 &= \frac{K_2}{2} (V_{GS2} - V_{TH2})^2 \end{aligned} \quad (1)$$

For $V_{GS} > V_{TH}$, $V_{DS} \geq V_{GS} - V_{TH}$ where $K = \mu_0 C_{ox} (W/L)$ is the transconductance parameter of transistor, μ_0 is the electron mobility, C_{ox} is the gate oxide capacitance per unit area, W/L is the transistor aspect ratio, V_{GS} is the gate-to-source voltage, V_{DS} is the drain-to-source voltage and V_{TH} is threshold voltage of the MOS transistor. If the transistors are homogeneous, as $K_1 = K_2 = K$ and $V_{TH1} = V_{TH2} = V_{TH}$, then the expression can be obtained as

$$I_1 + I_2 = \frac{K}{2} \left[(V_{in} - V_A - V_{TH})^2 + (-V_{in} - V_A - V_{TH})^2 \right] \quad (2)$$

Then the summation can be written as,

$$I_{sum} = KV_{in}^2 + K(V_A + V_{TH})^2 \quad (3)$$

where $I_{sum} = I_1 + I_2$. Since I_{sum} is also through M3, then it can be written as,

$$I_{sum} = K(V_A - V_{SS} - V_{TH})^2 \quad (4)$$

$$V_A = V_{TH} + V_{SS} + \sqrt{\frac{I_{sum}}{K}}$$

Substitution (4) into (3) get,

$$\begin{aligned} I_{sum} &= KV_{in}^2 + K \left(\sqrt{\frac{I_{sum}}{K}} + V_{SS} + 2V_{TH} \right)^2 \\ I_{sum} &= \frac{K(V_{in}^4 + 2V_{in}^2(V_{SS} + 2V_{TH})^2 + (V_{SS} + 2V_{TH})^4)}{4(V_{SS} + 2V_{TH})^2} \end{aligned} \quad (5)$$

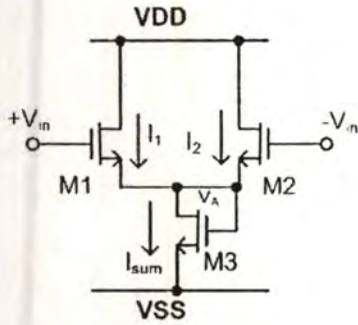


Fig. 1. Squarer Circuit

As small signal of V_{in} , assume that $V_{in}^4 \approx 0$. Then, the output current can be expressed as the simple input signal squarer as follows,

$$I_{sum} = \frac{K}{2} V_{in}^2 + \frac{K}{4} (V_{SS} + 2V_{TH})^2 \quad (6)$$

It can be derived from the small signal that

$$I_{sum} = g_m V_A \quad \text{or} \quad V_A = \frac{I_{sum}}{g_m}$$

$$V_A = \frac{K}{2g_m} V_{in}^2 + \frac{K}{4g_m} (V_{SS} + 2V_{TH})^2 \quad (7)$$

Equation (7) can be written as simple formula as,

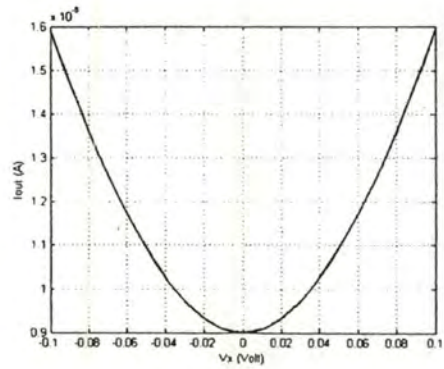
$$V_A = aV_{in}^2 + b \quad (8)$$

where $a = K/2g_m$ and $b = K(V_{SS} + 2V_{TH})^2/4g_m$.

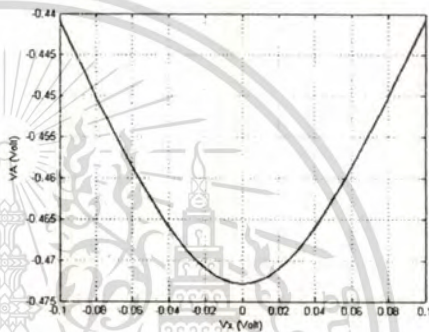
III. SIMULATION RESULTS

The performance of the proposed squarer circuit is simulated using PSPICE with level 7 model of $0.18\mu\text{m}$ MOS parameter from MOSIS [6]. The circuit is as simple as shown in Fig. 1, and the simulation uses $0.18\mu\text{m}$ CMOS with $L/W = 0.27/0.27$ (μm), the supply voltage $V_{DD} = +1\text{V}$ and $V_{SS} = -1\text{V}$. Since the drains of the squarer transistors (M1, M2) are connected to V_{DD} , while *Gate* and *Drain* of M3 are coupled, all transistors work in the saturation region.

Fig. 2 shows the DC transfer curves of the squarer circuit as in Fig. 1. The input range is from -100mV to $+100\text{mV}$. The output current shown in Fig 2(a) is graphically functioned as squaring function as mentioned in (6). The minimum value in the center, $I_{min} = 900.97\text{nA}$, is the constant value in (6). Meanwhile, Fig 2(b) shows the squaring output voltage of the circuit that conforms to (7). The minimum value in the center, $V_{Amin} = -472.89\text{mV}$, is the constant value in (7). The maximum values of output $I_{max} = 1.593\mu\text{A}$ and $V_{Amax} = -440.84\text{mV}$ are the output of inputs $\pm 100\text{mV}$.



(a) current output



(b) voltage output

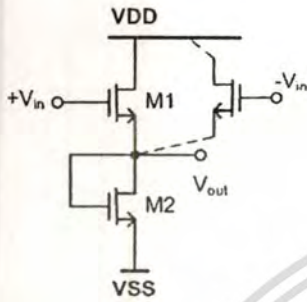
Fig 2. The DC transfer curves of the squarer circuit

Fig 3(a) shows the squarer circuit in Fig 1 that is considered as a source follower for the frequency response analysis. The frequency response of the source follower is determined by two capacitances designated as C_1 and C_2 in the small-signal model as shown in Fig 3(b). C_1 consists of capacitances connected between the input and output of the source follower, which are primarily C_{gs1} . C_2 consists of capacitances connected from the output of the source follower to ground. This includes C_{gd2} (or C_{gs2}), C_{bd2} , C_{bs1} , and C_1 of the next stage. The small-signal frequency response can be found as [7]

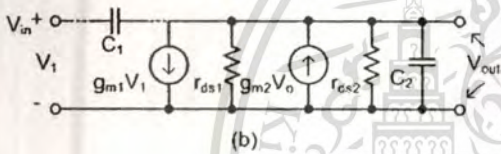
$$\frac{V_{out}}{V_{in}} = \frac{g_{m1} + sC_1}{g_{ds1} + g_{ds2} + g_{m1} + g_{m2} + GL + s(C_1 + C_2)} \quad (9)$$

$$\frac{V_{out}}{V_{in}} = \frac{c_0 + c_1s}{d_0 + d_1s} \quad (10)$$

The result of frequency characteristic slightly depends on the bias and ac of the input voltage. Fig. 4 shows the frequency response of the squarer circuit. For the frequency characteristic, $-V_{in}$ and $+V_{in}$ are the variable frequency with $V_{bias} = 0.2V$ and $V_{ac} = 0.1V$. At this input, the -3dB bandwidth of 10.96GHz is achieved. This frequency response has advantages to be used in the communication systems, and can accommodate the Ultra Wide Band applications.



(a)



(b)

Fig. 3 Squarer circuit as source follower

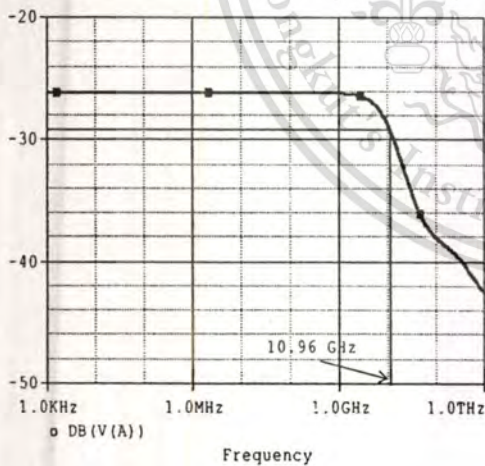


Fig. 4 The frequency response of squarer circuit as source follower

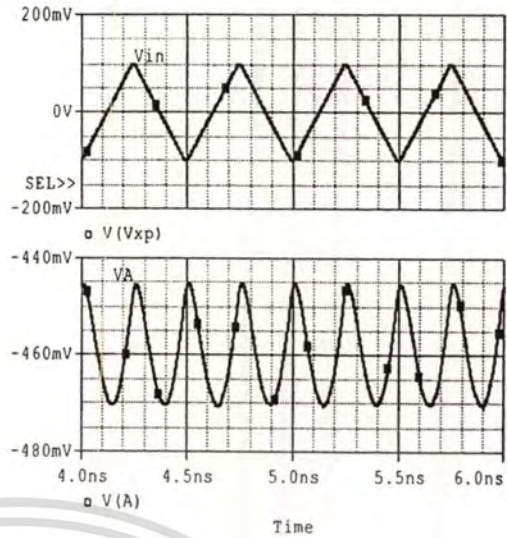


Fig. 5 Transient output with saw tooth input

Fig. 5 shows the transient output of the squarer circuit. The input voltage $+V_{in}$ has 0.5ns time period. The input swings from -100mV to +100mV.

Table I shows the performances of the multiplier. The multiplier has GHz-bandwidth response with low power consumption. The circuit has supply voltage $\pm 1V$ and the power dissipation 86.5 μ W. The input range $\pm 100mV$ will have the output range -472.89mV to -440.84mV of voltage or 900.97nA to 1.593uA of current.

TABLE I
PERFORMANCES OF THE SQUARER CIRCUIT

Number of MOS	3
Supply	$\pm 1V$
W/L	0.27 μ m/0.27 μ m
Input range	$\pm 100mV$
Output range	VA = -472.89mV to -440.84mV I = 900.97nA to 1.593uA
Freq. Response	10.96 GHz
Power dissipation	86.5 μ W

IV. CONCLUSION

A simple CMOS squarer circuit is proposed. The circuit is based on 0.18 μ m CMOS technology simulated using PSPICE level 7. The circuit has wide dynamic range, GHz-bandwidth response and low power consumption. The proposed circuit has been simulated with SPICE and achieved -3dB bandwidth of 10.96 GHz as source follower. The power consumption is about 86.5 μ W with a $\pm 1V$ power supply voltage. The Giga Hertz frequency response has advantages to be used in the communication systems, and can accommodate the UWB bandwidth.

REFERENCES

- [1] S. I. Liu and D. J. Wei, "Analogue squarer and multiplier based on MOS square-law characteristic," *Electron. Lett.*, vol. 32, no. 6, pp. 10.96-542, March 1996.
- [2] C.Y. Huang, C.Y. Chen and B.D. Liu, "Current-mode linguistic hedge circuit for adaptive fuzzy logic controllers," *Electro. Lett.*, vol.31, no. 17, pp. 1517-1518, August 1995.
- [3] I.M. Filanovsky and H.P.Baltes, "Simple CMOS analog square-rooting and squaring circuits," *IEEE Trans. Circuits and Systems-i*, vol. 39, no. 4, pp. 312-315, April 1992.
- [4] P. Gray, P. J. Hurst, S. H. Lewis and R. G. Meyer, *Analysis and design of analog integrated circuit*, John wiley & sons, 2001
- [5] <http://www.mosis.org/Technical/Testdata/tsmc-018-prm.html>
- [6] B. Razavi, "Design of Analog Integrated Circuits", New York: McGraw-Hill, 2001, pp. 126-129.
- [7] P. E. Allen, D. R. Holberg, "CMOS Analog Circuit Design", New York: Oxford Univ. Press, 2002, pp. 221-226.



December 24, 2008

Notification of Acceptance

Dear Authors

Manuscript No.KH256

Title: BER Analysis of IR-UWB Communication over Modified S-V Channel Model

Authors: Risanuri Hidayat, Kobchai Dejhan, Plichet Moungnoul and Yoshikazu Miyanaga

Received April 28, 2008 ; revised October 24, 2008

It is our great pleasure to inform you that the above paper submitted to the Journal of Signal Processing has been accepted for publication.

The paper will be published in the September issue (Vo. 13, No. 5) of the Journal of Signal Processing.

Sincerely yours,

Takashi Yahagi
Editor-in-Chief



Journal of Signal Processing

BER ANALYSIS OF IR-UWB COMMUNICATION OVER MODIFIED S-V CHANNEL MODEL

Risanuri Hidayat¹, Kobchai Dejhan¹, Phichet Moungnoul¹, Yoshikazu Miyanaga²

¹ Faculty of Engineering
King Mongkut's Institute of Technology Ladkrabang (KMITL), Bangkok 10520, Thailand
{risanuri, kobchai, phichet}@telecom.kmitl.ac.th

² Division of Media and Network Technologies, Graduate School of Information Science and Technology
Hokkaido University, Sapporo, Japan
miya@ist.hokudai.ac.jp

Abstract. This paper proposes BER of the Impulse Radio Ultra Wideband pulse communication over modified S-V channel model. The pulse is generated from circuit using HSPICE level 49. The channel model is generated from a modified S-V model. Binary Pulse Modulation is applied, and bit-error rate (BER) is measured over several of bit rates. The result shows that the shorter pulse over LOS and NLOS channel gives the better bit rates than the longer pulse. Moreover, UWB communication is appropriate with high bit rates in LOS channel.

Keywords: Impulse Radio, UWB, S-V Channel Model, LOS NLOS, monocycle pulse, triplet pulse.

1. Introduction

Since the Ultra Wide Band (UWB) technology was presented for telecommunication, many papers both in concepts and hardwares have been presented to develop the technology. FCC (Federation Communication Commission) has proposed 7.5 GHz (3.6-10.1 GHz) bandwidth and IERP (Isotropic Effective Radiation Power) regulation for UWB wireless communications [1].

Since FCC released UWB frequency band [1], several monocycle pulse shapes have been introduced [2]. Some researches have published pulse generators for UWB in circuit level [3]-[6]. The conventional circuit design requires many components and thus much power consumption. This paper proposes new circuit that has advantages of simple circuit and low power. It applies the delay process that occurs in MOS gates [7, 8]. The input transition is AND-ed for a few nanoseconds. A Gaussian pulse is thus generated. The generation is simulated based on 0.18 μm CMOS technology.

On the other hand, UWB performance for communication has been studied [9]-[18]. In previous work, binary modulations for impulse radio include pulse position modulation (PPM) [9, 10] and pulse amplitude modulation (PAM) [11]. Among them, bipolar PAM presents the highest power efficiency [12].

BER performance for impulse radio ultra wideband (IR-UWB) systems in multipath propagation channels has been introduced [13, 14]. However, the performances are considered only in few multipath models. Using such channel model, it is difficult to evaluate in actual environment.

In order to realize actual condition, a statistical model is established for the ultra-wide bandwidth in a simulation [15, 16]. Since a model using a Saleh-Valenzuela (S-V) introduced [17] as the channel measurements showed multipath arriving in clusters, the model has been modified for the UWB signal application [18]. In [15]-[18], since channel models have been developed, UWB systems have not been evaluated by only using them.

This paper analyzes BER of Ultra Wide Band pulse for communication over channel models by a simulation. The UWB pulse used in this paper is an Impulse Radio UWB generated from circuits using HSPICE level 49 models, while the channel model used in this paper is a modified Saleh-Valenzuela [17, 18, 19]. BER quantifies the reliability of the entire radio system from "bits in" to "bits out," including the electronics, antennas and signal path. Data sent by the transceiver are converted to UWB pulse using Binary Pulse Modulation (BPM) [11] and are then received by the receiver. At the receiver the pulse is then converted to data again. The comparison between the

data bits sent by transmitter and the data bits received by receiver represents the BER values.

The paper is organized as follows. Section I introduces the background of research. Section II describes UWB pulse principles which show the basic concepts of UWB and its generation circuit. The channel model and the simulation method are explained in section III and IV, respectively. The simulation results are presented in section V. The conclusion appears in section VI.

2. UWB Pulse

2.1. Gaussian Pulse

Some references have represented several formulas of Gaussian pulse [2, 4, 6]. A monocycle pulse is the first derivative of Gaussian pulse. The Gaussian pulse has formula (1), while the monocycle is given in (2).

$$x(t) = A_1 \cdot e^{-2\left(\frac{\pi t}{T_c}\right)^2} \quad (1)$$

$$x^{(1)}(t) = \frac{dx(t)}{dt} = A_2 t \cdot e^{-2\left(\frac{\pi t}{T_c}\right)^2} \quad (2)$$

$$f_c = \frac{1}{T_c} \quad (3)$$

where T_c is the width of the pulse. The values A_1 and A_2 are amplitudes. Figure 1 shows the waveform of Gaussian and monocycle pulse. The Federal Communications Commission (FCC) has recently approved the deployment of UWB on an unlicensed basis in the 3.1–10.6 GHz band subject to a modified version of Part 15.209 rules. The essence of this regulation is to limit the power spectral density (PSD) measured in a 1-MHz bandwidth at the output of an isotropic transmit antenna as shown in Fig. 2. [1]

2.2. Proposed UWB Pulse Generation

The Gaussian pulse generation used in this paper is proposed. The circuit is shown in Fig. 3. All circuits are simulated using HSPICE level 49 of 0.18 μm CMOS parameter given from Mosis [20]. The input is a step signal or pulse that the width is in such a way that the Gaussian pulse can be performed. Fig. 4 shows the time diagram of Gaussian monocycle pulse at the V_{out1} node that conforms to (2). Fig. 5 shows the normalized Power Spectral Density (PSD) of the derivative of the monocycle pulse from the circuit. When a pulse is transmitted, due to the derivative characteristics of the antenna, the output of the transmitter antenna can be modelled by the first derivative of the pulse [21]. The derivative can be achieved by the basics of differential calculus

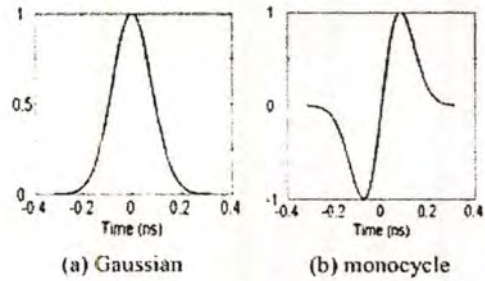


Fig. 1 Gaussian pulse waveform

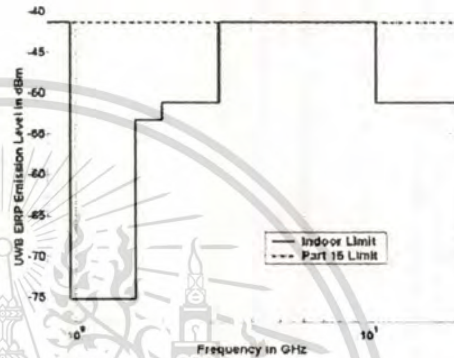


Fig. 2 UWB spectral mask and FCC Part 15 limits

$$x^{(1)}(t) = \lim_{dt \rightarrow 0} \frac{x(t+dt) - x(t)}{dt} \quad (4)$$

PSD of the deterministic power signal, $w(t)$, is

$$P(f) = \lim_{T \rightarrow \infty} \left(\frac{|X(f)|^2}{T} \right) \quad (5)$$

Where T is the pulse spacing interval. $X(f)$ is the Fourier transform of the pulse, i.e. $x(t)$. $P(f)$ has units of watts per hertz. When $X(f)$ is attained, the peak emission frequency, i.e. f_M , can be found as the frequency at the maximum value of $|X(f)|$. The normalized PSD is used to comply with the FCC spectral mask of the pulse that is transmitted by antenna [1, 21, 22]. The normalized PSD can be defined as follows

$$|P(f)| = \frac{|X(f)|^2}{|X(f_M)|^2} \quad (6)$$

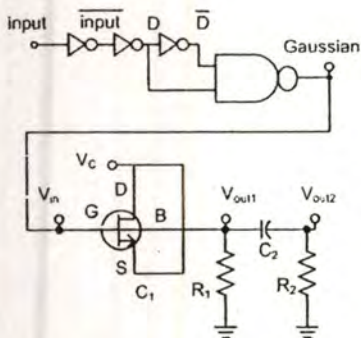


Fig. 3 Monocycle Circuit

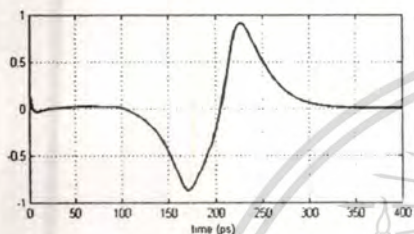


Fig. 4 The generated Gaussian monocycle pulse

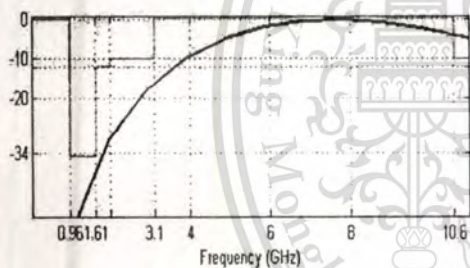


Fig. 5 Normalized PSD of the derivative monocycle pulse in Fig. 4

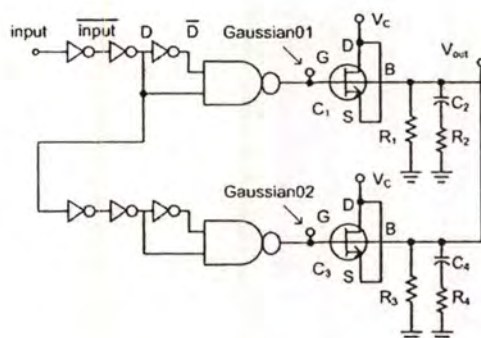


Fig. 6 The improvement of the proposed circuit

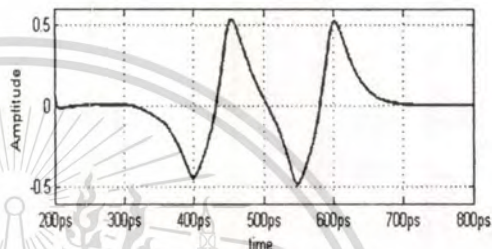


Fig. 7 The time diagram of Fig. 6

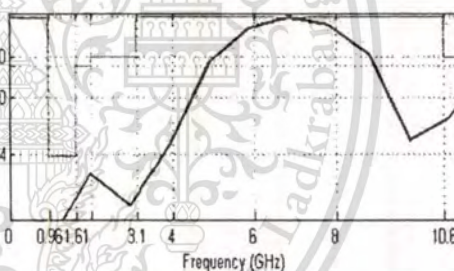


Fig. 8 The normalized PSD of the derivative pulse Fig.7

Fig. 6 shows the other Gaussian monocycle pulse generation. It is called triplet pulse. The second monocycle pulse is generated after being delayed by two NOT gates. Then, both monocycles are connected to generate UWB pulse the 3rd derivative of the Gaussian pulse. The time diagram of Gaussian02 node in Fig. 6 is equal to Gaussian01 node with some delays. Fig. 7 shows the time diagram of Gaussian monocycle pulse at the V_{out} node. The figure shows that the graphic has four peaks of signal which conducts as the triplet pulse or the 3rd derivative of Gaussian pulse. Fig. 8 shows the normalized Power Spectral Density (PSD) of the derivative of the UWB pulse from the circuit in Fig. 6. As shown in Fig. 8, the normalized PSD complies with the FCC spectral mask.

This monocycle circuit design as in Fig. 3 has advantage of simplicity and low cost power that are main focus in the UWB point of view. It applies 3 (three) NOT's, 1 (one) NAND, 2 (two) resistors, 1 (one) capacitor, and 1 (one) MOS as capacitor. In total, it is implemented with 11 MOS. The supply is ± 1 volt, and 5.35 mW for maximum power consumption.

As comparison, Azakkour [6] has proposed a gated pulse generator for UWB using VCO and on-off switch, which was more complicated. The power is also larger, i.e. 243 mW. Kim [5] has also proposed a UWB pulse generator using digital CMOS circuit, whose average power consumption of the whole circuit was 15.4 mW and 675 mW at the pulse repetition frequency of 500 and 1 MHz, respectively. A wavelets generation circuit for UWB proposed by Gerrits [3] combined the output

signals of four bipolar differential pairs to generate the second derivative of the Gaussian function as output signal. The circuit is implemented with 8 (eight) MOS's and it requires 4 (four) current sources with the circuit.

Our proposed circuit successfully generates a Gaussian monocycle pulse with simple circuit, i.e, few components. The whole circuit is comprised of only 11 MOS's and 2 CR components.

The pulse in Fig. 6 has four peaks of waves and has double duration of time than the pulse in Fig. 3. This paper compares between the two pulses, which one has higher rates and more robust due to the noise and multipath channels. This comparison may be used as consideration in order to apply IR-UWB communication using either long pulse or short pulse.

The pulses have normalized PSD in 3.1-10.6 GHz frequency band that can fulfil the FCC rules of UWB communication, as described in Fig. 2. The generated pulse from Fig. 3 and Fig. 6 are exported from HSPICE into text files. The files of monocycle and triplet are then used as UWB pulse in the simulation.

3. Channel Model

There are several channel models used for analyzing wireless communication system that is designed for specific situation such as indoor and outdoor environment. For the time-of-arrival statistics, the model of Saleh-Valenzuela (S-V), which is used as the channel measurements, shows multipath arriving in clusters [17]. Since UWB waveforms can be up to 7.5 GHz wide, for example, any paths separated by more than about 133 psec. (equivalent to 4 cm path length difference) can be individually resolved at the receiver [19]. The realistic channel for IEEE 802.15 study group 3a has been developed by Saleh-Valenzuela (S-V model) and proposed for the real indoor channel model, where the clusters and rays are multi-path components [18]. This multi-path channel can be expressed as

$$h(t) = \sum_{l=0}^L \sum_{k=0}^K \alpha_{k,l} \delta(t - T_l - \tau_{k,l}) \quad (7)$$

where $\alpha_{k,l}$ is the multipath gain coefficient, T_l is the delay of the l^{th} cluster, and $\tau_{k,l}$ is the delay of the k^{th} multipath component relative to the l^{th} cluster arrival time (T_l).

As suggested in [18], $\alpha_{k,l} = \rho_{k,l} \beta_{k,l}$ is adopted, where $\rho_{k,l}$ is equally likely to take on the values of ± 1 , and $\beta_{k,l}$ is the lognormal fading term, due to the simplicity of the real channel coefficients, and to avoid the ambiguity of phase for an UWB waveform.

The proposed channel model uses the definitions as previously described in the S-V model, and is repeated here for completeness. T_l is the arrival time of the first

path of the l -th cluster; $\tau_{k,l}$ is the delay of the k -th path within the l -th cluster relative to the first path arrival time, T_l ; Λ is cluster arrival rate; and λ = ray arrival rate, i.e., the arrival rate of path within each cluster.

Therefore, $\tau_{0l} = T_l$. The distribution of cluster arrival time and the ray arrival time are given by

$$\begin{aligned} p(T_l | T_{l-1}) &= \Lambda \exp[-\Lambda(T_l - T_{l-1})], \quad l > 0 \\ p(\tau_{k,l} | \tau_{(k-1),l}) &= \lambda \exp[-\lambda(\tau_{k,l} - \tau_{(k-1),l})], \quad k > 0 \end{aligned} \quad (8)$$

The channel coefficients are defined as $\alpha_{k,l} = \rho_{k,l} \beta_{k,l}$, $\beta_{k,l}$ is obtained by this expression

$$20 \log_{10}(\beta_{k,l}) \propto \text{Normal}(\mu_{k,l}, \sigma^2) \quad (9)$$

$$\text{or } |\beta_{k,l}| = 10^{n/20}$$

where

$$n \propto \text{Normal}(\mu_l, \sigma^2) \quad (10)$$

$$E[\beta_{k,l}^2] = \Omega_0 e^{-T_l/\Gamma} e^{-\tau_{k,l}/\gamma}$$

T_l is the excess delay of bin l and Ω_0 is the mean power of the first path of the first cluster, and $\rho_{k,l}$ is ± 1 . Then μ_l is given by

$$\mu_l = \frac{10 \ln(\Omega_0) - 10T_l/\Gamma - 10\tau_{k,l}/\gamma}{\ln(10)} - \frac{\sigma^2 \ln(10)}{20} \quad (11)$$

4. Simulation Method

Fig. 9 shows the block diagram of the transmitter and receiver communication. Transmitter converts the data bits to UWB pulses and the pulse are transmitted through the antenna. There is a channel model between the transmitter and the receiver. At receiver, the pulses are received by antenna and LNA (Low Noise Amplifier) becomes $u_f(t)$. Finally, the pulses are detected using the template pulse.

The classic binary pulse modulation (BPM) is implemented. It can be presented using two antipodal Gaussian pulses. The transmitted binary baseband pulse that is modulated information signal (t) is expressed as [11]

$$x(t) = d_j \cdot w_{ir}(t) \quad (12)$$

where $w_{ir}(t)$ represents the UWB pulse waveform, j represents the bit transmitted that $j=1$ then $d_j = 1$ and $j='0'$ then $d_j = -1$.

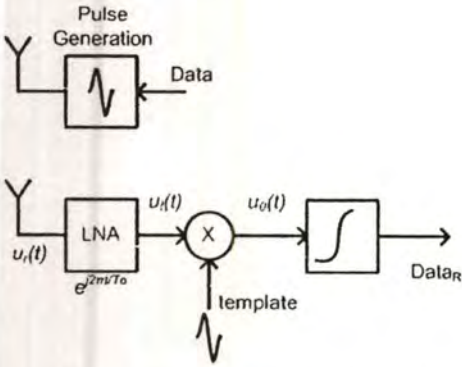
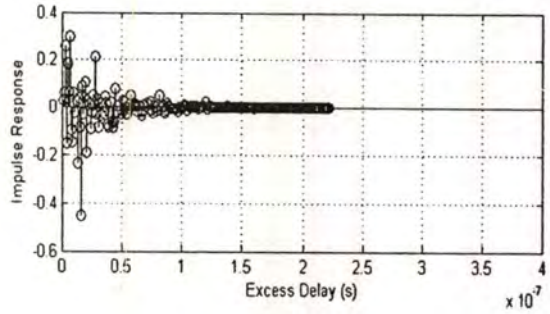


Fig. 9 Tx-Rx Communication Block Diagram



(b) NLOS

Fig. 10 The generated channel model

A channel is available between transceiver and receiver. An UWB channel model is derived from the modified Saleh-Valenzuela model suitable for home environment with both LOS and NLOS as described previously. There are 5 key parameters that define the model: Λ = cluster arrival rate; λ = ray arrival rate, i.e., the arrival rate of path within each cluster; Γ = cluster decay factor; γ = ray decay factor; and σ = standard deviation of lognormal fading term (dB). All parameters are taken into account for channel modeling as formulated in (8)-(11).

Table 1 Channel model parameters.

Model Parameters	LOS	NLOS
Λ (1/nsec)	1/60	1/11
λ (1/nsec)	1/0.5	1/0.35
Γ (nsec)	16	16
γ (nsec)	1.6	8.5
σ (dB)	4.8	4.8

This paper uses one channel model generated from S-V model using the parameters as shown in Table 1. The equation in (7)-(11) and Table 1 derived from and based on Intel measurements [18] are used to generate a channel model. The generated channel model is shown in Fig 10.

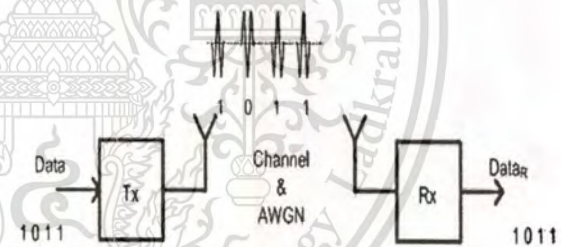
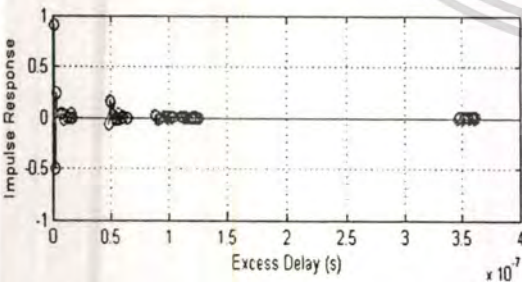


Fig. 11 UWB pulse communication.



(a) LOS

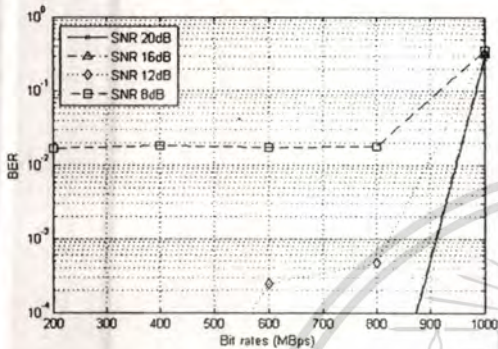
5. Simulation Results

The implementation is based on the block diagram as shown in Fig. 9. Fig. 11 shows the UWB pulse communication. The transceiver converts bits into UWB pulses, then the UWB pulses are reconverted the pulse back into bits by receiver. The comparison between the bits sent by transceiver and received by receiver gives BER value.

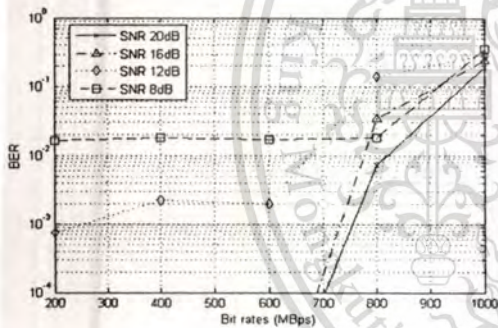
The channel is considered to analyze the bit rates of each pulse over the channel. Both monocycle and triplet pulses are employed. The channel models, both LOS and

NLOS using parameter in Table 1 are implemented as shown in Fig. 10. The modulation uses BPM.

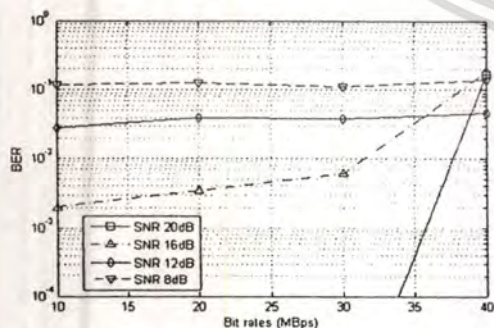
It is rare that communication systems use frequency band between 3.1-10.6 GHz. GSM/UMTS uses 0.9-1.8GHz, while WLAN uses 2.5 GHz. Only 802.11a system uses frequency band 5 GHz inside this UWB frequency standard. Therefore, some AWGN are included in the simulation. The result shows that AWGN with SNR value above 20 dB, BER values are significantly low and the graphs are close to BER without AWGN.



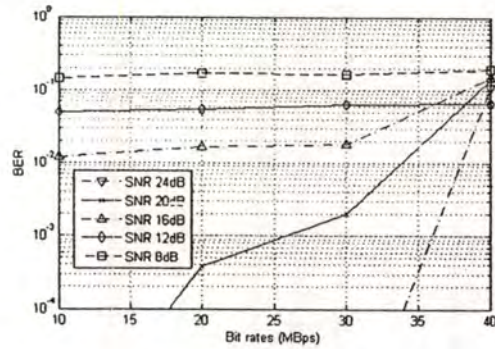
(a) UWB monocycle pulse over LOS channel



(b) UWB triplet pulse over LOS channel



(c) UWB monocycle pulse over NLOS channel



(d) UWB triplet pulse over NLOS channel

Fig. 12 BER of the UWB pulses through the LOS and NLOS channel models

In our experiments, there are around 10^4 bits sent from the transceiver to receiver, and later being analyzed. The bits are sent periodically, so that give a bit rate value in Mbps. The various bit rates and its BER can be seen in Fig. 12. The result shows that interference of multipath gives high effect to make an error. The LOS channel model in Fig. 10 (a) has the last significant paths that cross a 10 dB threshold (NP_{10dB}) at 0.5×10^{-7} sec and it has only 5 multipaths. It gives low BER until hundreds Mbps. Meanwhile, the NLOS channel has many multipaths that influence the pulses, so that it can not be sent in high bit rates. The NLOS channel model in Fig. 10 (b) has the last significant paths that cross a 10 dB threshold (NP_{10dB}) at around 1.0×10^{-7} sec and it has around 33 multipaths, so that it is much thicker. The bit rates drops drastically in the NLOS channel model.

Fig. 12 shows the result of the BER of the monocycle and triplet pulses through the LOS and NLOS channel models. Fig. 12 shows that the influence of inter multipaths occurs in higher bit rates. In the LOS channel, it gives high error after 800 Mbps. For bit rate below than 800 Mbps, BER is relatively low (in 10^{-4} or lower) in high SNR of AWGN. In the NLOS channel, high error occurs after 30 Mbps. For bit rate below than 30 Mbps, BER is relatively low (in 10^{-4} or lower) in high SNR. Note that in order to draw the line in Fig. 12, the value of $\log(10^{-6})$ is given instead of BER = 0, since log zero is infinity.

Fig. 12 (a) shows data sent using monocycle pulse over the LOS channel model. The result shows that SNR 8 dB AWGN gives high BER. SNR 12 dB gives no error (or error lower than 10^{-4}) until 400 Mbps and has error in 10^{-4} level until 800 Mbps. BER also increases drastically after 800 Mbps. SNR 16 and 20 dB has no error (or error lower than 10^{-4}) until 800 Mbps, but it has much higher BER afterwards.

Fig. 12 (b) shows data sent using triplet pulse over the LOS channel model. SNR 8 dB AWGN gives high BER. SNR 12 dB gives small error (in 10^{-4} level) within 200 Mbps and error in 10^{-3} level until 600 Mbps. BER

also increases drastically after 600 Mbps. SNR 16 and 20 dB has no error (below 10^{-4}) until 600 Mbps, and the value of BER increases drastically afterwards.

Different from the LOS channel that has much higher bit rates, the NLOS channel gives lower bit rates for the communication. In Fig. 12 (c), data are sent using monocycle pulse over NLOS channel model. It has high BER until SNR 12 dB. SNR 16 dB gives BER in 10^{-3} level occurs for bit rates below 30 Mbps and increases drastically after 30 Mbps. SNR 20 dB has no error (or error lower than 10^{-4}) until 30 Mbps, but it also has higher BER afterwards.

In Fig. 12 (d), data are sent using triplet pulse over the NLOS channel model. It has high BER until SNR equals to 12 dB. SNR 16 dB gives BER in 10^{-2} level for 30 Mbps and below and increases drastically afterwards. SNR 20 dB has no error (lower than 10^{-4}) for 10 Mbps, 10^{-4} level BER for 20 Mbps, and 10^{-3} level for 30 Mbps. It has higher BER for above 30 Mbps. Finally, SNR 24 dB has no error (lower than 10^{-4}) until 30 Mbps and has higher BER afterwards.

All results in Fig. 12 show that if the SNR of AWGN increases, then BER decreases. In this simulation, SNR 20 – 24 dB AWGN has good performances of BER value.

Comparing monocycle and triplet pulse, the result shows that for the same channel, the monocycle has more robust of AWGN. Fig. 12 (a) and (b) shows that the monocycle has error in 10^{-4} level until 800 Mbps, while the triplet begins to have more error since 600 Mbps. In Fig. 12 (c) monocycle has no error until 30 Mbps at SNR 20 dB, while SNR 24 dB has no error until 30 Mbps for triplet in Fig. 12 (d).

From the results, it can be said that UWB pulse communication is appropriate in the LOS channel, i.e., has high bit rates (hundreds Mbps). Nevertheless, this communication can be used until several Mbps in NLOS channel model

Table 2 Estimate of highest bit rates (HBR)

Model	Bit rates (Mbps)		
	SNR 20 dB	SNR 16 dB	SNR 12 dB
LOS monocycle	800	800	800
LOS triplet	600	600	200
NLOS monocycle	30	-	-
NLOS triplet	20	-	-

Table 2 shows estimation of highest bit rates without error (or error in 10^{-4} level is tolerable). If the less BER is desired, then lower bit rate can be implemented. However, in high SNR environment, the high bit rate can still be implemented. It shows that monocycle pulse over LOS channel gives the best bit rates. By looking at the UWB reference standard and compare to the others as shown in Table 3 [23], it seems that this communication model is preferable for the LOS channel.

Table 3 Comparison of UWB bit rate with other standards.

Speed (Mbps)	Standard
480	UWB, USB 2.0
200	UWB (4 m minimum)
110	UWB (10 m minimum)
90	Fast Ethernet
54	802.11a
20	802.11g
11	802.11b
10	Ethernet
1	Bluetooth

Based on Fig. 12(a)-(d), some samples of bit rate are chosen to take a closer look at each pulse over LOS and NLOS channels. For the LOS channel based on Table 3, 400 Mbps is chosen for the monocycle and triplet pulse. However, since the maximum bit rates for NLOS channel is only 30 Mbps, this rate is chosen.

There are 10^4 bits sent from the transceiver to receiver. Fig. 13 shows the BER performance of the UWB pulses through the LOS and NLOS channel models in the chosen bit rates. Fig 13 shows that the monocycle pulse is more robust than triplet both in LOS and NLOS channels.

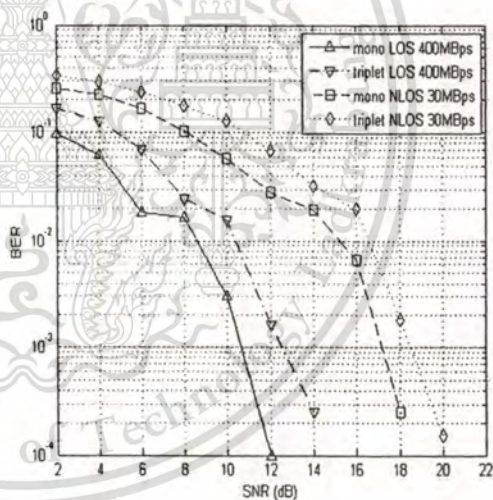


Fig. 13 BER performances over AWGN channels

For the monocycle pulse over the LOS channel, 400 Mbps is chosen. That means the pulse is sent in 2.5ns periodic time. It has BER in 10^{-3} level for SNR 10 dB, and BER in 10^{-4} level for SNR 12 dB, respectively. By estimation of the graph in Fig. 13, data communication that needs BER 10^{-5} or less can be applied in SNR 13 dB or more.

For the triplet pulse over the LOS channel, 400 Mbps is also chosen. BER occurs in 10^{-3} level for SNR 12 dB,

and in 10^{-4} level for SNR 14 dB, respectively. It can be estimated that BER 10^{-5} or less can be applied in SNR 15 dB or more.

For the monocycle pulse over the NLOS channel, 30 Mbps is implemented (0.33 ns pulse periodic time). It has BER in 10^{-4} level for SNR 18 dB. From the graph in Fig. 13, it can be estimated that data communication with BER less than 10^{-4} level needs SNR 19 dB or more.

For the triplet pulse over the NLOS channel, 30 Mbps is chosen, since it is also the maximum rate. It has BER in 10^{-4} level at SNR 20 dB. Data communication that needs BER 10^{-5} or less can be applied in SNR 21-22 dB or more.

6. Conclusion

The BER analysis of the Impulse Radio Ultra Wide Band pulse communication over modified S-V channel model is presented. The pulse is generated from circuit using HSPICE CMOS model level 49. The channel model uses a modified S-V model. Binary Pulse Modulation is applied for modulation, and BER is measured over several bit rates. The result shows that monocycle pulse over LOS and NLOS channel gives the best bit. Moreover, UWB communication is appropriate with high bit rates in LOS channel.

Acknowledgment

The authors would like to thank the anonymous reviewers for their constructive comments and insights that helped improve this paper.

The authors also would like to thank the AUN/SEED-net project supported mainly by the Japan International Cooperation Agency (JICA) for supporting this research.

References

- [1] FCC 04-48 "First Report and Order in the Matter of Revision of Part 15 of the Commission's Rules Regarding Ultra-wideband Transmission Systems." Feb.14, 2002.
- [2] X. Chen, and S. Kiaei, "Monocycle shapes for ultra wideband system", Proc. IEEE International Symposium on Circuits and Systems, vol. 1, pp. 597-600, May 2002.
- [3] J. F. M. Gerrits, and J. R. Farserotu, "Wavelet generation circuit for UWB impulse radio applications", IEE Electronics Letters, vol. 38, issue 25, pp. 1737-1738, Dec. 2002.
- [4] H. Kim, D. Park, and Y. Joo, "Design of CMOS Scholtz's monocycle pulse generator", Proc. IEEE Conference on Ultra Wideband Systems and Technologies, pp. 81-85, Nov. 2003.
- [5] H. Kim, D. Park, and Y. Joo, "All-digital low-power CMOS pulse generator for UWB system", IEE Electronics Letters, Vol. 40, Issue 24, pp. 1534-1535, Nov. 2004.
- [6] A. Azakkour, M. Regis, F. Pourchet, and G. Alquie, "A new integrated monocycle generator and transmitter for ultra-wideband (UWB) communications", Proc. IEEE Symposium on Radio Frequency integrated Circuits, pp. 79-82, June 2005.
- [7] R. Hidayat, K. Dejhan, P. Moungnoul, Y. Miyanaga, "A 0.18 μm CMOS Gaussian Monocycle Pulse Circuit Design for UWB", Proc. IEEE Asia Pacific Conference on Circuits and Systems, pp. 89-92, Dec. 2006.
- [8] D. A. Hodges, H. G. Jackson, and R. A. Saleh, ed., *Analysis and Design of Digital Integrated Circuits*, McGraw-Hill, New York, 2003.
- [9] R. A. Scholtz, "Multiple access with time-hopping impulse modulation," Proc. MILCOM '93, vol. 2, pp. 447-450, 1993.
- [10] M. Z. Win, R.A. Scholtz, "Ultra-wide bandwidth time-hopping spread-spectrum impulse radio for wireless multiple-access communications," IEEE Trans. Comm., vol. 48, no. 4, pp. 679-691, April 2000.
- [11] I. Oppermann, M. Hamalainen, and J. Linatti, *UWB Theory and Applications*, John Wiley & Sons, West Sussex, 2004.
- [12] M. L. Welborn, "System considerations for ultra wideband wireless networks," Proc. IEEE RAWCON 2001, Boston, MA, Aug. 2001.
- [13] L. Ge, G. Yue, and S. Affes, "On the BER Performance of Pulse-Position Modulation UWB Radio in Multipath Channels", Proc. IEEE Conference on Ultra Wideband Systems and Technologies, pp. 231-234, May 2002.
- [14] G. Yue, L. Ge, and S. Li, "Performance of UWB time-hopping spread-spectrum impulse radio in multipath environments", Proc. IEEE Semiannual Vehicular Technology Conference (VTC '03), vol. 3, pp. 1644-1648, April 2003.
- [15] J. Karedal, S. Wyne, P. Almers, F. Tufvesson and A.F. Molisch, "Statistical Analysis of the UWB Channel in an Industrial Environment", Proc. IEEE Vehicular Technology Conference (VTC 2004), pp. 81-85, Sept. 2004.
- [16] D. Cassioli, M. Win and A. Molisch, "The Ultra-Wide Bandwidth Indoor Channel: From Statistical Model to Simulations", IEEE Journal on Selected Areas in Communications, Vol. 20, No. 6, pp. 1247-1257, 2002.
- [17] A. M. Saleh, R. A. Valenzuela, "A statistical model for indoor multipath propagation," IEEE Journal on Selected Areas in Communications, SAC-5 no. 2 (1987) 128- 137.
- [18] J. R. Foerster, Q. Li, "UWB Channel Modeling Contribution from Intel," IEEE P802.15 Working Group for Wireless Personal Area Networks (WPANs), June 2002, http://www.ieee802.org/15/pub/2002/Jul02/02279r0P802-15_SG3a-Channel-Model-Cont-Intel.doc
- [19] A.F. Molisch, J.R. Foerster, M. Pendergrass, "Channel models for Ultra wideband personal area networks", IEEE Wireless Communications, vol. 10, Issue 6 (2003), 14-21.
- [20] Wafer Electrical Test Data and SPICE Model Parameters (2007), <http://www.mosis.org/Technical/Testdata/tsmc-018-prm.html>
- [21] G. Breed, "A Summary of FCC Rules for Ultra Wideband Communications,"2005, <http://www.highfrequencyelectronics.com/Archives/Jan05/>
- [22] S. Hongsan, P. Orlik, A.M. Haimovich, L. J. Jr. Cimini, and Z. Jinyun, "On the Spectral and Power Requirements for Ultra-Wideband Transmission", Proc. IEEE on Communications, vol. 1, May 2003, pp. 738 - 742.

- [23] M. Ghavami, L. B. Michael, R. Kohno, *Ultra Wideband Signals and Systems in Communication Engineering*, John Wiley & Sons, West Sussex, 2004.



Risanuri Hidayat received the B.S. in Electrical Engineering from Gadjah Mada University Indonesia in 1992. He received M.Sc. degrees in Information Communication Technology from Agder University College Norway in 2002. He is currently studying D.Eng. degree in Electrical Engineering Department, Faculty of Engineering and Research Center for Communication and Information Technology (ReCCIT) at King Mongkut's Institute of Technology Ladkrabang (KMITL) Thailand. His research interest is in digital and analog circuit design, and circuit design and system for telecommunication

degrees from Hokkaido University, Sapporo, Japan, in 1979, 1981, and 1986, respectively. He was a Research Associate at the Institute of Applied Electricity, Hokkaido University from 1983 to 1987, a lecturer of Electronic Engineering at Faculty of Engineering, Hokkaido University from 1987 to 1988 and an Associate Professor of Electronic Engineering at Faculty of Engineering, Hokkaido University from 1988 to 1997. He is currently a Professor of Laboratory for Information Communication Networks, Division of Media and Network Technologies at Graduate School of Information Science and Technology, Hokkaido University. His research interests are in the areas of adaptive signal processing, nonlinear signal processing and parallel/pipelined VLSI system. Dr. Miyanaga is a senior member of the IEEE, U.S.A., the Institute of Electronics, Information and Communication Engineers (Japan) and the Acoustical Society of Japan



Kobchai Dejhan received the B.Eng. and M.Eng. in electrical engineering from the King Mongkut's Institute of Technology Ladkrabang (KMITL), Bangkok, Thailand, in 1980 and 1982, respectively and the Doctorate degree in telecommunications from Ecole Nationale Supérieure des Telecommunications (ENST/Telecom Paris) Paris, France in

1989. Since 1980, he has been a member of the Department of Telecommunication at Faculty of Engineering, KMITL, where he is currently an associate professor of telecommunication. His research interests are analog circuit design, digital circuit design, communication system and communication circuit design. He is member of IEICE, ACM and senior member of IEEE.



Phichet Moungnoul received the B.Ind.Tech. in telecommunication technology, M.Eng. and D.Eng. degree in Electrical Engineering from King Mongkut's Institute of Technology Ladkrabang (KMITL), Bangkok, Thailand, in 1992, 1997 and 2001, respectively. Since 1998, he has been a member of the Department of Telecommunication at Faculty of

Engineering, KMITL, where he is currently an assistant professor of telecommunication. His research interests are wireless and mobile communication and broadband communication.



Yoshikazu Miyanaga was born in Sapporo, Japan, on December 20, 1956. He received the B.S., M.S., and Dr. Eng.

BIOGRAPHY



Risanuri Hidayat was born in August 2, 1967 at Sleman, Yogyakarta, Indonesia. He received the B.S. in Electrical Engineering from Gadjah Mada University Indonesia in 1992. Since then, he has been a staff of lecturer in the Electrical Engineering Department, Faculty of Engineering, Gadjah Mada University, Indonesia. He received M.Sc. degrees in Information Communication Technology from Agder University College Norway in 2002. He was Doctorate student in Electrical Engineering Department, Faculty of Engineering and Research Center for Communication and Information Technology (ReCCIT) at King Mongkut's Institute of Technology Ladkrabang (KMITL) Thailand from June 2005 to January 2009, under AUNSEED-Net program. His research interest is in digital and analog circuit design, and circuit design and system for telecommunication.

